The University Of Sheffield.

In situ studies of spin-coated polymer films

Daniel Thomas William Toolan

Presented for the degree of Doctor of Philosophy
Department of Chemical and Biological Engineering
The University of Sheffield
May 2014

Acknowledgments

I would like to acknowledge my supervisor Dr Jonathan Howse for allowing me the freedom to pursue all manner of ideas and the opportunity to conduct exciting research! My special thanks go to Dr Paul Topham, Miss Nikki Pullan and Mr Michael Harvey for supplying copious amounts of polystyrene for me to study. I am also grateful to Mr Richard Hodgkinson for help and discussions on electronics matters. Many thanks to Syuji Fujii and the Japan Society for the Promotion of Science for allowing me to conduct research in Japan. Finally I'd like to thank Sarah-Jane Bell for putting up with me.

Abstract

Spin-coating is a facile, straightforward, solution processing technique for the production of uniform thin films, which has been utilised for a wide range of applications including organic electronic and photonic devices, sensors, membranes and optical coatings. Many of the applications of spin-coated polymer films utilise the propensity of polymers to self-assemble, resulting in the formation of well-ordered, intricate morphologies that evolve towards thermodynamic equilibrium. Understanding the interplay between processes such as phase-separation and crystallisation, which control the final morphology, has therefore been the topic of intense theoretical and experimental studies in the field of polymer science. In particular the potential of spun-cast organic electronic devices to help alleviate the world's dependence upon fossil fuels in terms of energy generation and energy efficiencies has driven the need for greater control over the final morphology, in order to produce more efficient devices.

I have developed the technique of stroboscopic microscopy, which facilitates direct imaging during spin-coating, allowing us to directly observe, in real-time, the processes of self-assembly at the microscale. I have advanced the technique to operate in three different modes, which allow observations of topography, composition and crystallisation.

This thesis presents the direct observations of self-assembly processes that occur during the spin-coating of model polymer systems [polystyrene:poly(methyl methacrylate) and polystyrene:poly(ethylene glycol)], systems relevant to organic electronics [polystyrene:poly 9,9'-dioctlyflourene] and polystyrene colloidal dispersions. A number of key parameters have been investigated including the effects of; rotation rate, composition, polydispersity and

the interplay between crystallisation and phase separation. The observation that of have been made may be utilised to either, rationally design processing conditions that will allow targeted morphologies to be attained or information obtained in real-time may be used to direct and control self-assembly processes in order to achieve desired morphologies.

The work presented in this Thesis concentrates on the development of the technique of stroboscopic microscopy for the study of the self-assembly processes which occur when polymer blends are spin-coated. Specifically, I looked to understand the role of the quench rate, composition, polydispersity and crystallinity on self-assembly processes. Chapter 1 gives an introduction to the theory of self-assembly processes and gives an overview of the progress made in conducting *in situ* studies of spin-coated polymer blends.

In Chapter 2 I will explain the technique of stroboscopic microscopy and how I have developed the technique to provide information regarding topographical, compositional and crystalline development.

In Chapter 3 I will present results of the direct observation, in real-space, of the phase separation of high molecular weight polystyrene and poly(methyl methacrylate) spun-cast from *ortho*-xylene utilising stroboscopic microscopy in an interferometric mode. By varying the rotational rate of the spin-coating process, I am able to alter how the polymer blend is quenched and the subsequent effect on morphological development. Importantly, I am able to show that the mechanism by which the final phase separated structure is formed is through domain coarsening when rich in solvent, before vitrification occurs and fixing the phase separated structure.

In Chapter 4 I will present the direct observation of compositional and corresponding structural development for blends of polystyrene and poly(9,9'-dioctylfluorene), at a range of compositions, producing a range of different phase separated morphologies. I initially observe domains formed by spinodal decomposition, coarsening *via* Ostwald Ripening until an interfacial instability causes break-up of the bicontinuous morphology. Ostwald ripening continues, and depending upon composition a bicontinuous morphology is re-established.

Further, by observing compositional and morphological development in real-time, I have developed a method to direct and control morphological structure development through control of the spin coating parameters *via in situ* feedback.

In Chapter 5 I will present results showing the role of polydispersity play on the phase separation processes that occur during the spin-coating of blends of polystyrene and poly(9,9'-dioctylflourene) using stroboscopic fluorescence microscopy. The data indicates that increasing polydispersity shifts the critical point, altering morphological development.

In Chapter 6 I present results showing the direct observation of crystallisation, phase separation and Marangoni instabilities for blends of polystyrene and poly(ethylene oxide). This data illustrates the interplay between different processes, the complexities of which, result in the formation of highly intricate morphologies.

Chapter 7 presents the direct observation of the ordering of polystyrene colloids during spin-coating, which allows identification of the roles volume fraction, shear force and capillary force play in the formation of colloidal crystals.

Contents

1. Introduction

1.0 Introduction 2
1.1 Thermodynamics of polymer blends 3
1.2 Phase transitions 13
1.2.1 Nucleation and growth 13
1.2.2 Spinodal decomposition 14
1.2.3 Coarsening and coalescence 16
1.2.4 Polydispersity effects 17
1.2.5 Crystallisation 18
1.2.6 Marangoni effects 21
1.2.7 Colloidal ordering 23
1.3 Spin-coating 26
1.4 Development of *in situ* studies of spin-coated polymer films 29
1.4.1 Specular reflectivity 31
1.4.2 Specular reflectivity combined with off-specular scattering 37
1.4.3 Video observation studies 50
1.5 Summary 60
1.6 References 61

2. Stroboscopic Microscopy

2.0 Introduction 67
2.1 Topographical mode of operation 70
2.2 Compositional mode of operation 75
2.3 Crystallisation mode of operation 78
2.4 References 81

3. Effect of Spin-speed

3.0 Introduction 83
3.1 Experimental 84
3.2 Results and discussion 85
3.3 Conclusions 96
3.4 References 97

4. Compositional Studies

4.0 Introduction 99
4.1 Experimental 100
4.2 Results and discussion 101
4.3 Conclusions 113
4.4 References 114

5. Effect of Polydispersity

5.0 Introduction 116
5.1 Experimental 117
5.2 Results and discussion 118
5.3 Conclusions 122
5.4 References 123

6. Crystallisation
6.0 Introduction 125
6.1 Experimental 127
6.2 Results and discussion 127
6.2.1 Crystallisation of PEG 127
6.2.2 Interplay between phase separation and crystallisation 130
6.3 Conclusions 141
6.4 References 141
7. Colloidal Crystallisation
7.0 Introduction 144
7.1 Experimental 146
7.2 Results and discussion 146
7.3 Conclusions 161
7.4 References 162
8. Conclusions and future work
8.0 Conclusions and future work 165
Appendix I (Papers published during PhD) 169

Chapter 1. Introduction

Parts of this chapter were published in:

Toolan, D. T. W. & Howse, J. R., "Development of in situ studies of spin coated polymer films". *Journal of Materials Chemistry C* **1**, 603-616 (2013), DOI: 10.1039/C2TC00026A.

1.0 Introduction

Since the discovery that the semiconducting polymer, poly(p-phenylene vinylene) (PPV) exhibited electroluminescence by Burroughes, Friend and Bradley in 1990,(1) a tremendous amount of research effort has been invested in the field of polymer electronics, which has lead to dramatic increases in device efficiencies within a relatively short timeframe. This research effort has been driven by the potential of organic light emitting diodes (OLED), organic field effect transistors (OFET) and organic photovoltaics (OPV), which may help to mitigate the worlds energy dependence upon fossil fuels, through increased energy efficiencies (OLED & OFET) and providing a clean, renewable energy source (OPV).

One advantage of organic based electronic devices over inorganic based electronics is that the semiconducting polymers may easily be processed from solution, which opens the potential of reel-to-reel continuous processing methods for high throughput, low-cost, device fabrication. Spin-coating is a solution processing technique for producing highly uniform thin-films and is commonly employed for the fabrication of photoresists, optical coatings, synthetic opals and organic electronic devices. The process involves depositing a solution onto a substrate that is then rotated at high speed (typically 1000 – 10,000 rpm), resulting in the formation of a highly uniform thin film within a matter of seconds, as solution is ejected from the edge of the substrate, due to shear forces and solvent is removed by evaporation.

Organic electronic devices such as OPVs are fabricated by spin-coating a blend of two different polymers from a common solvent, and posses a rich variety of accessible non-equilibrium morphologies, which form through self-assembly

processes, such as phase-separation, stratification and crystallisation. The performance, and hence future economic success of organic electronic devices is highly dependent upon the generation of a well-defined, interconnected, crystalline morphology. Despite the effort undertaken so far, as yet, we still do not fully understand, and nor are we able to fully control, the processes of self-assembly that occur during spin-coating. The aim of this thesis is to develop new *in situ* experimental techniques to further our understanding of the self-assembly processes occurring during the spin-coating of polymer blends. It is believed that the information gathered from such studies will facilitate the development of rational design approaches, so that targeted morphologies may be obtained, in order to produce more efficient organic electronic devices.

1.1 Thermodynamics of polymer blends

In order to understand the phase behaviour of polymer blends, we will first consider the simpler case of two liquids, which may be described by the regular solution model. This model is a Mean-field theory, which is to treat individual molecules (or polymer chains) as if they where to experience a uniform environment wherever they might be in their particular medium.(2)(3) Using this model we will derive an expression to predict the Gibbs free energy of mixing that will enable us to determine whether the system is miscible or phase separates.

If two liquids (a and b) exist in two distinct separate unmixed states their free energy may be written as $G_a + G_b$, whilst the free energy of the mixed state may be written as G_{ab}. The Gibbs free energy of mixing, ΔG_{mix} may be written as:

$$\Delta G_{mix} = G_{ab} - (G_a + G_b) \qquad (1.1)$$

In order to make predictions of the phase behaviour of the species *a* and *b* we must be able calculate the change in ΔG_{mix}, as a function of both composition (in terms of the volume fraction, $\emptyset$ and temperature, *T*. In order to do so, the change in the entropy of mixing, S_{mix} and the change of energy upon mixing U_{mix} must be calculated.

To find the change in entropy, we imagine that the molecules of the two liquids are arranged on a lattice, with each lattice site possessing *z* nearest neighbours. The volume fraction of *a* molecules, $\emptyset_a$ is defined as the volume of *a* molecules divided by the volume of the system (with the same applying for *b* molecules). We assume that the volume of the system remains constant, independent of composition, so $\emptyset_a + \emptyset_b = 1$ (as will be the case if the mixture is incompressible) and that *a* and *b* molecules occupy the same volume. In order to derive the free energies we will introduce a simple statistical model that enables us to predict the probability of finding the molecules *a* and *b* on a given lattice site. Given the volume fractions $\emptyset_a$and $\emptyset_b$, we do not know whether a particular lattice sites is occupied by *a* or *b* molecules.(2) The entropy per lattice site may be written using the Boltzmann formula:

$$S = -k_B \sum_i p_i ln\, p_i \qquad (1.2)$$

where the sum is taken over all the states of the system *i*, with each state possessing a probability p_i and k_B is the Boltzmann constant. In our system of two liquids, where either site being occupied by either *a* or *b* molecules, with a probability of $\emptyset_a$and $\emptyset_b$, Equation 1.2 may be written as:

$$S_{mix} = -k_B(\emptyset_a ln\emptyset_a + \emptyset_b ln\emptyset_b) \qquad (1.3)$$

This equation gives us the entropy of mixing and is based on the assumption that neighbouring sites are independent of each other, i.e. if one site is occupied by a b molecule it is neither more or less likely that a neighbouring site is similarly occupied.(2)

In order to find the energy of mixing U_{mix}, we assume that the molecules only interact with their nearest neighbours in a way that is pairwise additive, so the energy of interaction between two neighbouring a molecules is $\in_{aa}$, two neighbouring b molecules is $\in_{bb}$ and neighbouring a and b molecules $\in_{ab}$. Using a mean field approach we assume that a given site has $z\emptyset_a$ a neighbours, $z\emptyset_b$ b neighbours, independent of whether the site is occupied by a or b molecules. Using this assumption the energy per lattice site may be written as, $\frac{z}{2}(\emptyset_a^2 \in_{aa} + \emptyset_b^2 \in_{bb} + 2\emptyset_a\emptyset_b \in_{ab})$. By subtracting the energy per lattice site from the energy of the unmixed state (which is given by, $\frac{z}{2}(\emptyset_a \in_{aa} + \emptyset_b \in_{bb})$) we may obtain the energy of mixing: (2)

$$U_{mix} = \frac{z}{2}\left((\emptyset_a^2 - \emptyset_a) \in_{aa} + (\emptyset_b^2 - \emptyset_b) \in_{bb} + 2\emptyset_a\emptyset_b \in_{ab}\right) \qquad (1.4)$$

This equation can be simplified by introducing a single, dimensionless parameter χ, which characterises the strength of the energetic interaction between a and b, relative to their self-interactions. This interaction parameter χ is given as:

$$\chi = \frac{z}{2k_BT}(2 \in_{ab} - \in_{aa} - \in_{bb}) \qquad (1.5)$$

and is the energy change (in units of k_BT), when a molecule of a is taken from an environment of pure a and placed in an environment of pure b. Therefore U_{mix} may be simplified to:

$$U_{mix} = \chi\emptyset_a\emptyset_b \qquad (1.6)$$

Using the equation for the Gibbs free energy $\Delta G = \Delta U - T\Delta S$ and combing Equations 1.3 and 1.6, the Gibbs free energy of mixing is given as:

$$\frac{G_{mix}}{k_B T} = \emptyset_a ln\emptyset_a + \emptyset_b ln\emptyset_b + \chi\emptyset_a\emptyset_b \qquad (1.7)$$

This expression enables us to calculate the Gibbs free energy of mixing for a system of two liquids. This thesis is concerned with understanding the phase behaviour of polymer blends, as such Equation 1.7, must be modified to deal with polymers.

For a system containing two polymers (*a* and *b*), each polymer will posses a degree of polymerisation *N*, when the number of monomer units is increased from 1 to *N*, the entropic component of the Gibbs free energy remains the same (as a single site in space is either occupied by a molecule of *a* with a probability of $\emptyset_a$, or by a molecule of *b* with a probability of $\emptyset_b$), whilst the energetic component of the Gibbs free energy will increase by a factor of *N*. The Gibbs free energy of mixing per polymer molecule may be written as: (2)

$$\frac{G_{pol}^{mol}}{k_B T} = \emptyset_a ln\emptyset_a + \emptyset_b ln\emptyset_b + N\chi\theta_a\emptyset_b \qquad (1.8)$$

The Gibbs free energy of mixing for a blend of two polymers is more commonly written in terms of per monomer unit, rather than per polymer molecule is commonly referred to as the Flory-Huggins free energy: (2)

$$\frac{G_{pol}^{site}}{k_B T} = \frac{\emptyset_a}{N} ln\emptyset_a + \frac{\emptyset_b}{N} ln\emptyset_b + N\chi\theta_a\emptyset_b \qquad (1.9)$$

The interaction parameter χ is usually greater than zero, so this term acts to separate the polymers into separate phases. Conversely, the first two terms represent the entropy of mixing, act to mix polymers of different types. For polymer blends the entropy of mixing is proportional to the inverse of the number of monomers and so is very small. Thus, unless χ is very small, phase separation is

very common for polymer blends. The phase behaviour of a polymer blend may be understood by plotting the free energy of mixing as a function of composition using Equation 1.9, for an arbitrary blend of polymers, where $N_a = N_b = 10$ and $\chi = 0.015$, 0.02, 0.025 and 0.035 and is shown in Figure 1.1. The curve with $\chi < 0.02$ is concave, with a single minima, whilst curves where $\chi > 0.02$ exhibit one maximum with two inflection points.

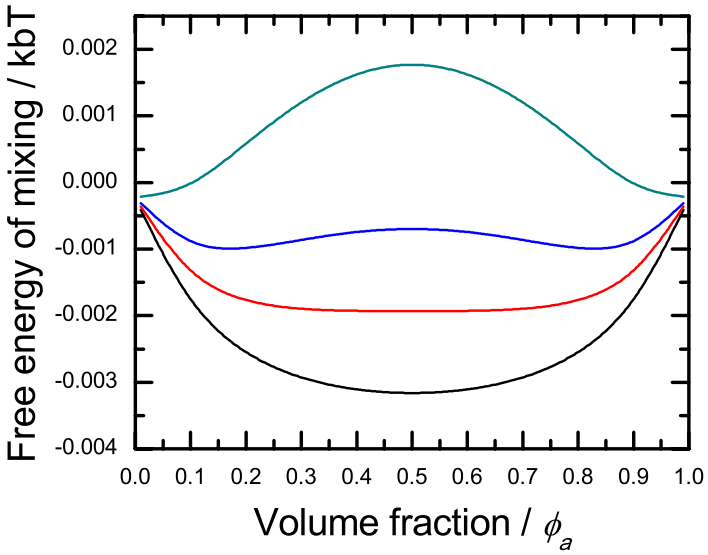

Figure 1.1. Gibbs free energy of mixing as a function of volume fraction for $\chi = 0.035$ (cyan), 0.025 (blue), 0.02 (red) and 0.015 (black), where $N_a = N_b = 100$.

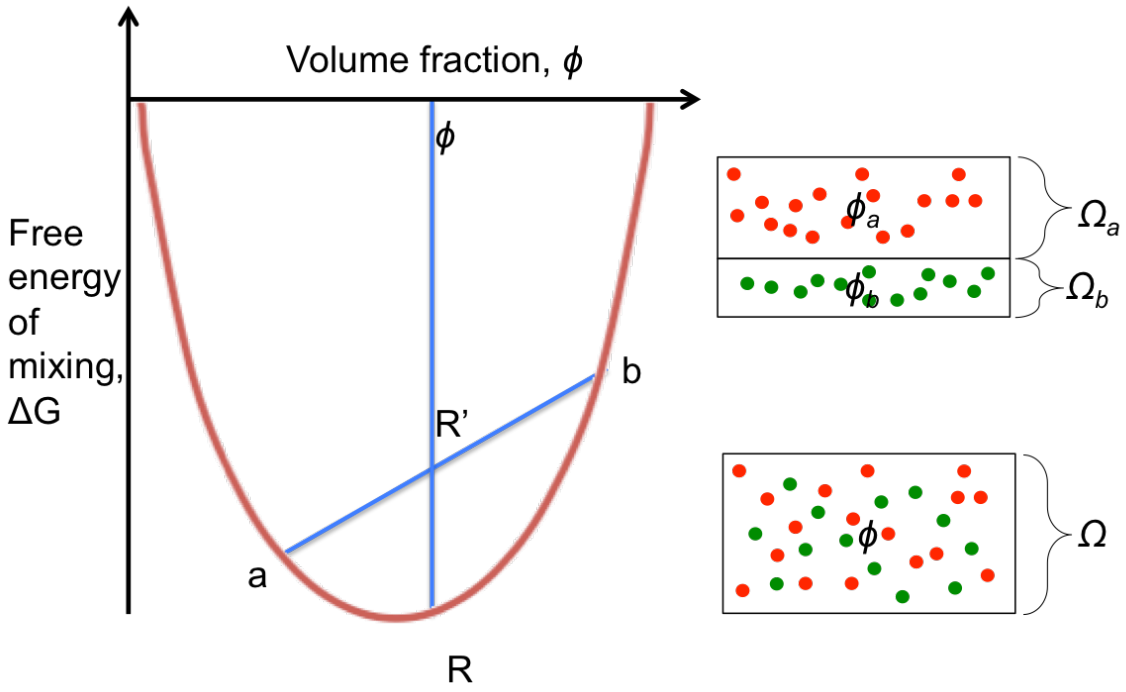

Figure 1.2. Free energy curve for the case where blend is stable at all compositions.

Figure 1.2 shows the free energy curve for the case when $\chi < \chi_c$, for a system with a starting volume Ω, where the volume fraction of polymer a is ϕ and polymer b is $\phi - 1$, as the blend is symmetric. Providing the system remains in the homogenous mixed state, the free energy of mixing is given by Equation 1.9, which corresponds to point R, Figure 1.2. If the solution were to separate into two distinct phases, a and b, with volume fractions ϕ_a and ϕ_b, respectively. Following the conservation of mass and volume, the volumes of these phases would be given by:(4)

$$\Omega\phi = \Omega_a\phi_a + \Omega_b\phi_b \tag{1.10}$$

$$1 = \Omega_a + \Omega_b \tag{1.11}$$

The total energy of the phase separated system may be given by:

$$\Delta G_{sep} = \Omega_a \Delta G_{mix}(\phi_a) + \Omega_b \Delta G_{mix}(\phi_b)$$

$$\Delta G_{sep} = \frac{\phi - \phi_b}{\phi_a - \phi_b}\Delta G_{mix}(\phi_a) + \frac{\phi - \phi_a}{\phi_a - \phi_b}\Delta G_{mix}(\phi_b) \tag{1.12}$$

Which corresponds to point R' in Figure 1.2 and has a higher energy than the miscible state R. For a concave free energy curve, separation from a homogenous mixed phase to form two separate phases will always result in an higher free energy and as such the system will be miscible at all compositions.

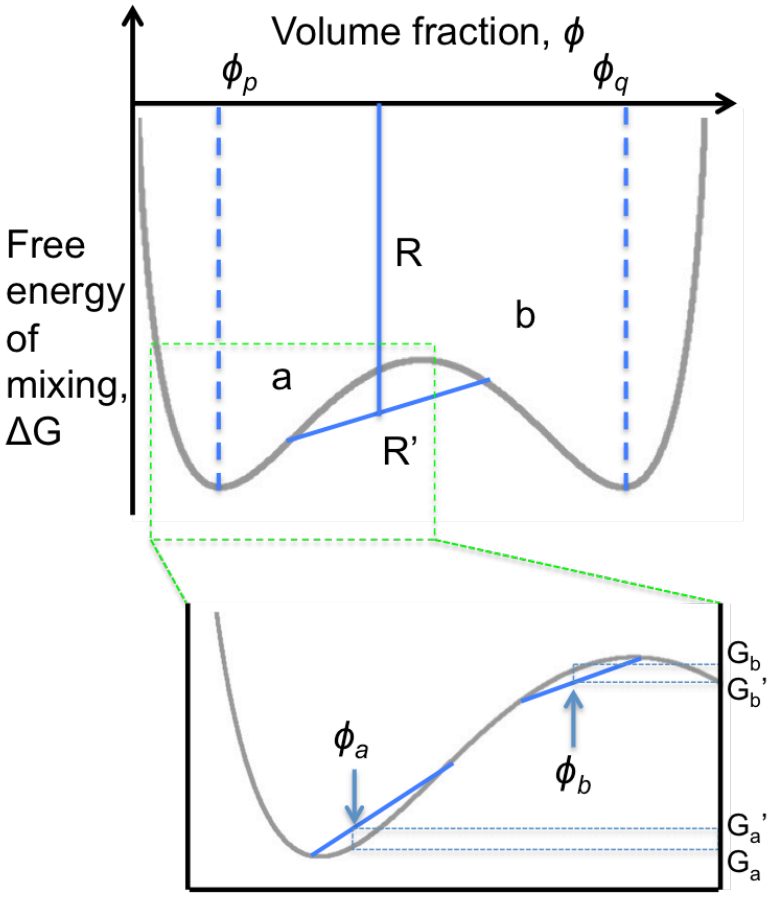

Figure 1.3. Free energy curve for the case where phase separation is favourable. Enlarged section showing the distinction between regions that are metastable ϕ_a, and those that are unstable ϕ_b.

If the free energy curve is convex, as in Figure 1.3, then there will be some starting compositions, which if they phase separate, will result in a lowering of the Gibbs free energy of the system. The transition from R to R', resulting in the formation of two coexisting phases, a and b is shown in Figure 1.3. The locus of the points satisfying $dG/d\emptyset = 0$, as a function of temperature is known as the bimodal.(2)

The curvature of the Gibbs free energy function $d^2G/d\emptyset^2$ may either be either positive or negative. This is shown in Figure 1.3, where at a composition of ϕ_b the transition from G_b to G_b', is favourable due to the decrease in the free energy of the system. As such this composition is unstable. However, at a composition of ϕ_a the transition from G_a to G_a requires an increase in energy, in order to access a composition at a global energy minima. Therefore in this case the system is locally stable with respect to small composition fluctuations. However, the system will be globally unstable, but requires an activation energy to be surmounted in order to separate into two separate phases. Such compositions are termed metastable. The limit of local stability is defined by the condition that the curveture of $d^2G/d\emptyset^2 = 0$; the locus of these points is known as the spinodal.(2) The critical point is defined as the curveture where $d^3G/d\emptyset^3 = 0$ and is the point where the coexistence curve and spinodal meet.

For a polymer blend the value of the critical interaction parameter χ_c is given by:

$$\chi_c = \frac{1}{2}\left(\frac{1}{\sqrt{N_a}} + \frac{1}{\sqrt{N_b}}\right) \tag{1.13}$$

For $\chi < \chi_c$, both polymers are miscible, whilst for the case where $\chi > \chi_c$ phase separation will occur.(3) The critical composition where the miscibility gap begins is located at:

$$\phi_c = \left(1 + \sqrt{\frac{N_a}{N_b}}\right)^{-1} \tag{1.14}$$

Knowledge of the relationship between the shape of the free energy of mixing as a function of composition and the phase behaviour of the mixture allows

construction of a phase diagram. A generic phase diagram for a symmetrical polymer melt (where, $N_a = N_b$) is shown in Figure 1.4, illustrating the stable, metastable and unstable regions. Such a phase diagram allows predictions to be made as to how a mixture of two polymers at a particular composition will behave when the system is quenched from one region to another. In the case of an asymmetrical polymer blend where $N_a \neq N_b$ the phase diagram will be asymmetric,(5) possessing a critical composition, ϕ_c that is no longer at 0.5.

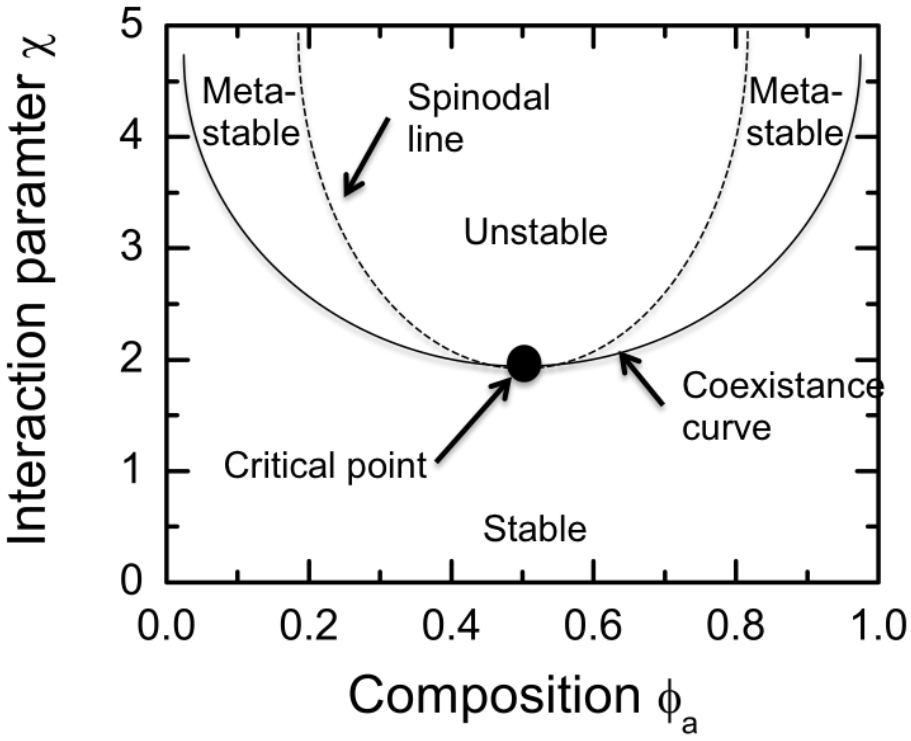

Figure 1.4. Generic phase diagram of a symmetrical polymer blend showing the stable, meta-stable and unstable regions.

When a binary polymer blend (polymer *a* and polymer *b*) is processed from the melt the system is miscible at high temperatures. When the system is quenched from a high temperature to a lower temperature the system will lie within either a metastable or unstable region where phase separation processes will occur, resulting in the formation of well-defined morphologies. Such melt processing methods are often not appropriate for polymers that may thermally decompose at

high temperature, such as the highly conjugated polymers employed in organic electronic applications. Solution casting, where two polymers are dissolved in a common solvent, which is subsequently removed via evaporation, offers an alternative processing route that negates the need for high temperatures.

The Gibbs free energy of mixing for a binary mixture (Equation 1.9) may be expanded for a ternary system containing two polymers (a and b, respectively) and solvent (s) as:

$$\frac{\Delta G}{nk_BT} = \frac{\phi_a}{N_a}\ln(\phi_a) + \frac{\phi_b}{N_b}\ln(\phi_b) + \phi_s \ln(\phi_s) + \chi_{ab}\phi_a\phi_b + \chi_{as}\phi_a\phi_s + \chi_{bs}\phi_b\phi_s \quad (1.15)$$

Providing the solvent employed is good for both polymers, the ternary system can be simplified as a pseudo-binary system, where the system may be described as a solution of polymer a and a solution of polymer b. In such a system, the solvent acts to lower the amount of unfavourable interactions between the polymers and the system will form homogenous single phase.(6) As solvent is removed from the system, interactions between the polymers increase, and at a critical value the mixture will become immiscible and phase separate. The case of evaporating solvent from the system is therefore analogous to the temperature quench. The phase diagram for ternary systems is often plotted as a two dimensional triangle, with a component at each corner, as shown in Figure 1.5.

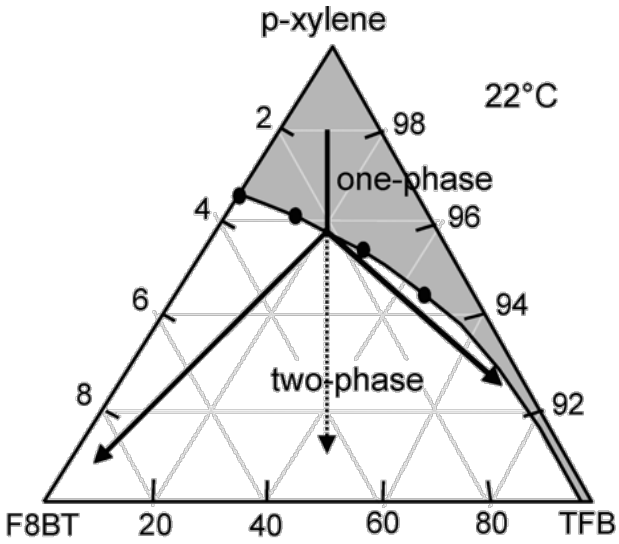

Figure 1.5. Theoretical phase diagram for ternary blend system (F8BT + TFB + p-xylene) and the chemical structures of F8BT, poly(2,7-(9,9-di-n-octylfluorene)-alt-benzothiadiazole), and TFB, poly(2,7-(9,9-di-n-octylfluorene)-alt-(1,4-phenylene-((4-sec-butylphenyl)imino)-1,4-phenylene)). Taken from reference (7).

1.2 Phase transitions

Phase separation occurs when a system undergoes a change in temperature, interaction parameter or composition, pushing the system from the stable region of the phase diagram into either the metastable or unstable regions of the phase diagram. The following section discusses the different mechanisms of phase separation, which depend upon the "quench", from the stable to the metastable or unstable regions.

1.2.1 Nucleation and growth

As stated in the previous section a polymer blend quenched into the metastable region of the phase diagram is stable with respect to small composition fluctuations. Phase separation under this regime occurs when a drop of the minority phase spontaneously comes into being within the coexisting phase, which must then subsequently grow to reduce the free energy of the system.(2) This

process is usually initiated through either thermal fluctuation or the existence of impurities in the system.(3)

1.2.2 Spinodal decomposition

When a polymer blend is quenched to the unstable region, phase separation occurs via spinodal decomposition. In this case the system is sensitive to composition fluctuation and any small changes in composition are amplified, resulting in the formation of a phase separated morphology, lying at a coexisting region.(2) This mechanism differs from that of nucleation, in that phase separation occurs uniformly throughout the material, as opposed to occurring at specific nucleation sites. The patterns formed via spinodal decomposition are random, but do posses a characteristic length scale. This characteristic length scale is intermediate between long and short-wavelength fluctuations and is shown in Figure 1.6. Long-wavelength fluctuations grow slowly, due to the large distance material has to diffuse from a peak to a trough. Where as, short-wavelength fluctuations generate a large increase in interface, with a corresponding free energy penalty and therefore do not grow.(2) An intermediate-wavelength fluctuation therefore grows the fastest, which depends upon the interplay between enthalpy and entropy.

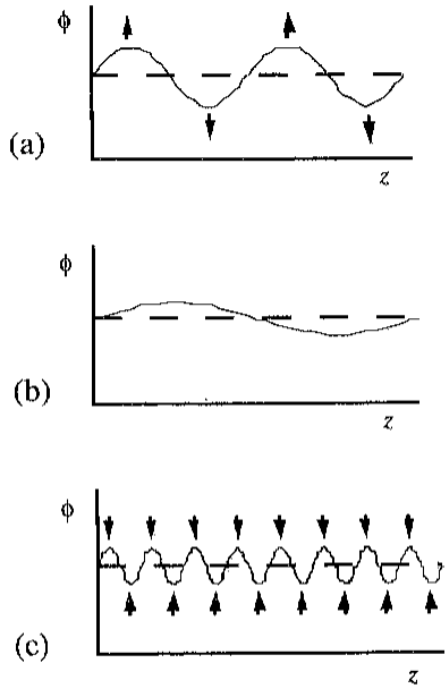

Figure 1.6. Schematic showing why concentration fluctuations of an intermediate length scale grow fastest a) an intermediate length scale, b) long wavelength fluctuation and c) small wavelength fluctuation. Taken from reference (2).

The formation of a dominant wavelength fluctuation results in the formation of a morphology with an average domain size, *R(t)*, separated by an interface with a width *w(t)*. How *R(t)* and *w(t)* evolve with time is illustrated in Figure 1.7. Initially, during the early stages of spinodal decomposition, all interfaces are essentially identical and grow in accordance with the dominant wavelength fluctuation. At an intermediate stage, where the system approaches a co-existing composition, *R(t)* increases, whilst *w(t)* decreases. Finally, the interfaces become sharp at their equilibrium values, whilst *R(t)* continues to increase. This latter process is known as coarsening and will be discussed in greater detail in the following section.(2)

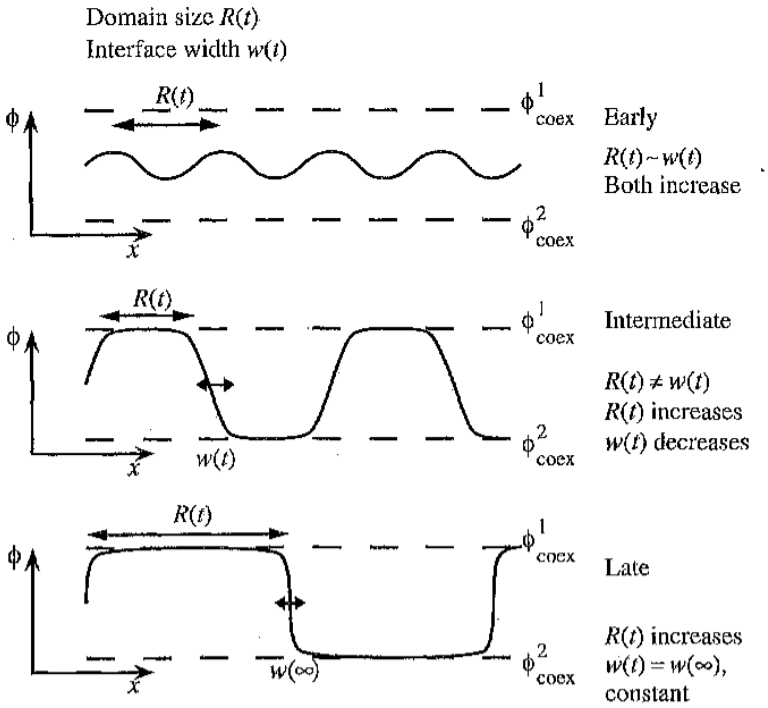

Figure 1.7. Composition profiles illustrating the evolution of the average domain size, *R(t)* and interfacial width, *w(t)* change with time for a system undergoing spinodal decomposition. Taken from reference (2).

The dynamics of spinodal decomposition may be described by the Cahn-Hilliard equation, which is a modified diffusion equation.(2)(8-10) Cahn-Hilliard theory has been extended to polymer melts using Flory-Huggins theory by de Gennes,(11) Pincus(12) and Binder(13) and has been extensively utilised to model spinodal decomposition in polymer blends.(14)

1.2.3 Coarsening and coalescence

Independent of the initial process of phase separation, be it nucleation and growth or spinodal decomposition, the domains formed will subsequently grow and coalesce, which is driven by the decrease in interfacial energy associated with larger domains. As such, the morphology observed is simply a magnification of an earlier morphology.(2)

When the morphology of the system comprises of a number of discrete islands of polymer *a*, within a matrix of polymer *b*, (or vice versa) diffusional mass transfer occurs from regions of high interfacial curvature to regions of low interfacial curvature and larger domains grow at the expense of small domains. This process where smaller domains are absorbed into larger domains is known as coarsening or Ostwald Ripening, which is depicted in Figure 1.8.(15)

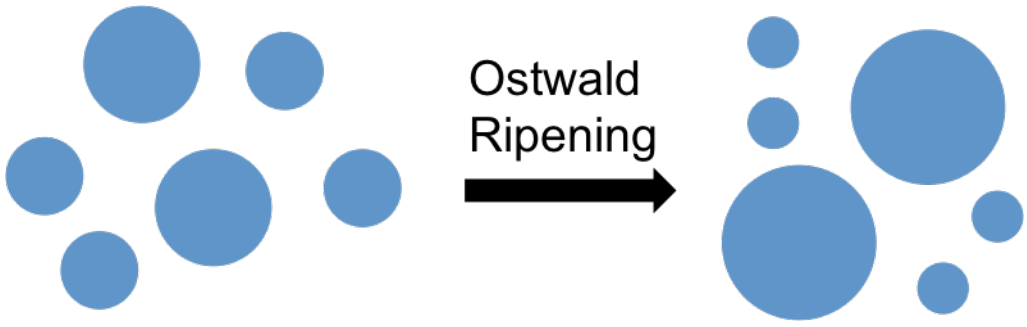

Figure 1.8. Droplet morphology before and after Ostwald ripening.

1.2.4 Polydispersity effects

So far polymer chains have been considered to be completely monodisperse. However, the majority of polymers employed in organic electronic devices are highly polydisperse, possessing a wide molecular weight distribution, due to complex/sensitive synthesis routes. A polymers polydispersity may be characterised by the moments of the molecular weight distribution function, namely, the number average molecular weight (M_n), weight averaged (M_w) and the z averaged (M_z), which are defined as:,

$$M_n = \frac{\sum N_i M_i}{\sum N_i}, \tag{1.16}$$

$$M_w = \frac{\sum N_i {M_i}^2}{\sum N_i M_i}, \tag{1.17}$$

$$M_z = \frac{\sum N_i {M_i}^3}{\sum N_i {M_i}^2} \tag{1.18}$$

where N_i is the number of polymer chains with a molecular weight M_i.

A number of theoretical studies have extended the Cahn-Hilliard theory of spinodal decomposition to allow for polydisperse components.(16, 17) Clarke showed that the of the growth rate of the reciprocal length scale of phase separation (Q) is commensurate with the behavior of monodisperse systems and that for shallow quenches through the phase diagram the early stages of spinodal decomposition are slower for more polydisperse polymers.(18) Mumbay and Sher derived an equation for the critical point, for a polydisperse binary sytem, where both polymer components *(a* and *b*) are polydisperse:(19)

$$\emptyset_c = \frac{M_{w,a}\sqrt{M_{z,b}}}{M_{w,b}\sqrt{M_{z,a}} + M_{w,a}\sqrt{M_{z,b}}} \qquad (1.19)$$

1.2.5 Crystallisation

A crystal is built up of regularly repeating 'structural motifs', which may be atoms, molecules or groups of atoms, molecules.(20) Crystallisation may occur in polymers depending upon their architecture. For example, polystyrene may crystallise depending upon its tacticity. Atactic polystyrene (Figure 1.9a) has phenyl side groups randomly orientated about the chiral centres along the polymer backbone. These random orientations disrupt packing and thus inhibit crystallisation. Isotactic polystyrene (Figure 1.9b) readily crystallises, as all of the phenyl side group lie at the same position on each monomer.(3)

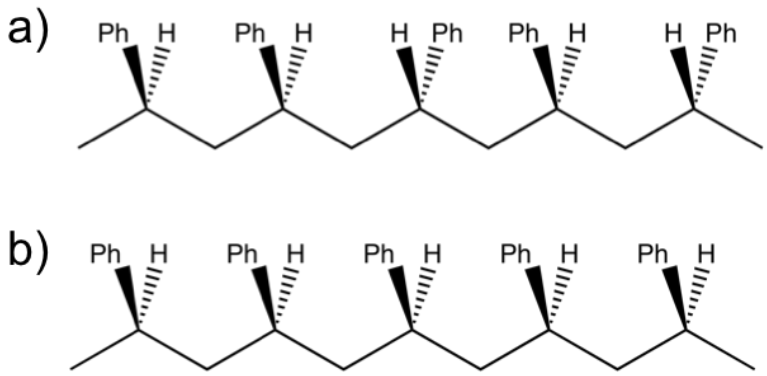

Figure 1.9. Structures of a) atactic polystyrene, b) isotactic polystyrene.

Specific interactions such as hydrogen bonding and π-π stacking tend to promote crystallinity.(21) Many conjugated polymers posses solubilising alkyl side groups, which may intermesh (as shown in Figure 1.10), leading to ordering between polymer chains However, it also possible that alkyl sidegroups may disrupt the packing of the main chain. Polymers are semi-crystalline as different portions along the chain are able to participate with different initial nuclei, prohibiting the formation of a perfect polymer crystal.(22)

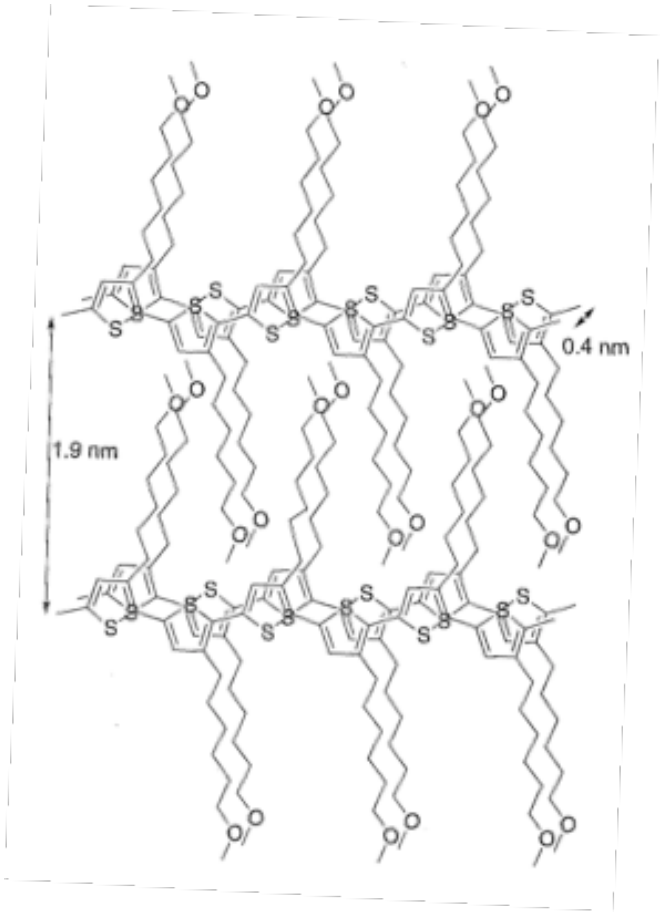

Figure 1.10. Regio-regular poly[(3-hexylmethoxy)thiophene] showing how the alkyl chains between polymers may intermesh and π-π stacking of aryl units. Taken from and adapted from reference (3).

The basic unit of polymer crystals is the chain-folded lamella, possessing a lamellar thickness *l*, much smaller then the chain length (shown in Figure 1.11a). Lamella organise into higher order structures known as spherulites, comprising of sheaves of individual lamella that radiate and branch from a central nucleus (shown in Figure 1.11b). (23)

Chain folded lamella form through a process involving the straightening and subsequent packing of portions of polymer chains. An optimum lamella thickness *l*, is observed owing to the balance between the entropic drive to reduce extensive chain straightening (which would produce thick lamellae) and the energetic desire to minimise excessive interfacial energy and unfavourable interactions from

surface folds (resulting from thin lamellae).(2) The free energy curve of this process is shown in Figure 1.12.

Polymers may also form fibrillar crystallites, provided they are subjected to sufficient shear. Fibrils may act as distinct crystallisation sites, resulting in the formation of an "shish-kebab" morphology.

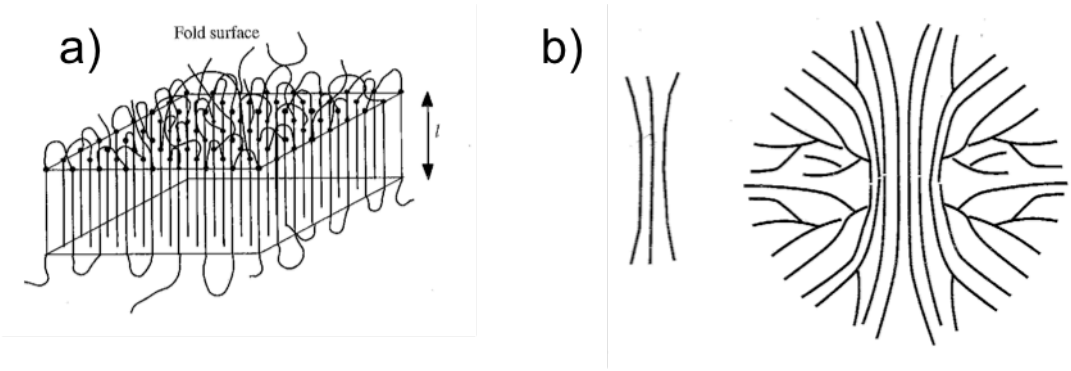

Figure 1.11. Schematic showing a) chain-folded lamella, with a thickness *l* and b) how lamellae may arrange, branching from a central nucleus, forming a spherulite. Taken and adapted from reference (2).

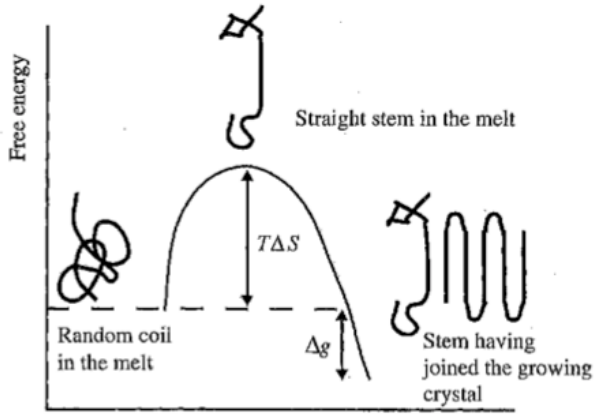

Figure 1.12. Schematic showing how the Free energy changes when a stem of polymer joins a growing crystal. Taken from reference (2).

1.2.6 Marangoni effects

When thin layers of fluid (open to the air) are heated from below, hexagonal patterns of convective cells form. Such patterns where first observed by Bérnard in

1900 and are shown in Figure 1.14.(24, 25) This effect was originally attributed to buoyancy-driven convection and was confirmed by the theoretical work of Rayleigh.(26)

The free surface, at the air-fluid interface has a surface tension, which can come to exert a dominant influence on pattern formation. The surface tension of a liquid is inversely proportional to temperature and so if the temperature of a liquid varies spatially, surface flows may be set-up because regions of higher surface tension (cooler regions) pull warmer regions up to the surface. When there is heterogeneity in the horizontal balance of surface tension, result in a surface flow forming hexagonal patterns, where fluid is pulled up from below to replace that which is pulled laterally across the surface to regions of higher surface tension.(27) Such surface tension gradients where studied in the nineteenth by Marangoni and are termed Marangoni effects.

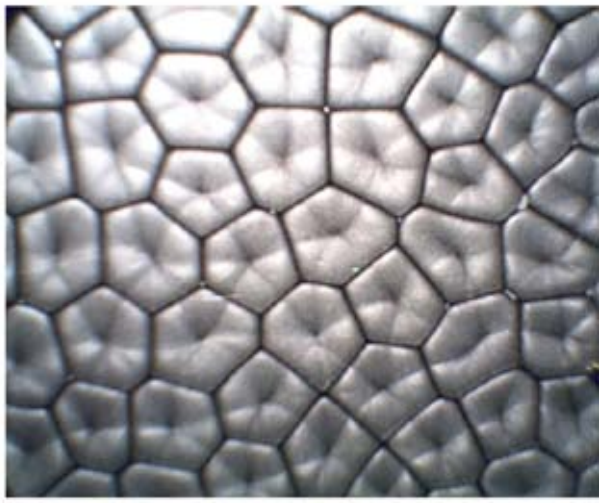

Figure 1.13. Shows an image of Bérnard cells, induced through Marangoni flows. Taken from reference (25).

1.2.7 Colloidal ordering

So far we have considered how polymer melts and solutions may order via phase separation and crystallisation. Colloidal dispersions, where polymer particles (<10 μm) are dispersed in a liquid medium may similarly self-assemble to form two or three-dimensional periodic structures known as colloidal crystals or synthetic opals. These structures often posses significant long-range order and will diffract light of similar wavelengths to the structure, resulting in striking opalescent interference effects(2) and have potential applications in optical devices/switches,(28-31) as macroporous templates,(32) and as monolayers for nanolithography.(33)

Colloidal dispersions posses a rich variety of phase behavior, mimicking that of simple atomic liquids and solids, where as the particle concentration is increased transitions from colloidal fluid, to fluid and crystal coexisting phases to full crystallization may be observed,(34) which can be described by an effective hard-sphere model.(2)

The hard-sphere model considers an assembly of perfect spheres that interact with an energy potential of zero, unless they overlap, in which case the energy potential is infinite. As a result the Boltzmann weights may either be unity or zero, independent of temperature and so any ordering of the system is driven purely by entropy. The maximum obtainable volume fraction of random close packing is around 0.63. Whereas, for a regular close packed structure the maximum volume fraction is 0.74. Therefore at high volume fractions packing constraints force the system to adopt a more ordered structure. It has been shown that regular close packed structures form at much lower volume fractions than 0.74 and that at a volume fraction of 0.49 there is an abrupt transition to a crystal

with a volume fraction of 0.55.(2, 34) This transition is dictated by the difference in entropy between the random and regular close packed structures. Despite the loss of entropy when the system undergoes the a transition from random close packing (liquid) to regular close packing (crystalline) owing to the long range order, due to the difference in densities of the two structures the regular close packed structure allows each individual sphere more space locally. Thus regular close packing is more entropically favourable than the random close packing. Such transitions from liquid (isotropic) to crystalline may occur when the concentration of a colloidal dispersion is increased, when the dispersing liquid is allowed to evaporate.

There are two different forms of close packed structures, face-centred cubic (FCC) and hexagonal close packed (HCP), which both posses the maximum packing density. FCC and HCP structures differ in the way subsequent layers are positioned on top of the first layer. The layers of a HCP structure are positioned ABABAB…, whilst the layers of an FCC structure are positioned ABCABC…, as illustrated in Figure 1.14. Colloidal crystals most readily adopt HCP structures, with a random sequence of close-packed planes, possessing a large number of stacking faults.(2)

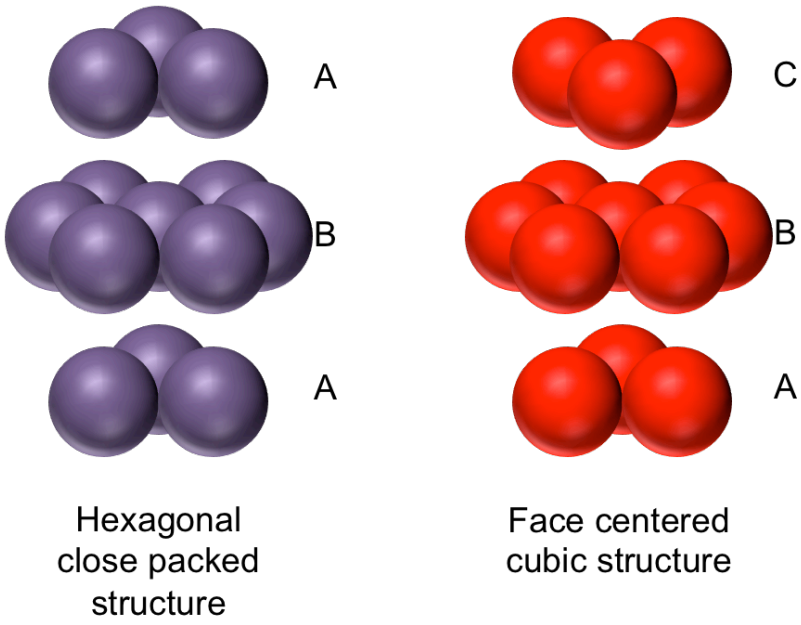

Figure 1.14. Schematic showing hexagonal close packed and face centered regular close packed structures, illustrating how hexagonal structures are layered A, B, A, whilst face centred cubic structures are layered A, B, C.

Well ordered two dimensional particle arrays often spontaneously form when a colloidal dispersion is deposited on a solid substrate, where the self-assembly of particles may occur via convective assembly. This process involves the formation of crystal nucleus through attractive capillary forces, and subsequent crystal growth driven by convective particle flux caused by water evaporation from the ordered crystalline regions.(35) In addition to well ordered two dimensional arrays, colloids may form well ordered two and three dimensional rings which may order via two different mechanisms. The most common of these mechanisms is responsible for the "coffee ring effect", where some particles will irreversibly stick to the substrate at the drop periphery under the action of capillary force, pinning the contact line, resulting in evaporation from the edge being compensated by flow from the interior, which drags suspended particles to the drop periphery.(36) Alternatively, in some cases surface forces may induce film destabilization and

hole formation. The rim of the expanding hole in the wetting film drags the particles away, arranging them into annular rings.(37)

In addition to the HCP and FCC structures a large number of other crystal morphologies may be adopted through employing binary colloidal dispersions, containing particles with two distinct length-scales.(38) Such systems provide a convenient frame-work to study solvent evaporation induced crystallisation directly, using microscopy techniques.

1.3 Spin coating

Spin-coating is a facile thin film production technique widely employed for the fabrication of organic electronic devices such as, organic photovoltaics,(39-42) organic light emitting diodes(1) and organic field effect transistors.(43, 44) The process involves depositing a polymer solution onto a substrate that is subsequently rotated at high speed (typically between 1,000 & 10,000 rpm). Initially, film thinning occurs due to rotational forces(45) (hydrodynamic thinning) and solution is ejected from the edge of the rotating surface. At some point, due to increasing viscosities, an equilibrium is reached where hydrodynamic thinning is minimal, and instead film thinning predominantly occurs through evaporation (evaporative thinning).(46) A number of parameters affect the interplay between hydrodynamic and evaporative thinning of a polymer solution, including viscosity, vapor pressure,(47) molecular weight, acceleration rate(48) and the rotational rate.(49, 50)

Spin-coating a polymer solution (e.g. Polymer *a* + solvent) usually results in the formation of a uniform film with a continuous morphology. When ternary mixtures (e.g. Polymer *a* + Polymer *b* + Solvent) are spin-coated, often complex

processes of self-assembly take place, such as phase-separation,(51-53) crystallization,(54) stratification,(47, 55-57) and agglomeration, resulting in the formation of intricate morphologies that evolve towards thermodynamic equilibrium, but which ultimately become frozen due to rapidly increasing viscosities.(2, 47) This process is shown schematically for both binary and ternary blends in Figure 1.15. The propensity of polymer blends to self assemble, forming well-ordered morphologies during spin-coating is highly desirable, particularly for organic electronic devices, such as organic photovoltaics, where a morphology with a large amount of interface between phases and interconnectivity is required for the generation and separation of charges.(21)

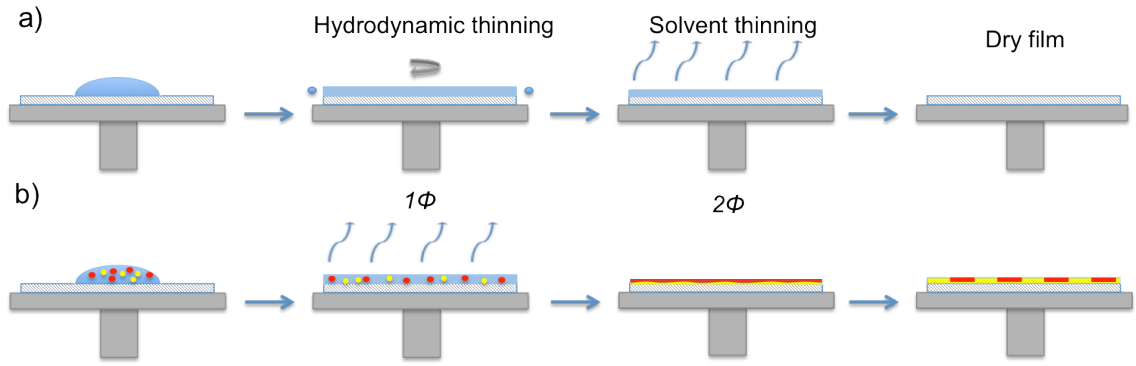

Figure 1.15. Overview of the spin-coating process for a) solvent and b) a ternary mixture consisting of two incompatible polymers dissolved in a common solvent.

There have been many attempts to model the spin coating process, the first of which was proposed by Emslie, Bonner and Peck; commonly referred to as the EBP model.[8] This consists of a viscous fluid on a rotating plane and is based on the assumptions that the fluid shows Newtonian character, the rotating plane is infinite in extent, the rotating plane is horizontal and that the liquid layer is radially symmetric so that shear resistance is only applicable in the horizontal planes. In their analysis EBP gave the thinning rate as:

$$\frac{dh}{dt} = \frac{-2\rho\omega^2 h^3}{3\eta} \tag{1.20}$$

where h is the film thickness, t is time, ρ is the solution density, ω is the rotation rate in radians per second and η is the solution viscosity in kg s^{-1} m^{-1}.

In the early stage of spin coating known as hydrodynamic thinning, the rate of thinning is sufficiently described by Equation 1.20. However, later on in the process contributions from solvent evaporation dominate film thinning behaviour. Meyerhofer was the first to estimate the effect of solvent evaporation on the thinning rate, by simply adding an evaporation term to Equation 1.20:[9]

$$\frac{dh}{dt} = \frac{-2\rho\omega^2 h^3}{3\eta} - e \tag{1.21}$$

where e is the evaporation rate [ml s^{-1} cm^{-2}] and is dependant upon the rate of rotation and the rate of diffusion through a vapour boundary layer above the spinning substrate.

Equation 1.21 was not solved analytically, instead Meyerhofer assumed spin coating was a two-stage process; where the first stage was dominated by flow and the second stage was dominated by evaporation. This assumption allowed prediction of the final coating thickness in terms of several key solution properties. Over the years this model has been improved through taking into account the concentration profile that develops in the film.[10]

1.4 Development of *in situ* studies of spin coated thin films

In situ studies have been a key tool in furthering our understanding of the self-assembly processes that occur during spin-coating. Yet despite intensive research in this area, we still do not fully understand the complex interplay between processes such as phase separation, crystallisation, self-stratification and agglomeration. A summary of the key analytical developments over the past 20 years is given in Table 1.1.

The most widely employed techniques for conducting *in situ* studies of spin coating have been based upon interferometry. For this technique a narrow bandwidth light source (usually a laser ($\Delta\lambda$ < 1nm)) is incident on the substrate and the fluctuations in specular reflectivity are recorded. Through analysis of the variations in specular reflectivity over time it is possible to extract drying rate curves using Bragg's law (constructive interference occurs when, $2nd\ cos\theta = m\lambda$, where n = refractive index of the film, d is the film thickness, θ_i is the angle of incidence relative to the normal, λ is the wavelength and m is an integer value).[14, 15] This approach is greatly simplified by many polymers having similar refractive indices to organic solvents (i.e. polystyrene = 1.592, poly(methyl methacrylate = 1.491, toluene = 1.496 at 20 °C).

The first *in situ* studies of spin coated polymer films were conducted by Graves and co-workers.(58, 59) The motivation behind the study was to understand the effect of substrate surface topography on spin-coating, as previous manufacturing steps employed in semiconductor fabrication often left an uneven surface topography on the substrate. Their strategy was to make systematic comparisons between film profiles over topography, taken during the process,

against model predictions of the wet film profile. Their experimental set-up is shown in Figure 1.16. A laser was directed onto the spinning substrate and the resultant interference patterns where recorded using a conventional 35-mm film camera. The laser and 35-mm camera where synchronised so as to image the same point once per revolution. The spin coating experiment produced a series of photographs, each showing a contour map of the thin film at a preselected point on the wafer at a certain time. The space between interference fringes showed the differences in height between two points, and not the absolute thickness.

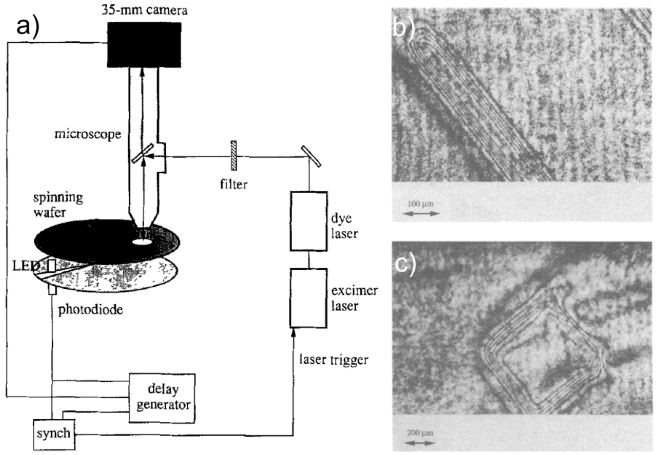

Figure 1.16. a) Schematic of set-up. As the slit on the wheel attached to the spindle passes between the light emitting diode and the photodiode, a TTL signal is sent to the synchronisation control, which triggers the excimer laser. A 20 ns pulse of light from the excimer pumped dye laser is passed to the illuminator of the microscope. The interferometric images are captured by a 35-mm camera; b) Interferogram of 50 µm line 17 s into spin; c) Interferogram of 500 µm line 1.5 s into spin-cating. Taken from reference (58).

This study indicated that an applicable model proposed by Stillwagon and Larson for spin coating over topography with azimuthal symmetry[17] was found to be in good agreement with the obtained experimental profiles of thin films. Predictions for dry profiles, assumed constant throughout the film, where found to be inaccurate for small feature sizes on substrate topography. The ability of the

technique to measure film profiles was hindered by the coherence of the laser producing speckle, internal reflections within the microscope, and the exposure time of the photographic film.

1.4.1 Specular reflectivity

Horowitz utilised an interferometric approach similar to that of Graves. However, rather than photographic, film, Horowitz's set-up utilised two photo detectors and an analogue to digital converter to record the intensity. The ratio between the reflected intensity and the incident intensity gave a value for reflectivity. An example plot of the modulating reflectance as a function of time is shown in Figure 1.18 for a spin-coated sol gel solution. (60, 61)

Table 1.1. Summary of analytical developments of *in situ* studies of spin-coating.

Year	Set-up	Source	Detector	1D / 2D	System Studied	Real / Reciprocal Space	Reference
1990	Specular reflectivity	Laser	Photographic film	2D	Photo-resists	Real	Graves *et al.* (59 & 60)
1993	Specular reflectivity	Laser	Photo-diode	1D	Silica spin-on glasses by a sol-gel method	Reciprocal	Horowitz (61)
1996	Specular reflectivity	Laser	Photo-diode	1D	Pure solvents	Reciprocal	Birnie (63)
1997	Specular reflectivity	Laser	Photo-diode	1D	Solvent mixtures	Reciprocal	Birnie (64)
2005	Specular reflectivity and off-specular laser scattering	Laser	Photo-diode & progressive scan CCD camera	2D	F8BT:PFB	Reciprocal	Jukes *et al.* (65)
2010	Colour video calibrated with laser interferometry	Laser & white light	Photo-diode & colour video camera	2D	n-propyl	Real	Birnie (72)
2011	Direct stroboscopic imaging	LED (Δλ10 nm)	EMCCD (electron-multiplying CCD) QE = 95%	2D	PS:PI	Real	Ebbens *et al.* (74)
2013	Off-specular x-ray scattering	X-ray	Pilatus 1M	2D	P3HT:PCBM	Reciprocal	Chou *et al.* (76)

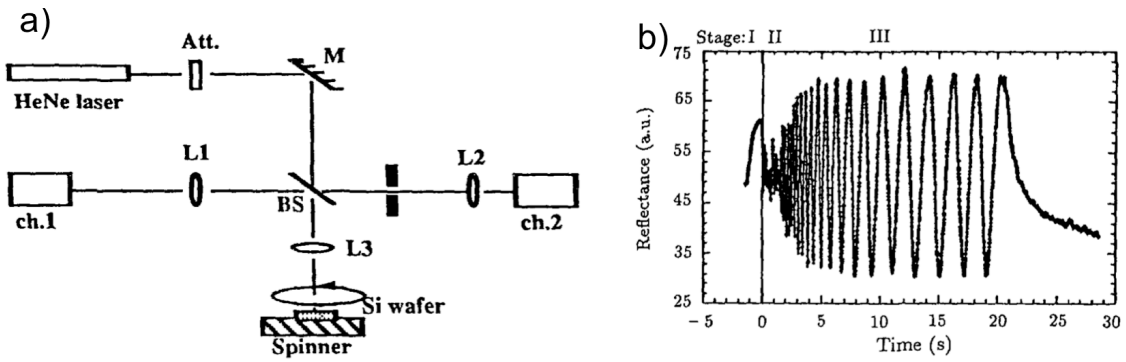

Figure 1.17. a) Double-beam experimental set-up with a He-Ne laser followed by Att. (attenuator), M. mirror, BS. Beamsplitter, L 1-3. condenser lenses, ch.1 incident intensity at photodiode 1 (reference), transmitted intensity at photodiode 2 (sample), b) "Optospinogram" for a sol-gel solution spun-cast in a saturated solvent atmosphere. Taken from reference (60).

Changes in optical thickness as a function of time where obtained from the "*optospinogram"* by counting a quarter wave every time reflectance evolved between two successive extremes. Plots of optical thickness against time for the sol-gel in air/saturated solvent atmosphere showed film thinning occurred at a faster rate for the sample in air compared to the saturated solvent atmosphere. This study indicated that the role of evaporation could not be disregarded when modelling the spin-coating process and disproved the early assumption of a separate solvent evaporation stage after convection has ceased as proposed originally by Meyerhofer.(46)

Birnie further utilised laser interferometry to study solvent thinning behaviour on spinning silicon wafers.(62) In contrast to the work of Horowitz, relative reflectivity was measured rather than absolute reflectance, to allow interference fringe counting. As the bright/dark interference fringe spacing only measured thinning rate, thickness was determined once thinning had proceeded to

a completely dry wafer by counting back from the reference point, the last intensity maximum corresponded to the time when the wafer first became dry. A plot of log thickness against log time for methanol, ethanol, butanol and butyl acetate emphasized the similarity found for solutions thinning in this geometry and is shown in Figure 1.18.

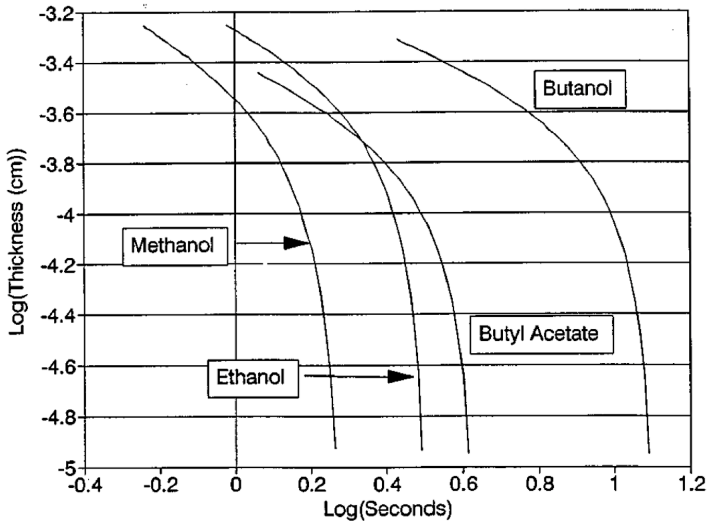

Figure 1.18. Thickness development for several volatile fluids spun-cast at 2000 rpm. Taken from reference (62).

These results indicated that the process is initially dominated by mass flow and later in the process solvent volatility dominates, as indicated by each sequence reaching the dry state. By plotting thinning rate (dh/dt) as a function of two times the cube of film thickness ($2h^3$) (Figure 1.19) (commonly referred to as a Meyerhofer plot), Birnie was able to determine both fluid viscosity and the evaporation rate for a variety of solvents. Analysis of the evaporation data substantiated an earlier conclusion of the spin-speed dependence of evaporation rate, and confirmed that evaporation rate is limited by vapour diffusion though the laminar boundary layer above the disk.(46)

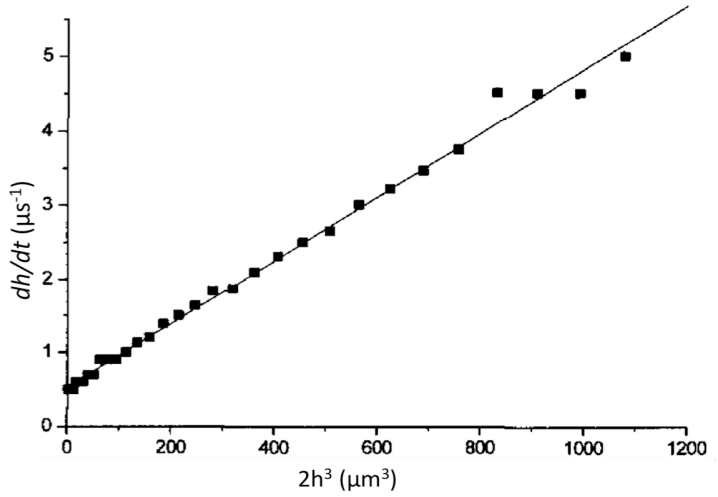

Figure 1.19. Meyerhofer plot for pure butanol spun-cast at 2000 rpm. The line is a linear regression to the observed data. Taken and modified from reference (63).

The flow behaviour was found to be largely consistent with the EBP model, however, Meyerhofer's modification was required to account for evaporating fluids. Simultaneous extraction of both flow and evaporation constants was achieved by performing a linear regression fit. Evaporation rates where found to vary as a function of the square-root of spin speed as predicted by Meyerhofer. The evaporation constants derived for several solvents showed a strong correlation between their evaporation rates and their room temperature vapour pressures, as would be expected.

Birnie followed on from this study by investigating the flow and evaporation rate of mixed solvent solutions and a sol-gel pre-cursor solution.(63) The time evolution of fluid thickness for a series of two component solutions was studied as in the previous study. Methanol-butanol mixtures where studied, due to their relative differences in volatility. In addition a sol-gel solution was tested using the same methodology, as a measure to test the effectiveness of this experimental approach to industrially relevant systems.

As in the previous study, Meyerhofer plots for pure butanol and pure methanol were linear. However, butanol-methanol mixtures exhibited more complex behaviour. Figure 1.20 shows the Meyerhofer plot of a 1:1 mixture for butanol:methanol. Two distinct regions where observed, instead of one as with pure solvents. Early on in the spinning process the slope and intercept yield viscosities and evaporation rates that are intermediates between that of pure butanol and pure methanol. The second region present, later on in the spinning process, corresponded to an evaporation rate and viscosity of that expected of pure butanol. It was assumed that this second stage represents a transition where viscosity and evaporation behaviour are both changing toward those of pure butanol. For solvent mixtures which where more unbalanced (1:9 or 9:1 – butanol:methanol) the second transition region was more difficult to resolve. This behaviour was attributed to the higher component solvent dominating both viscosity and evaporation behaviour.(63)

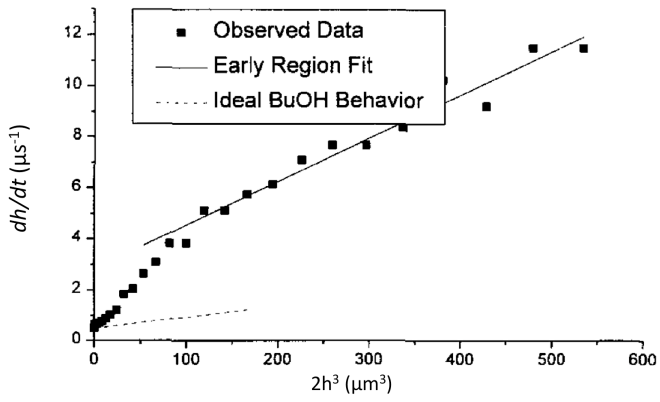

Figure 1.20. Meyerhofer plot for a 1:1 (by volume) methanol:butanol solution spun-cast at 2000 rpm. Solid line is a regression to early data points, while the dashed line shows the expected response for pure butanol. Near the end of coating process the fluid behaviour changes gradually by evaporation of methanol, leaving behind a butanol-rich liquid. Taken and modified from reference (63).

The sol-gel precursor solution showed behaviour consistent with a single thinning region (with exception to the latter data points). However, the later data points suggested that the solvent depletion effect (as observed in butanol-methanol), occurs for sol-gel coatings. Therefore the majority of the thinning behaviour may be modelled, until the final moments of the spin-coating process. Comparison of the sol-gel precursor evaporation and viscosity values to that of pure methanol and butanol, suggested that there was no substantial polymerisation of the sol-gel, during the majority of the spin coating process. However, the evaporation constant was below what might was expected for a solution with a significant fraction of methanol, which indicated that evaporation may be slowed by the formation of gel-like skin on the film surface.

Birnie hypothesised that if a volatile solvent is necessary to stabilise the precursor components, then an instability might occur before the coating has set completely, leaving behind inferior coatings. Therefore improved coating solutions may require selection of an alternate solvent system with associated modification to other solution chemical parameters. It was suggested that lower volatility solvents may be employed for the production of defect free coatings.(63)

1.4.2 Specular reflectivity combined with off-specular scattering

Jukes *et al.* integrated a light scattering set-up with a spin coater to measure both specular-reflectivity and off-specular scattering as shown in Figure 1.21.(64) Specularly reflected light was detected by a photodiode and the off-specular diffraction pattern was collected on a screen and recorded by a CCD camera. This allowed both the evolution of film thickness and the development of lateral phase separated structures to be monitored as a function of time. As in previous studies,

specular reflectivity interferometry was used to monitor changes in film thickness, while off-specular scattering allowed observation of the onset of phase-separation and subsequent length-scale evolution.

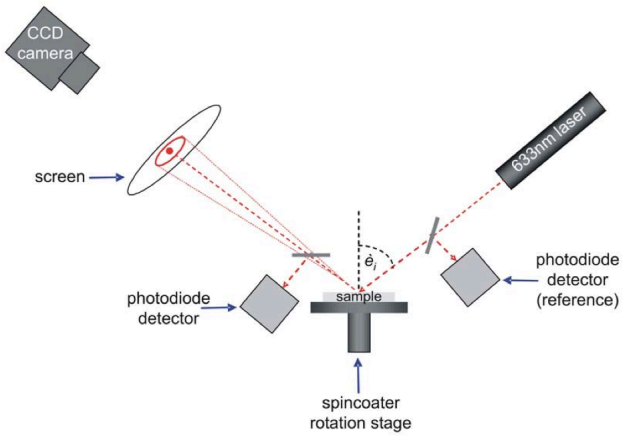

Figure 1.21. Experimental set-up for *in situ* light scattering consisting of a HeNe laser (633 nm), spin coater rotation stage, photo-diode detectors screen and a CCD camera. Taken from reference (57).

Blends of polyfluorene derivatives where studied; poly(9,9'-dioctylfluorene-co-benzothiadiazole) (F8BT) and poly(9,9-dioctylfluorene-2,7-diyl-1,4-phenylene-bis(N-(p-sec-butylphenyl) imino-1,4-phenylene) (PFB). The F8BT/PFB is a blend of two conjugated polymers (PFB is a hole acceptor and F8BT is an electron acceptor), which was of interest due to applications in blend-based photodiodes.

When the F8BT:PFB blend was spun-cast the speculary reflectivity data exhibited a series of peaks and troughs corresponding to constructive and destructive interference conditions of the reflected light as the film thickness decreased. The final film thickness was determined via AFM, which allowed deduction of the time dependence of the film thickness. A linear change in refractive index with time from the mixed polymer/solvent state to the final solid polymer film was assumed, in order to correct for the changing refractive index.

Figure 1.22 shows specular reflectivity data and a corresponding thickness-time curve extracted from this data.

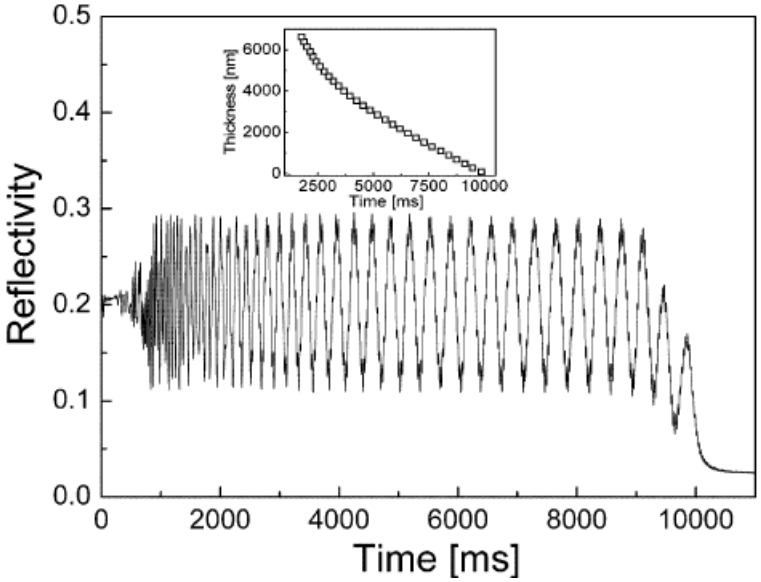

Figure 1.22. Specular reflectivity for a 44:56 F8BT:PFB blend spun-cast at 2000 rpm from a 2 wt% solution in xylene. The inset shows the thickness-time curve extracted from these data. Taken from reference (64).

The off-specular scattering data provided information on the development of lateral structure in the film and the obtained scattering patterns where radially symmetric throughout the phase-separation process. Figure 1.23 shows radially averaged scattering data as a function of time, from the first frame where significant scatter is observed (9.2 s), until scattering pattern ceases to evolve (10.2 s) due to the formation of a solid film as vitrification occurs. The point at which the scattering was first detected corresponded to the cloudpoint, i.e. the onset of lateral phase separation in the system. At the cloudpoint there was no drop in the specular reflectivity intensity (Figure 1.22), showing that it is not possible to detect phase separation via reflectivity alone and also indicating that multiple scattering events where not likely to be a significant complication.

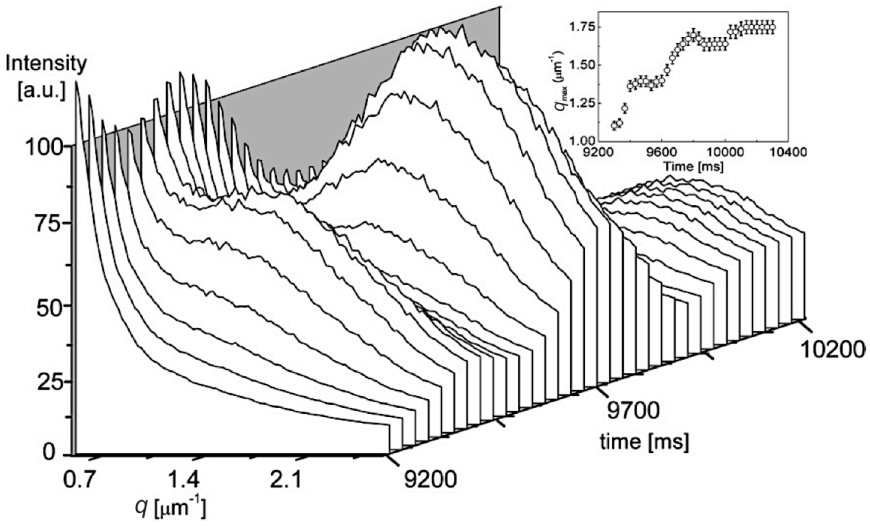

Figure 1.23. *In situ* light scattering taken during the spin-coating of a 44:56 F8BT:PFB blend from a 2 wt% solution in xylene at 2000 rpm. The data shown are for a portion of the spinning event from the "cloud point" to the point where the length scale stops evolving. The inset shows the time dependence of the peak wavevector q_{max}. Taken from reference (64).

The scattering data showed two prominent features; firstly, scattering exhibited pulsations in intensity with a periodicity mirroring the oscillating specular reflectivity intensity. Intereference effects occurring due to film thinning therefore affect both specular reflecivity and off-sepcular scattering. By accounting for the subsequent periodic modulation of overall scattering intensity, the scattering curves initially showed a strong similarity with that would arise from the scattering in bulk phase separation systems. A scattering peak, characterised by a well-defined intensity maximum, grows smoothly out of the background, in a way strongly reminiscent of spinodal decomposition.(64) However, as phase separation proceeds, the behaviour deviated from that of conventional bulk separation. Figure 1.23 inset shows that the q value of maximum scattering as a function of time, q_{max} moved to a higher value as phase separation proceeded, implying that the overall length scale decreased as phase separation. Further

analysis of Figure 1.23 showed that the average size of the phase separated domains (as deduced from q_{max}), is initialy 5.7 μm, rapidly shrinking to a final size of ~ 3.6 μm. This result was in stark contrast to behaviour seen in the bulk, where q_{max} decreases (lengthscale increases) as a result of coarsening as discussed in Section 1.2.3. The size of the domains roughly followed a $t^{1/2}$ dependence on the spinning time. The result was surprising as it directly contradicted the model proposed by Walheim *et al*, where domains nucleate from the initially homogeneous mixture below a critical solvent concentration and the grow until their size reaches the thickness of the film.(51)

The proposed explanation for these results was that an initial lateral structure may form, (not from bulk-like phase separation within the film), as a result of an instability in transient wetting layers at the surface and substrate. The spinning fluid may initially form a layered structure, driven by the difference in surface energy between the two polymer solutions. As the solvent evaporates, surface and interfacial tensions that stabilise the configuration are continuously changing, resulting in the development of interfacial instabilities (the origin of which was not clear). These instabilities lead to dewetting and breakup of the layered arrangement and the development of the lateral domain structure with an exact morphology dependent on the initial composition of the blend. The lateral structure is detected as soon as the layers began to break up.

Evidence in support of this proposed mechanism came from reports that spin-coating the same polymers from isodurene, a highly viscous and volatile solvent results in the formation of a bilayer with the lower surface energy F8BT on top.(65) In this instance the structural evolution was frozen at the layered stage before lateral domains can develop. More direct evidence of this layering during

the spin coating process was found through detailed analysis of the time dependence of specular reflectivity in blends of polystyrene:polyisoprene.(66)

This study showed that the dynamics of phase separation occurring during the spin-coating of polymer blends may be studied *in situ* via light scattering techniques. The results of this experiment where explained by two possible mechanisms: one in which morphology arose by the unstable growth of either a composition fluctuation and another in which the morphology results from an interfacial instability initiated by the loss of solvent. A single length scale is initially selected, but contrary to the normal situation in bulk spinodal decomposition following a temperature quench, this length scales subsequently appears to shrink rather than grow.

Using this technique Heriot and Jones went on to investigate phase separation in a model polymer blends system,(57) Specular reflectivity data was obtained for both pure PMMA and a PS:PMMA (1:1) blend and the off-specular scattering was plotted as a intensity graph for the PS:PMMA blend and is shown in Figure 1.24. The plot shared the same features as the F8BT/PBT data, in that there was a smooth appearance of a broad scattering peak as in the case of bulk phase-separation. As previously seen unlike bulk phase-separation, there was a superimposed rise in scattering intensity, a periodic increase and decrease in overall intensity (with a period matching specular reflectivity) and the scattering vector q_{max} moved to a higher value as phase separation proceeded.

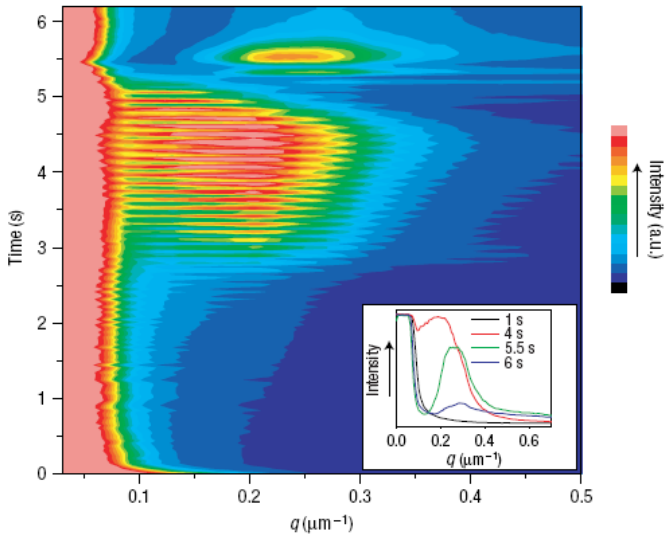

Figure 1.24. Contour plot showing the radially averaged light-scattering intensity out of the specular direction for PS:PMMA (1:1) blend film. Taken from reference (57).

The appearance of scattering with a well-defined peak scattering vector is indicative of the development of lateral structure within or at the surface of the film, in Figure 1.24 the length scale characterising the lateral structure is around 30 μm. Two mechanisms where proposed to account for the production of such a peak. The first is the bulk mechanism of spinodal decomposition, where composition fluctuations are amplified by a process that selects the fastest growing length scale (Section 1.2.2). The second was that the initial phase-separation within the film occurs perpendicular to the plane of the film, resulting in a lateral interface between layers of different composition.(67) This interface then becomes unstable leading to a wavelength-selective amplification of a capillary wave in a process analogous to spinodal de-wetting.(68)

As in previous studies the periodic modulation in intensity observed in these experiments was attributed due to the thin-film geometry. As the film continues to thin, interference effects cause a periodic variation with film

thickness of the electric-field intensity at the position of the roughening interfaces from which scattering arises.

A more detailed analysis was performed on the specular reflectivity data, which offered support in favour of the second suggestion for the mechanism producing the well-defined scattering peak observed in Figure 1.24. The fringe visibility, shown in Figure 1.25 was calculated as $(R_{max} - R_{min}) / (R_{max} + R_{min})$. For the pure PMMA film there was little variation throughout the process, only a slow decrease in fringe visibility, followed by a sharper increase in visibility, which was attributed to a coarsening of the film. For the PS:PMMA film at early stages of the spinning process, the blend showed a systematic modulation of fringe visibility with time that was not observed with the pure polymer. This was interpreted to indicate that the film split into two layers, one rich in PS and the other rich in PMMA. Later in the spinning process, at a time corresponding to the onset of off-specular scattering (phase separation), the fringe visibility decreased whereas the average reflectivity remained constant, which was accounted for by assuming the average roughness of the free surface increases, leading to a reduction in the reflectance of that interface.

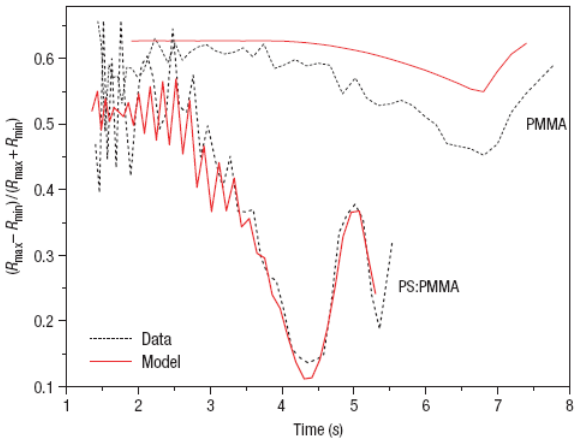

Figure 1.25. Fringe visibility for PMMA and PS:PMMA (1:1) with corresponding models. Taken from reference (57).

These effects were modelled (semi-quantitatively) based on the assumption that the effect of small-length-scale roughness on the reflectance of the top surface may be accounted for by a Debye-Waller-like factor as derived for x-rays.(69) Analysis indicated that, during the initial phase of the instability, the root mean squared (RMS) roughness increased to a value of 120 nm, at a time when the total film thickness was 3.44 μm. The end of this phase was marked by an abrupt shift in the position of the peak in off-specular scattering intensity, corresponding to a decrease in the characteristic length scale from a value of 53 to 25 μm.

The reflectivity profile during film thinning was modelled using a classical expression for the reflectivity of a dielectric film on a substrate, for both pure PMMA and a PS:PMMA blend. Solvent concentration was assumed to be uniform throughout the film, and interfacial roughness was included. The model fitted the obtained data for pure PMMA well, except that it showed lower visibility than the experimental data, as the model did not take into account concentration gradients within the film. The model for the PS:PMMA blend, did not fit the experimental data as well. However, the model did capture the most striking features of the data (i.e. the periodic modulation of fringe intensity). The conclusions from this study are summarised in Figure 1.26. Initially wetting layers form at the air-film and film-substrate interfaces (i)-(iii). When the thickness decreases to a critical value, the interface between these wetting layers becomes unstable and thermally excited capillary waves are amplified with a mechanism to select a length scale, resulting in the observed off-specular scattering (iv) and a final phase separated structure.

Heriot and Jones speculated that an instability at the polymer-polymer interface arose because of a solvent-concentration gradient through the film. Due

to the solvent at the film surface evaporating at a faster rate than the solvent in the bulk can diffuse through the film, resulting in a significantly lower solvent concentration at the surface compared to that of the substrate.(68) The interfacial tension at a polymer-polymer interface is a strong function of the solvent concentration,(70) so if an interface is in the plane of the film, it is very probable that it would be subject to a Marangoni-like instability.

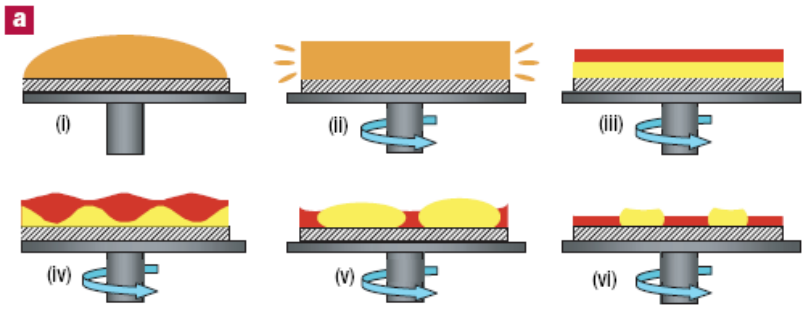

Figure 1.26. A schematic model describing the film formation during the spin-coating process, and the final film morphology. Taken from reference (57).

As the film thinned further the instability is expected to grow (independent of its origin), leading to an increase in the off-specular scattered intensity and an increase in the roughness of the top surface of the film. At some point, the amplitude of the instability becomes such that the liquid-liquid interface meets the surface. At this point there is a rapid movement of the contact lines to yield the laterally phase separated structure shown in step (v) of Figure 1.26. This stage is marked by a decrease in surface roughness and an abrupt change in the peak in the scattering pattern. Simultaneously, or subsequently, as the total polymer concentration is increasing and the equilibrium phase boundaries change, phase separation may be initiated in one or both phase, leading to a hierarchical, secondary phase separation step.(57)

In order to further explore the role of evaporation on the structural development of a spin-coated PS:PMMA blend an environmental cell was implemented into the laser scattering set-up by Mokarian-Tabari *et al.* (shown in Figure 1.27a).(47) This approach controlled evaporation rates where obtained through controlling the solvent atmosphere, differing from Birnie's earlier experiments, where the evaporation rate was varied through changing the solvent. Experimental curves for the evolution of film thickness for a variety of values of the nominal applied vapour pressure are shown in Figure 1.27b and show two distinct stages of film thinning behaviour. Firstly, early on the spin-coating process hydrodynamic thinning in which the solvent does not strongly effect the thinning rate. Secondly, an evaporation dominated stage in which the rate of thinning could be systematically changed through controlling the solvent vapour pressure. The evaporation rate was extracted from the thickness-time profiles using Meyerhofer's model. As expected increasing the nominal vapour pressure lead to a decrease in the evaporation rate.

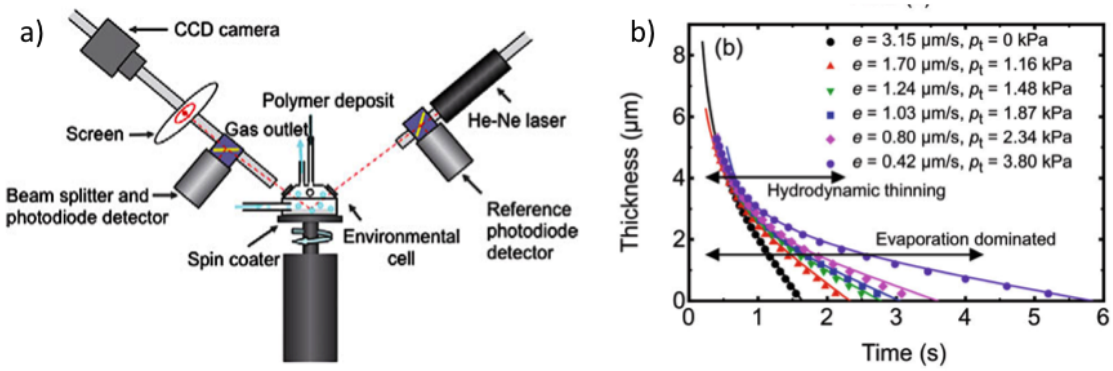

Figure 1.27. a) Schematic diagram showing the integrated light scattering set-up with an integrated spin coater and environmental cell; b) Thickness-time profiles for toluene at different evaporation rates. The evaporation rate, *e*, is controlled by changing P_t, the nominal toluene vapour pressure inside the cell. The points and lines are data and fits, respectively. Taken from reference (47).

The structure evolution for films spun from mixtures of PS and PMMA at controlled evaporation rates was then studied using specular reflectivity and off-specular scattering. Figure 1.28 shows the off-specular scattering data and optical micrographs of films, taken at the centre and near the edge of the sample for PS:PMMA blends spun at different evaporation rates.

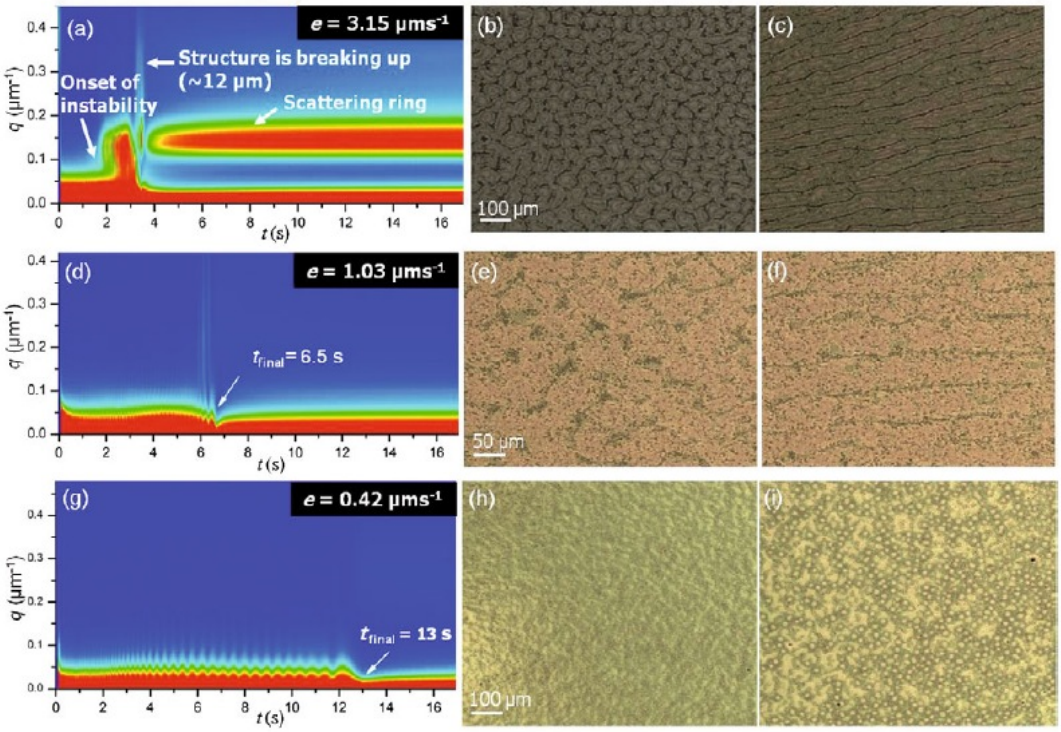

Figure 1.28: a-c) radially integrated off-specular scattering profiles as a function of time for PS:PMMA blends spin-coated at evaporation rates of; 3.15, 1.03 and 0.42 μm s^{-1}. Corresponding micrographs of the resultant morphology at the centre and off centre are shown to the right [b-c), e-f) and h-i)] of the off-specular data. Taken from reference (47).

Figure 1.28b-c show the typical spin-cast film morphologies for a film spun in an ambient atmosphere. At the centre of rotation (*b*) there are isotropic islands of PMMA in a cellular pattern, whereas off centre (*c*) the structure is radially orientated striations. The isotropic island and stirations have a similar length scale (~50 μm), which is an indication that hydrodynamic forces break the symmetry of

the instability when the shear forces are sufficiently large, without affecting the dynamics of the phase separation lengthscale. Figure 1.28a is a intensity plot showing the radially averaged off-specular light scattering intensity for the blend film spun cast in an ambient environment, at the greatest evaporation rate studied (e = 3.15 μm s^{-1}). The *q(t)* profile provides information on structure evolution during film formation. The profile shows three different regions. First, a smooth and broad scattering peak shifts towards the largest scattering vector with time, indicative of the onset of instability in the film. This was then followed by the break up of that structure and the formation of a pattern ~12 μm. Finally a fixed pattern with a length scales of ~ 50 μm forms.

Figure 1.28d–f, show data at a decreased evaporation rate (e = 1.03 μm s^{-1}), which has a different scattering pattern and final structure to that observed at a higher evaporation rate. The *q(t)* profile (Figure 1.28d) shows no dominant q, nor scattering ring and takes longer to develop a fixed structure (6.5s instead of 3.5 s). Figure 1.28e–f show the absence of a strong cellular pattern in the centre and that striations start to disappear. Exploiting slower evaporation rates, showed the above trend continued and at one extreme e = 0.42 μm s^{-1} there was no lateral phase separation. As shown in Figure 1.28g, the *q(t)* profile does not reveal any dominant *q*, indicative of a lack of any specific length scale in the film. Evaporation in this film was very slow taking 13 s for the toluene to fully evaporate. The conclusions drawn were that at a low evaporation rate, the concentration gradient in the film was not large enough to trigger a Marangoni instability. The interface oscillates between rough and smooth but the magnitude of the instability is never large enough to break up the film, resulting in stratification. Selective washing was performed on the film formed at the slowest evaporation rate, which indicated a

PMMA layer at the substrate with a PS layer on top. These layers where quantitatively analysed using ion scattering techniques of forward recoil spectrometry (FReS) and nuclear reaction analysis (NRA), which showed clear stratification of the film, with segregation of PS to the air-film interface and PMMA towards the silicon-film interface

The conclusions from this study where that at high evaporation rates (e = 3.5 μm s^{-1}), the film was unstable during evaporation, resulting in lateral phase separation. For evaporation rates between 1.5 and 1.8 μm s^{-1} striations in the film may develop. Decreasing the evaporation rate below e = 1.6 μm s^{-1} suppresses the instability, allowing vertical phase separation to proceed. For these low rates of evaporation, the solvent remained in the film long enough to allow the polymer surface energies to dominate and control the final morphology. However, for fast evaporation in which diffusion cannot re-equilibrate the concentration through the film, large solvent concentration gradients exist near the surface of the film. Such gradients destabilise the polymer flow causing the breakup of the (transient) wetting layer in a Marangoni-type instability, leading to lateral phase separation.

1.4.3 Video observation studies

In situ studies utilising scattering based methods provide data in reciprocal-space, where data is in the form of the Fourier transform of an image. Therefore information on the morphological development is inferred from the changes in the observed length-scale of the scattering sample.

In 2009 Birnie developed a technique for mapping the evolution of thickness profiles during spin-coating, through combining colour video observations with laser interferometry.(71) Building upon previous work, where

colour video images where used to determine the final film thicknesses of transparent coatings on silicon.[72] As with previous specular reflectivity based techniques, this colour mapping technique utilises the intereference effects causing a thinning film to exhibit distinct colours as it thins. Laser interferometry was performed at the centre of rotation to determine fluid thickness as in previous experiments,(60, 62, 63) to provide a calibration for the colour video observations. Laser interferometry was performed at normal incidence and video observation was performed away from the normal incidence. The video camera captures a colour image by detecting the varying intensities of the reflected incident red, green and blue (RGB) light at a particular position on the wafer. By linking the evolution of colour intensity at the centre, to the corresponding fluid thickness measured by interferometry, Birnie was able to extend the intensity analysis to nearby positions on the wafer and by comparison determine the fluid thickness profile at a particular time.

N-propyl alcohol was used to test this experimental study, as it had a sufficiently low volatility to allow 60 distinct RGB intensity variations to be detected, which where used to generate colour matching calibration points. A typical fluid height vs time plot was generated as previously described for laser reflectivity experiments. Then the fluid thickness at the centre of rotation was matched to the colour of the fluid at an instant in time, thus a thickness value was assigned to a particular colour. From the interferometrically determined thickness vs. time dependence, each (R*, B*) value was assigned a particular thickness, where R* and B* are the scaled fractional red and blue colour balance values of a given pixel.

Thinning was first tracked qualitatively by following the progression of the yellowish zone that starts in the centre of Figure 1.29a. This coloured zone spreads radially, resulting in the appearance of a colourful, growing ring as shown by the expanding yellow ring in Figure 1.29b-c. The yellow colour was matched to a corresponding film thickness from laser interferometry and they assumed that the ensuing yellow rings where indicative of the fluid reaching the same thickness at radial positions further from the wafer centre. The process was conducted for every observable colour displayed at the film centre, in order to dynamically map the film thickness across the entire wafer throughout the bulk of the latter stage of spin-coating. The resultant fluid thickness profile as a function of radius for four different time intervals is shown in Figure 1.30. As expected from the colour variations visible in Figure 1.29, there is a substantial increase in fluid thickness as the radius increases. At each time step there is an incremental loss of solution due to evaporation and hydrodynamic flow.

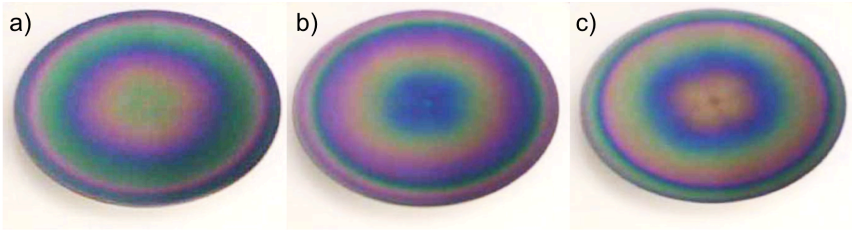

Figure 1.29. Frames captured from a video sequence taken of n-propanol spinning on a 50 mm diameter silicon wafer rotating at 2000 RPM. The three images occur sequentially separated by 66.7 ms (every other frame from this sequence), a),b), and c) correspond to 3.87, 3.93, and 4.00 s into the spin-coating process, respectively. Taken and modified from reference (71).

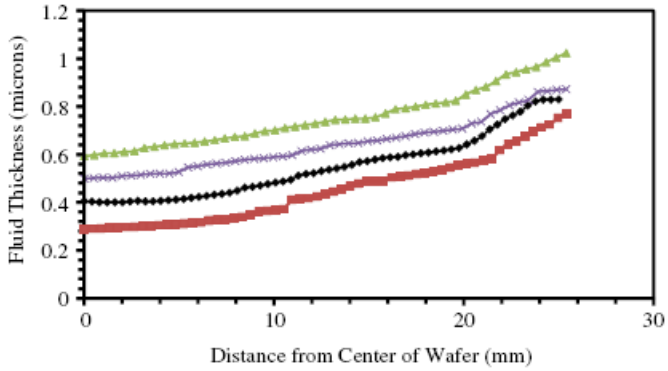

Figure 1.30. Thickness profile for fluid for four different frames 3.87, 3.93, 4.00, and 4.07 s into the spin-coating (from top to bottom). Taken from reference (71).

In 2011 Ebbens & Howse developed a direct imaging approach capable of obtaining micrometer-scale lateral and nanometer vertical precision metrology during the spin coating of a phase separating polymer blend, providing lateral in-plane information in real-space with height information inferred from interference information.(73)

The method employed synchronised stroboscopic LED illumination with a high sensitivity electron-multiplying charge-coupled device camera (EMCCD) connected to an episcopic optical microscope to optically observe structure evolution of polymer blends during spin coating. The sample was irradiated with a filtered high intensity near monochromatic green LED ($\Delta\lambda \sim 10$ nm), which allowed interference reconstruction of three-dimensional topographies of the spin-coated film as it dries and phase separates with nanometre precision.(73) The experimental set-up, is somewhat similar to Graves', in that a light source was synchronously triggered with a charge coupled device and a series of stroboscopically frozen images where recorded. Images were recorded once every full revolution, allowing for a movie of the evolution of phase separation at the same location to be recorded [This technique is discussed in further detail in

Chapter 2]. An illumination source with a narrow bandwidth was used so that interferometric height reconstruction could be performed, as such contrast in the stroboscopic images reflects instantaneous height differences at the sample surface and is as a consequence of constructive/destructive interference.

High molecular-weight polystyrene (PS) and polyisoprene (PI) blends in *ortho*-xylene where studied in order to generate better understanding of the processes involved in the fundamental phase separating behaviour of polymer blends. The high molecular-weights of the polymers and relatively low vapour pressure of *ortho*-xylene ensured that lengthscales were optically visible and that the phase separation and drying where relatively slow.

Figure 1.31 shows extracts from a movie, which directly observes, in real-space, the evolution of microstructure during the spin-coating of a polymer-blend, with resolution and clarity comparable to that obtained from conventional optical microscopy of a static sample. As the height of the film is continuously decreasing due to hydrodynamic flow/solvent evaporation, periodic interference contrast inversions occur according to Bragg's law (as seen in the final two frames of Figure 1.31). Early on in the spinning process (the first frame, t = 8 s) the image shows no contrast, as the surface is flat and uniform. After approximately 12 s onwards, weak large-scale fluctuations roughly 100 μm in length become observable, which then become increasingly dominated by shorter scale fluctuations of approximately 20 μm, which appear to have a fixed position until the final dry film at 17.2 s reflecting the expected stages of the spin-coating process. The radially averaged Fourier transformed data shows the evolution of the two lengthscales during the spin coating process. The longer length scale decreased in length as the film dried, converging with the length scale

corresponding to the obvious phase separated domain structure. The images and FFT analysis in Figure 1.31 indicated the final phase-separated structure appeared very early and evolved very little once the liquid-liquid transition had occurred, despite the fact solvent evaporation occurred for a further 5 s. It was believed that the larger length scale structure was likely to be caused by Marangoni type instabilities, due to solvent evaporation. However, in the case of the PS/PI blend, Marangoni type instabilities had little influence on the final structure. This technique provides a new method to explore the extent to which phase separation and Marangoni phenomena inter-relate to form the resultant final morphology in a range of polymer systems.

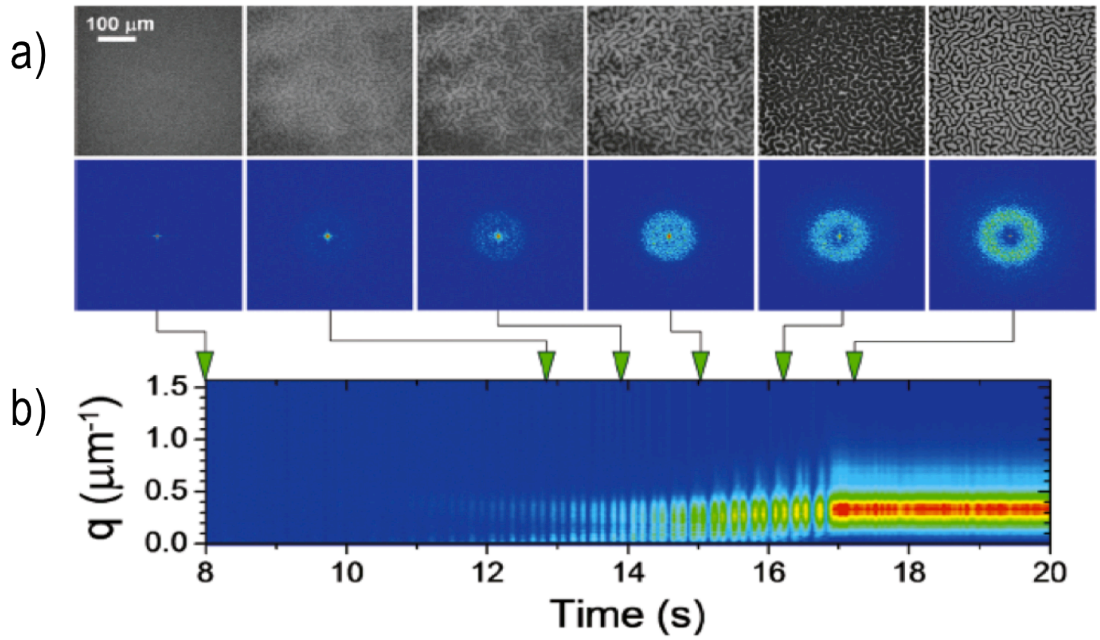

Figure 1.31. a) a series of unprocessed stroboscopic optical reflectance images recorded during spin coating of a 1:1 blend of PS:PI (2% wt at 1500 rpm) from *ortho*-xylene are shown. The images were illuminated with narrow-bandwidth green light at the indicated times during the spin-coating process b) Corresponding background-corrected 2D Fourier transforms are shown underneath each frame, with the radial integral of the Fourier transform for a section of the movie above. Taken from reference (73).

Analysis of the intensity variation at each image pixel as function of time allowed the corresponding drying rate of the film to be determined and mapped across the entire field of view, through using methodology analogous to that of spatially averaged specular laser methods previously mentioned. This required the assumption of flat uniform film morphology at a sufficiently early stage of the film formation, to be used as a starting point where all oscillations of the specular reflectivity intensity would be in-phase.

The drying curves extracted from this analysis revealed a consistent difference in the drying rate between optically “bright” and “dark” domains as seen in the dry film under monochromatic light. Resulting in the predicted height difference between these locations, such that optically “dark” regions dried at a slower rate, resulting in a higher film height than the “bright” regions. Applying the same analysis to the homopolymer samples revealed that the pure PS homo-polymer dried completely within 12 s of spin coating, whereas, the pure PI homo-polymer took 22 s to dry. The blend dry film end point lay at the midpoint of these two values. The drying rate over the final 6 s was faster for PS than PI, and ellipsometry indicated that the final PS film thickness was less than that for PI. Suggesting the faster drying “bright” domains where PS rich and the slower drying “dark” domains where PI rich. This assignment was confirmed via selective washing, and verified that such drying rate curve analysis can facilitate material identification.

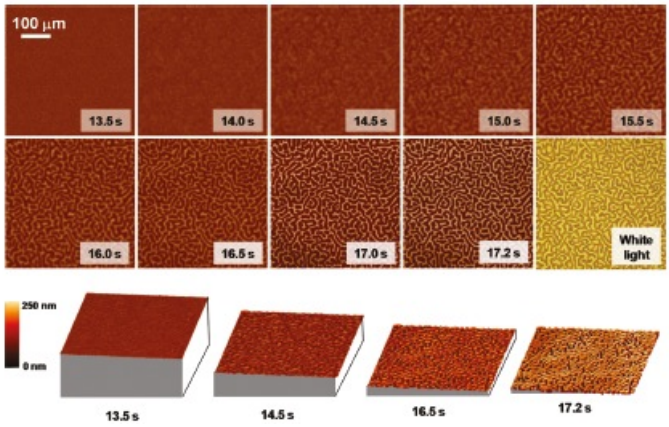

Figure 1.32. (Top) 2D relative height reconstructions during spin coating a PS:PI blend at 1500 rpm obtained from pixel by pixel drying curve arrays generated from fringe counting the stroboscopic optical images. (Bottom) 3D surface morphology reconstructions. Taken from reference (73).

Through application to every pixel value the method was extended to reconstruct by interpolation the absolute quantitative sample height across the whole field of view at all stages during the drying process, as shown in Figure 1.32.

The validity of the assumption of uniform film morphology with a low roughness as the start point for the analysis was tested by comparing the final reconstructed morphology with AFM metrology carried out at the same region of the final sample surface. Cross-section analysis revealed a quantitative agreement between the reconstructed and "real" AFM data in the z-direction within 10% accuracy. Figure 1.33 schematically illustrates how the bi-continuous phase-separated morphology appeared well before the end point of the drying process and that no significant lateral translation occurred after this point. Apparent features in the final surface topography where initially visible early on in the spinning process where the film thickness was greater than 2 µm (~10x greater than final thickness). FFT analysis of the raw optical images (Figure 1.31),

indicated features at this length scale where first visible after 11 s after spin coating begins (6 s before the sample dried). The early surface structure observed supported the theoretical prediction that that phase separation originated at the surface first and that the original structure forms a motif to direct the subsequent phase separation of solvent richer underlying regions.(74)

The morphological reconstructions confirmed that phase separation in the PS:PI system followed a straightforward spinodal decomposition process, with little influence by Marangoni instabilities. However, fine details of the phase-separated morphology develop over fractions of seconds of the drying process and appear fixed once formed.

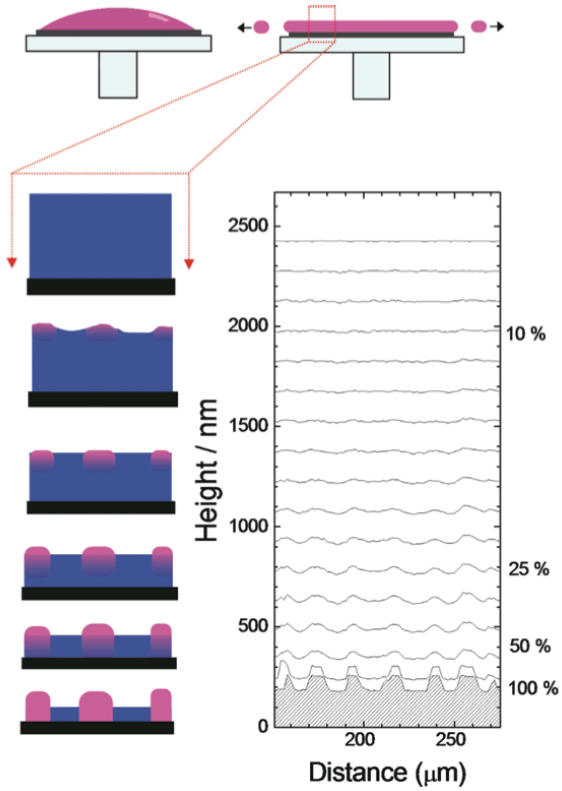

Figure 1.33. (Left) Schematic of cross section during the phase separation process. (Right) Quantitative reconstructed surface topography at 0.25 s intervals (start time 13 s). Estimated polymer content labeled on right-hand axis. Taken from reference (73).

Recently, Chou *et al.* employed a combination of video microscopy, time resolved spectroscopic reflectometry, with grazing incidence small and wide angle x-ray scattering (GISAXS and GIWAXS, respectively) to study the blend of poly-(3-hexylthiophene) (P3HT) and [6,6]-phenyl C61-butyric acid methyl ester (PCBM), which is the most widely studied system for bulk heterojunction (BHJ) organic solar cells.(75) Video microscopy was used to observe solution spreading and ejection across the solution and spectral reflectometry provided information regarding film thickness evolution. P3HT lamellar crystallization was monitored via wide angle scattering, whilst phase separation of PCBM from P3HT was detected via small angle scattering.

The experimental set-up and data for a P3HT:PCBM (1.7:1) blend are shown in Figure 1.34. The video microscopy images (top left) reveals a rapid spreading and loss of solution via ejection, which leads to the formation of a uniform liquid layer at ~0.5 s. The thickness evolution of this layer (top right) was monitored via reflectivity measurements, which shows that within 0.5 s the fluid rapidly thins from ~1 mm to ~12 μm. As in earlier studies initial thinning was predominately attributed to hydrodynamic forces and later on in the process (3.6 s, ~2 μm) thinning was driven by solvent evaporation.

The *in situ* GIWAXS measurements (bottom, first row) show the crystallization of P3HT lamellae, represented by the formation of the (100) Bragg sheet, whilst the GISAXS (bottom, second row) measurements show the agglomeration of PCBM. Analysis of the (100) peak in the GIWAXS data (yellow ellipse) and the low q region in the GIWAXS data (green box) indicated that crystallisation and phase separation occur simultaneously, early on in the spin-coating process (<1 s). The kinetics of the process were found to be highly

dependent upon the composition of the blend. P3HT crystallisation was found to be slowed with increasing PCBM content and was completely inhibited above 50 wt% PCBM.

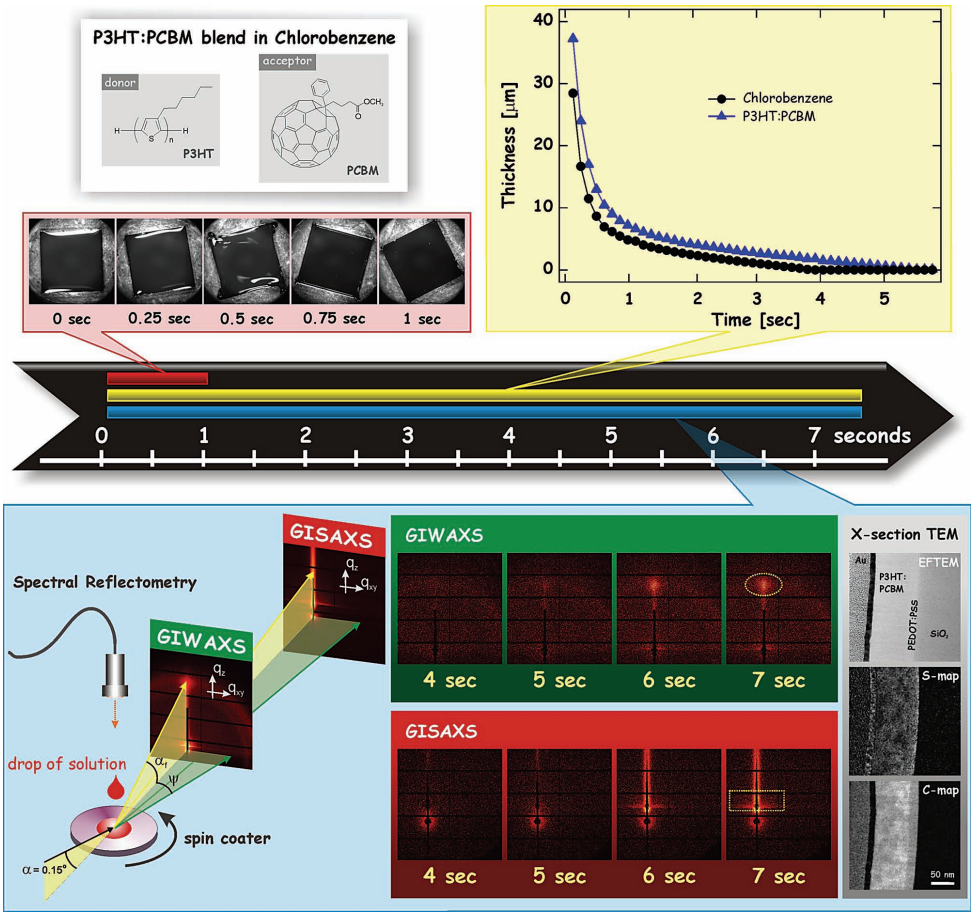

Figure 1.34. Visual timeline of the spin-coating process of P3HT:PCBM blend (62.5 wt%:37.5 wt%) recorded via video microscopy (top left), spectroscopic reflectometry (thickness profile top right) and grazing incidence small and wide angle scattering (bottom). Taken from reference (75).

1.5 Summary

In situ studies of spin coating have been vital in developing knowledge of the many different parameters that determine the final film thickness and the rich morphologies generated. The early studies of Horowitz, and later Birnie, confirmed

the validity of the EBP model in the early stages of the process and Meyerhofer's extension of the EBP model to include evaporation rate and showed that a two stage process adequately described the spin coating of simple solvents and binary solvent mixtures. The work conducted by Heriot *et al.* combined reflectivity and light scattering techniques, in order to investigate more complex polymer blend systems, which cast insight into the processes of phase separation. The results indicated that in some cases phase separation in thin films may not occur via the same mechanisms as in the bulk case. The later work of Birnie, Ebbens & Howse and recently Chou *et al* have utilised novel experimental approaches to investigate further intricacies of the processes that occur during the spin-coating of polymer blends. Such studies have only become possible due to the development of highly sensitive detector technology, which are able to detect low intensity images/diffraction patterns.

1.6 References

1. Friend RH, Burroughes JH, Bradley DDC, inventors; Cambridge Research and Innovation Ltd., UK; Cambridge Capital Management Ltd.; Lynxvale Ltd. . assignee. Electroluminescent devices and their manufacture patent WO9013148A1. 1990.
2. Jones RAL. Soft condensed matter: Oxford University Press; 2002.
3. Geoghegan M, Hadziioannou G. Polymer Electronics: Oxford University Press; 2013.
4. Doi M. Introduction to polymer physics: Oxford University Press; 1996.
5. Tanaka H. Viscoelastic phase separation. Journal of Physics: Condensed Matter. 2000;12(15):R207.
6. Hashimoto T, Sasaki K, Kawai H. Time-Resolved Light-Scattering Studies on the Kinetics of Phase-Separation and Phase Dissolution of Polymer Blends .2. Phase-Separation of Ternary Mixtures of Polymer-a, Polymer-B, and Solvent. Macromolecules. 1984;17(12):2812-8.
7. Kim J-S, Ho PKH, Murphy CE, Friend RH. Phase Separation in Polyfluorene-Based Conjugated Polymer Blends: Lateral and Vertical Analysis of Blend Spin-Cast Thin Films. Macromolecules. 2004;37(8):2861-71.
8. Cahn JW, Hilliard JE. Free energy of a nonuniform system. I. Interfacial free energy. The Journal of Chemical Physics. 1958;28:258.

9. Cahn JW. Phase Separation by Spinodal Decomposition in Isotropic Systems. Journal of Chemical Physics. 1965;42(1):93-&.
10. Morral JE, Cahn JW. Spinodal Decomposition in Ternary Systems. Acta Metallurgica. 1971;19(10):1037-&.
11. De Gennes P. Dynamics of fluctuations and spinodal decomposition in polymer blends. The Journal of Chemical Physics. 1980;72:4756.
12. Pincus P. Dynamics of fluctuations and spinodal decomposition in polymer blends. II. The Journal of Chemical Physics. 1981;75:1996.
13. Binder K. Collective Diffusion, Nucleation, and Spinodal Decomposition in Polymer Mixtures. Journal of Chemical Physics. 1983;79(12):6387-409.
14. Sanchez IC. Bulk and Interface Thermodynamics of Polymer Alloys. Annual Review of Materials Science. 1983;13(1):387-412.
15. Voorhees PW. Ostwald ripening of two-phase mixtures. Annual Review of Materials Science. 1992;22(1):197-215.
16. Schichtel TE, Binder K. Kinetics of Phase-Separation in Polydisperse Polymer Mixtures. Macromolecules. 1987;20(7):1671-81.
17. Huang C, Delacruz MO. The Early Stages of the Phase-Separation Dynamics in Polydisperse Polymer Blends. Macromolecules. 1994;27(15):4231-41.
18. Clarke N. Early stages of phase separation from polydisperse polymer mixtures. The European Physical Journal E. 2001;4(3):327-36.
19. Mumby SJ, Sher P, van Ruiten J. Liquid—liquid phase separation in blends of polydisperse linear and branched polyethylenes. Polymer. 1995;36(15):2921-7.
20. Atkins P, De Paula J. Atkins' physical chemistry: Oxford University Press; 2010.
21. Brabec CJ, Heeney M, McCulloch I, Nelson J. Influence of blend microstructure on bulk heterojunction organic photovoltaic performance. Chemical Society Reviews. 2011;40(3):1185-99.
22. Muthukumar M. Commentary on theories of polymer crystallization. European Physical Journal E. 2000;3(2):199-202.
23. Gránásy L, Pusztai T, Tegze G, Warren JA, Douglas JF. Growth and form of spherulites. Physical Review E. 2005;72(1):011605.
24. Bénard H. Étude expérimentale des courants de convection dans une nappe liquide.—Régime permanent: tourbillons cellulaires. J Phys Theor Appl. 1900;9(1):513-24.
25. Maroto J, Pérez-Munuzuri V, Romero-Cano M. Introductory analysis of Bénard–Marangoni convection. European journal of physics. 2007;28(2):311.
26. Rayleigh L. LIX. On convection currents in a horizontal layer of fluid, when the higher temperature is on the under side. The London, Edinburgh, and Dublin Philosophical Magazine and Journal of Science. 1916;32(192):529-46.
27. Ball P. The self-made tapestry: pattern formation in nature: Oxford Univ. Press, Oxford.
28. Mihi A, Ocana M, Miguez H. Oriented colloidal-crystal thin films by spin-coating microspheres dispersed in volatile media. Adv Mater (Weinheim, Ger). 2006;18(17):2244-9.
29. Norris DJ, Arlinghaus EG, Meng L, Heiny R, Scriven LE. Opaline photonic crystals: How does self-assembly work? Adv Mater (Weinheim, Ger). 2004;16(16):1393-9.
30. Wijnhoven JEGJ, Vos WL. Preparation of photonic crystals made of air spheres in Titania. Science (Washington, D C). 1998;281(5378):802-4.

31. Yang SM, Kim SH, Lim JM, Yi GR. Synthesis and assembly of structured colloidal particles. Journal of Materials Chemistry. 2008;18(19):2177-90.
32. Velev OD, Kaler EW. Structured porous materials via colloidal crystal templating: From inorganic oxides to metals. Advanced Materials. 2000;12(7):531-4.
33. Xia YN, Gates B, Yin YD, Lu Y. Monodispersed colloidal spheres: Old materials with new applications. Advanced Materials. 2000;12(10):693-713.
34. Pusey PN, Vanmegen W. Phase-Behavior of Concentrated Suspensions of Nearly Hard Colloidal Spheres. Nature. 1986;320(6060):340-2.
35. Denkov N, Velev O, Kralchevsky P, Ivanov I, Yoshimura H, Nagayama K. Two-dimensional crystallization. 1993.
36. Kralchevsky PA, Denkov ND. Capillary forces and structuring in layers of colloid particles. Current Opinion in Colloid & Interface Science. 2001;6(4):383-401.
37. Ohara PC, Gelbart WM. Interplay between hole instability and nanoparticle array formation in ultrathin liquid films. Langmuir. 1998;14(12):3418-24.
38. Cong H, Cao W. Array patterns of binary colloidal crystals. J Phys Chem B. 2005;109(5):1695-8.
39. Brabec CJ, Durrant JR. Solution-processed organic solar cells. Mrs Bulletin. 2008;33(7):670-5.
40. Armstrong NR, Wang W, Alloway DM, Placencia D, Ratcliff E, Brumbach M. Organic/Organic' Heterojunctions: Organic Light Emitting Diodes and Organic Photovoltaic Devices. Macromol Rapid Commun. 2009;30(Copyright (C) 2012 American Chemical Society (ACS). All Rights Reserved.):717-31.
41. Agostinelli T, Ferenczi TAM, Pires E, Foster S, Maurano A, Mueller C, et al. The Role of Alkane Dithiols in Controlling Polymer Crystallization in Small Band Gap Polymer:Fullerene Solar Cells. Journal of Polymer Science Part B-Polymer Physics. 2011;49(10):717-24.
42. Andrew JP, Tao W, David GL. The role of dynamic measurements in correlating structure with optoelectronic properties in polymer,Äâ:,Ääfullerene bulk-heterojunction solar cells. Reports on Progress in Physics. 2013;76(2):022501.
43. Arias AC, Endicott F, Street RA. Surface-induced self-encapsulation of polymer thin-film transistors. Advanced Materials. 2006;18(21):2900-+.
44. Schuettfort T, Watts B, Thomsen L, Lee M, Sirringhaus H, McNeill CR. Microstructure of Polycrystalline PBTTT Films: Domain Mapping and Structure Formation. Acs Nano. 2012;6(2):1849-64.
45. Emslie AG, Bonner FT, Peck LG. FLOW OF A VISCOUS LIQUID ON A ROTATING DISK. Journal of Applied Physics. 1958;29(5):858-62.
46. Meyerhofer D. Characteristics of resist films produced by spinning: AIP; 1978. 3993-7 p.
47. Mokarian-Tabari P, Geoghegan M, Howse JR, Heriot SY, Thompson RL, Jones RAL. Quantitative evaluation of evaporation rate during spin-coating of polymer blend films: Control of film structure through defined-atmosphere solvent-casting. European Physical Journal E. 2010;33(4):283-9.
48. Birnie D, III, Hau S, Kamber D, Kaz D. Effect of ramping-up rate on film thickness for spin-on processing. J Mater Sci: Mater Electron. 2005;16(11-12):715-20.

49. Hall DB, Underhill P, Torkelson JM. Spin coating of thin and ultrathin polymer films. Polymer Engineering & Science. 1998;38(12):2039-45.
50. Toolan DTW, Haq Eu, Dunbar A, Ebbens S, Clarke N, Topham PD, et al. Direct observation of morphological development during the spin-coating of polystyrene-poly(methyl methacrylate) polymer blends. Journal of Polymer Science Part B: Polymer Physics. 2013;51(11):875-81.
51. Walheim S, Boltau M, Steiner U, Krausch G. Phase separation in thin films of strongly incompatible polymer blends. Richards RWPSK, editor1999. 75-99 p.
52. Dalnoki-Veress K, Forrest JA, Stevens JR, Dutcher JR. Phase separation morphology of spin-coated polymer blend thin films. Physica A: Statistical Mechanics and its Applications. 1997;239(1-3):87-94.
53. Dalnoki-Veress K, Forrest JA, Stevens JR, Dutcher JR. Phase separation morphology of thin films of polystyrene/polyisoprene blends. Journal of Polymer Science Part B: Polymer Physics. 1996;34(17):3017-24.
54. Mellbring O, Oiseth SK, Krozer A, Lausmaa J, Hjertberg T. Spin coating and characterization of thin high-density polyethylene films. Macromolecules. 2001;34(21):7496-503.
55. Xue BF, Vaughan B, Poh CH, Burke KB, Thomsen L, Stapleton A, et al. Vertical Stratification and Interfacial Structure in P3HT:PCBM Organic Solar Cells. Journal of Physical Chemistry C. 2010;114(37):15797-805.
56. Dunbar AD, Mokarian-Tabari P, Parnell AJ, Martin SJ, Skoda MW, Jones RA. A solution concentration dependent transition from self-stratification to lateral phase separation in spin-cast PS:d-PMMA thin films. Eur Phys J E Soft Matter. 2010;31(4):369-75.
57. Heriot SY, Jones RAL. An interfacial instability in a transient wetting layer leads to lateral phase separation in thin spin-cast polymer-blend films. Nat Mater. 2005;4(10):782-6.
58. Manske L. Dynamic measurements of film thickness over local topography in spin coating. Appl Phys Lett. 1990;56(23):2348.
59. Peurrung LM, Graves DB. FILM THICKNESS PROFILES OVER TOPOGRAPHY IN SPIN COATING. J Electrochem Soc. 1991;138(7):2115-24.
60. Horowitz F, Yeatman E, Dawnay E, Fardad A. REAL-TIME OPTICAL MONITORING OF SPIN-COATING. Journal De Physique Iii. 1993;3(11):2059-63.
61. Horowitz F, Dawnay EJC, Fardad MA, Green M, Yeatman EM. Towards better control of sol-gel film processing for optical device applications. J Nonlinear Opt Phys Mater. 1997;6(1):1-18.
62. Birnie D. Combined flow and evaporation of fluid on a spinning disk. Phys Fluids. 1997;9(4):870.
63. Dunbar P B, III. Combined flow and evaporation during spin coating of complex solutions. Journal of Non-Crystalline Solids. 1997;218(0):174-8.
64. Jukes PC, Heriot SY, Sharp JS, Jones RAL. Time-Resolved Light Scattering Studies of Phase Separation in Thin Film Semiconducting Polymer Blends during Spin-Coating. Macromolecules. 2005;38(6):2030-2.
65. Corcoran N, Arias AC, Kim JS, MacKenzie JD, Friend RH. Increased efficiency in vertically segregated thin-film conjugated polymer blends for light-emitting diodes. Applied Physics Letters. 2003;82(2):299-301.
66. Budkowski A, Bernasik A, Cyganik P, Raczkowska J, Penc B, Bergues B, et al. Substrate-determined shape of free surface profiles in spin-cast polymer blend films. Macromolecules. 2003;36(11):4060-7.

67. Cahn JW. Phase Separation by Spinodal Decomposition in Isotropic Systems. The Journal of Chemical Physics. 1965;42(1):93-9.
68. de Gennes PG. Instabilities during the evaporation of a film: Non-glassy polymer plus volatile solvent. European Physical Journal E. 2001;6(5):421-4.
69. Nevot L, Croce P. CHARACTERIZATION OF SURFACES BY GRAZING X-RAY REFLECTION - APPLICATION TO STUDY OF POLISHING OF SOME SILICATE-GLASSES. Revue De Physique Appliquee. 1980;15(3):761-79.
70. Broseta D, Leibler L, Kaddour LO, Strazielle C. A THEORETICAL AND EXPERIMENTAL-STUDY OF INTERFACIAL-TENSION OF IMMISCIBLE POLYMER BLENDS IN SOLUTION. Journal of Chemical Physics. 1987;87(12):7248-56.
71. Birnie DP, Haas DE, Hernandez CM. Laser interferometric calibration for real-time video color interpretation of thin fluid layers during spin coating. Optics and Lasers in Engineering. 2010;48(5):533-7.
72. Birnie DP. Optical video interpretation of interference colors from thin transparent films on silicon. Materials Letters. 2004;58(22-23):2795-800.
73. Ebbens S, Hodgkinson R, Parnell AJ, Dunbar A, Martin SJ, Topham PD, et al. In situ imaging and height reconstruction of phase separation processes in polymer blends during spin coating. ACS Nano. 2011;5(6):5124-31.
74. Buxton GA, Clarke N. Ordering polymer blend morphologies via solvent evaporation. Epl. 2007;78(5).
75. Chou KW, Yan B, Li R, Li EQ, Zhao K, Anjum DH, et al. Spin-cast bulk heterojunction solar cells: a dynamical investigation. Adv Mater. 2013;25(13):1923-9.

Chapter 2. Stroboscopic microscopy

Parts of this chapter were published in:

Toolan, D. T. W., Hodgkinson, R. & Howse, J. R. “Stroboscopic microscopy—direct imaging of structure development and phase separation during spin-coating”. *Journal of Polymer Science Part B: Polymer Physics* **52**, 17-25 doi:10.1002/polb.23410 (2013).

2.0 Introduction

As discussed in Chapter 1 the majority of *in situ* spin-coating studies have been based upon laser interferometry and scattering, providing information regarding film thinning behaviour and morphological development, respectively. However, a fundamental drawback of techniques based upon scattering is that results are based in reciprocal space, and as such, information regarding morphological development must be inferred from changes in the observed scattering length scale, which opens the potential for ambiguity in how data is interpreted. In this chapter I will explain how the technique of stroboscopic microscopy may be utilised to obtain information (in *real-space*) regarding topographical, compositional and crystalline development during spin-coating.

The stroboscopic microscopy technique allows information regarding the processes taking place during spin-coating to be obtained in "real-space", eliminating the need for behaviour to be inferred from changes in an observed reciprocal lengthscale obtained through scattering. Microscopy images are collected at the centre of rotation, once per complete revolution of the rapidly rotating sample by applying a short light pulse (~ 50 μs), which allows a static image to be obtained [a] despite the high rotation rate.

The technique utilises a standard reflection microscope, with a DC motor mounted directly underneath the microscope objective, a high-powered LED and

[a] When the sample is rotating at 1500 rpm upon illuminated with a 50 μs light pulse, there will be 0.785 μm of movement at a distance of 100 μm from the centre of rotation.

high sensitivity EMCCD camera that are both electronically synchronised with the motor's rotation. This setup, along with the signal processing flow structure that synchronises the motor, LED and camera is represented in Figure 2.1.

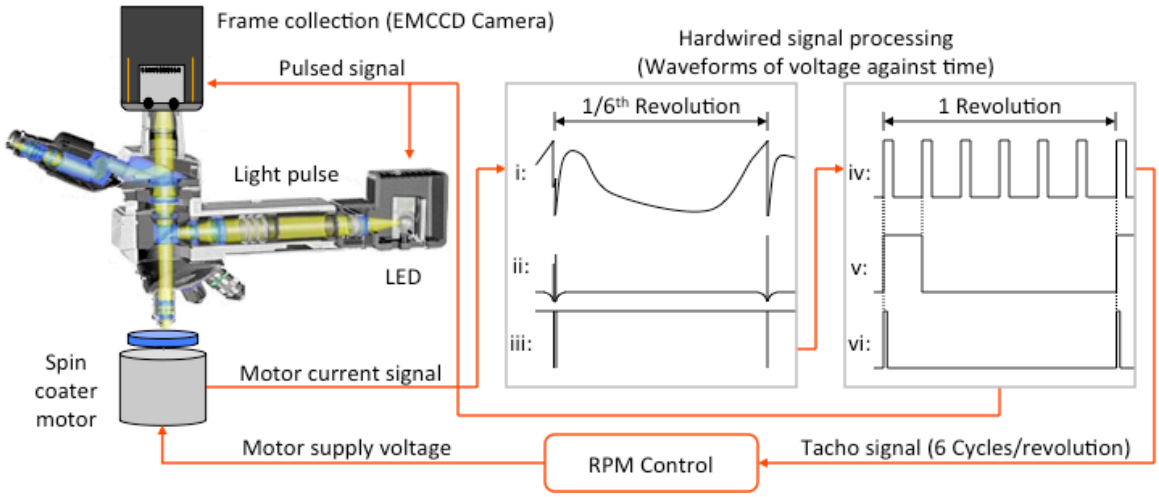

Figure 2.1. From right to left) Schematic of the stroboscopic microscope set-up, showing the signal processing flow structure i-vi, where i) shows oscillations in the motor current, v) is the pulse used to trigger the LED and frame collection and vi) is used as a tachometer to accurately control the rotation rate.

Synchronisation between the spin-coater, LED and camera is achieved by monitoring periodic oscillations in the motor current that arises due to the commutator action. A current waveform is measured through measuring the voltage drop across a resistor (Figure 2.1 i). A waveform of 6 cycles per revolution is typical of motors used to date. The voltage waveform displays sharp dips at a key points per cycle as the motor brushes pass between the commutators. A hardwired inverting differentiator (Figure 2.1 ii) and inverting threshold comparator detect these sharp dips, producing a pulse train (Figure 2.1 iii). Spurious peaks are removed by using these pulses to trigger a fixed-duration pulse generator. The resulting signal (Figure 2.1 iv) is used as a tachometer and fed into

a LabView programme to measure the rotation rate. Motor rotation is controlled via LabView, through a feedback-loop that assesses the desired rotation rate with the rotation rate obtained from the tachometer pulse train, varying the motors supply voltage accordingly and stabilising the motors rotation rate. The cleaned pulse train (Figure 2.1 iv) is divided down via a decade counter (Figure 2.1 v) and square-wave pulses of a predefined length (dictated by the desired illumination pulse time) are generated from it (Figure 2.1 vi) and subsequently used to drive the illumination LED and trigger the camera. This approach allows the use of any DC motor to rotate the substrate and synchronise both illumination and detection. The LED and camera are typically pulsed for 50 μs, depending upon experimental conditions (rotation rate, objective employed); such an illumination time is sufficient to capture a static image at the same point once per rotation. By selecting appropriate LEDs and optical filters the technique can be used to provide information regarding topographical development, compositional development and crystallisation. These modes of operation, along with representative data for each, are shown below in Table 2.1 and will be discussed in sections 2.1 to 2.3.

A typical experimental run involves placing the substrate on top of the spin-coater chuck, focusing the microscope on "imperfections" on the substrate surface and then depositing a solution onto the substrate. The microscope objectives used in this work have depth of fields between 1.13 and 2.76 μm. In many cases the self-assembled structures formed during the spin-coating of a polymer blends are out of focus, due to the combination of a small depth of field and that focusing is performed before the any structure has formed.

2.1 Topographical mode of operation

Thin polymer films often exhibit vibrant colours, due to interference effects that arise due to constructive/destructive interference occurring between the air/film and film/substrate interfaces. Such interference effects occur due to Bragg's law of diffraction:

$$m\lambda = 2nd\ sin\theta \qquad (2.1)$$

where m is an integer value, λ is the wavelength of the incident light, n is the refractive index, d is the film thickness and θ is the angle from the normal incidence.

Table 2.1. Optostrobometer modes of operation and representative data.

Mode of operation	LED	Filter	Typical data
Topography	Near monochromatic red/green	Band pass filter ~20 nm, centred on LED λ_{max}	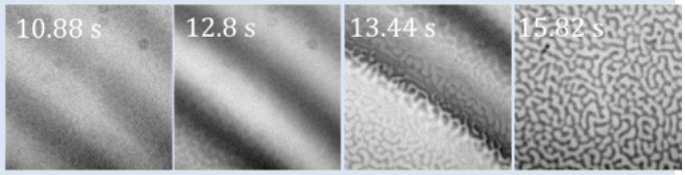
Composition	UV-blue	Beam cube comprising of appropriate filters for fluorophore to be studied	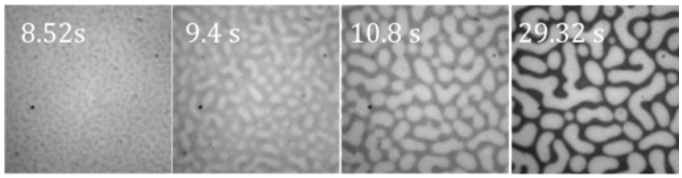
Crystallisation	White (high flux due to effect of polarisers)	Polariser with second analyser polariser	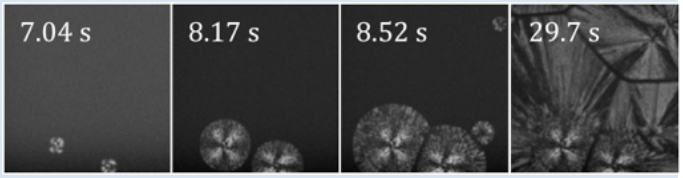

The implications of this equation are that as a polymer film thins during spin-coating, consecutive constructive maxima and destructive minima will be observed every time the film thins by a value of the incident wavelength divided by two times the refractive index.

The topographical mode of operation exploits these oscillations in intensity as a function of thickness in order to obtain information regarding the film height at each individual pixel value on the detector and thus through image processing it is possible to generate three-dimensional topographies from the series of images taken during spin-coating. The sensitivity of this topographical approach relies upon the wavelength distribution or "monochromaticity" of the illumination source. The LEDs employed to generate the required, short lived, stroboscopic pulses typically have a full half width maximum (FHWM) of 20 nm, as shown in Figure 2.2 for the red, red-orange and amber LEDs.

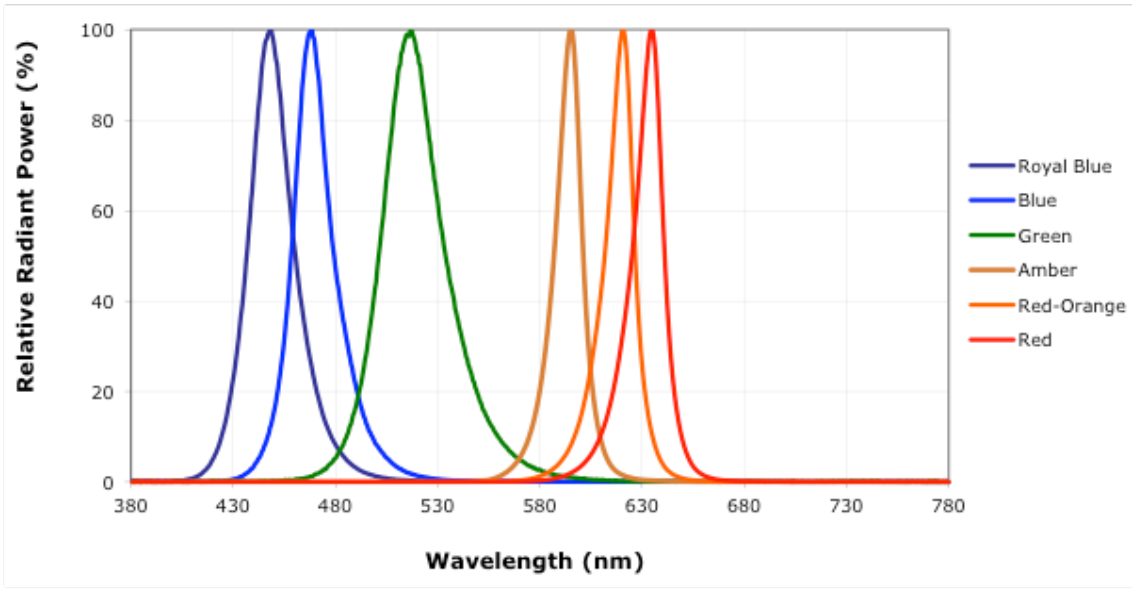

Figure 2.2. Emission spectra of various coloured Cree LEDs. Taken from reference (1).

The effect of this Gaussian wavelength distribution is that when a film thins during spin-coating, the magnitude of the intensity difference between consecutive constructive and destructive interference will increase as the film thins. This enveloping effect is clearly shown in Figure 2.3, which shows the mean pixel intensity over a whole image as a function of time for a spin-coated polymer film.

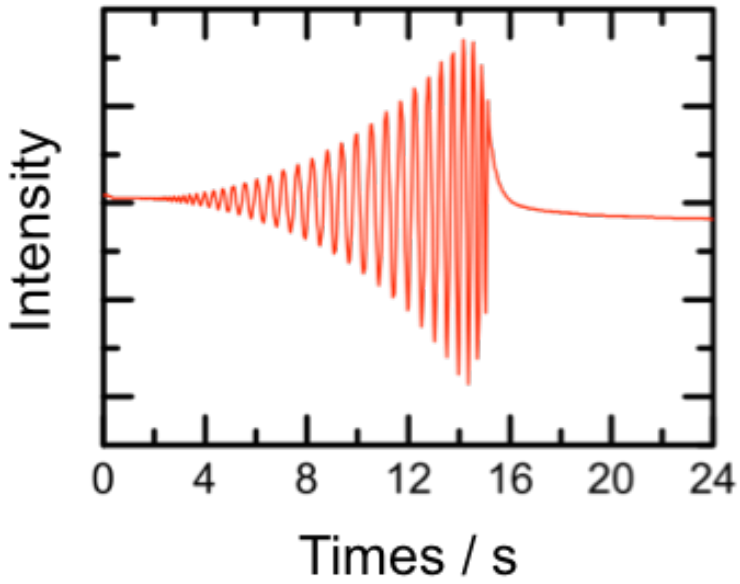

Figure 2.3: Profile showing enveloping of oscillations in spectral reflectivity obtained using an LED with a comparatively large FHWM (20 nm). Taken from a series of *in situ* optical reflectance images recorded for a blend of PS:PMMA spun-cast at 1500 rpm from *ortho*-xylene, illuminated with a red LED λ_{max} = 620 nm, FHWM = 20 nm.

An expression for the relative reflectance of a thin film with a thickness (d) illuminated with a Gaussian wave number spectrum was derived by Koyama *et al*: (2)

$$\frac{I_r(D)}{I_0} = r_{12}^2 + r_{23}^2 + 2r_{12}r_{23}\cos(2n_2k_0d) + e^{\left[-\left(\frac{nd\Delta k}{2}\right)^2\right]} \qquad (2.2)$$

where r_1, r_2 and r_3 are the reflection coefficients of the first medium (air), film and the substrate, respectively, n is the refractive index of the film, k_0 is the central wavenumber of the illumination and Δk is the full half width maximum (FHWM) of the illumination wavenumber spectrum.

As such reflectance is modulated by $\cos(2n_2k_0d)$ as a function of the film thickness d and the amplitude of the modulated component decays with increasing film thickness according to $e^{\left[-\left(\frac{nd\Delta k}{2}\right)^2\right]}$. (2)

Therefore the optimum illumination source, would be completely monochromatic, producing a large difference in the intensities between maxima/minima, with minimal enveloping at large film thicknesses (as found early on in the spin-coating process). In addition, for a longer wavelength illumination source the consecutive maxima will be spaced further apart in time as a film thins, facilitating the acquisition of more data points between the consecutive maxima and increasing the accuracy of the position (in time) of the maxima intensities.

In this set-up a near monochromatic red LED (λ = 620 nm, $\Delta\lambda$ = 20 nm FWHM) is employed as the illumination source and constructive maxima will therefore be observed every time the film thins through intervals of 206.67 nm (for a film with an average refractive of 1.5). The dynamic microscopy images taken during spin-coating periodically flash from bright to dark as the film thins and the contrast in the observed images reflects a combination of the topographical height differences between regions and the refractive index.

For comparison between LED illumination and laser illumination reflectivity data obtained by Heriot and Jones using a HeNe laser (λ = 633 nm) is

shown in Figure 2.4.(3) The data shows a large number of discernable interference fringes, with very little of the enveloping observed in Figure 2.3.

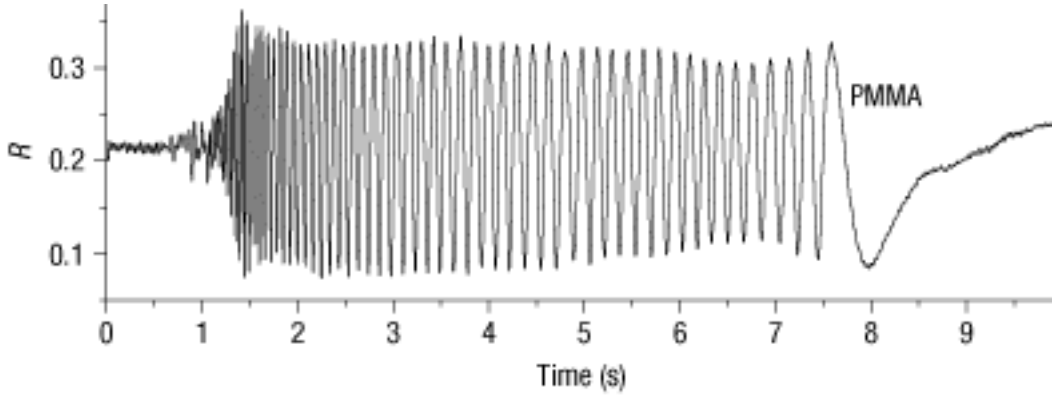

Figure 2.4: Profile showing oscillations in spectral reflectivity obtained using an LED with a small FHWM (~0.2 nm). Taken for a 10 wt% PMMA in toluene, spun-cast at 1500 rpm illuminated with a HeNe laser (λ_{max} = 633 nm, FHWM ~ 0.2 nm).(3)

A series of stroboscopic microscopy images taken during spin-coating may be post-processed to generate drying rate curves (film thickness as a function of time) analogous to those obtained from specular reflectivity measurements. Drying rate curves are generated via an automated fringe counting programme developed using LabView. The data is normalised between zero and one and is then interpolated to improve the accuracy of a peak-picking algorithm. The data is then squared so that both maxima and minima are detected by the peak picking algorithm, which logs the position (in time) of the maxima and minima. A drying curve is produced by subtracting a thickness of $d = \frac{\lambda}{4n}$, at every point where peaks where detected (the value is half, as both consecutive maxima and minima are measured). The drying curve is then set on an absolute scale by adjusting the final

end height to correspond to averaged data obtained by *ex situ* characterisation methods (such as atomic force microscopy (AFM) scratch testing).

After initial hydrodynamic thinning,(4) changes in the film thickness are predominantly caused by removal of solvent from the system.(5) As the effect of solvent is merely to dilute the polymers and so diminish the number of unfavourable contacts between segments of different types,(6) it is possible to calculate the volume fraction of polymer as the percentage change in the absolute film height, which is calculated from the obtained drying curves (based on the assumption of ~97% solvent content when interference is initially observed and ~0% solvent content in the final cast film).

In Chapter 3 I will present results of the observation of the phase separation of PS with poly(methyl methacrylate) (PMMA) as a function of rotation rate obtained using this interferometry approach.(7, 8)

2.2 Compositional mode of operation

One of the drawbacks with the above mentioned interferometric mode of operation is that constructive interference is dependent upon optical thickness (= $n \times d$), where d is the thickness and n is the refractive index. As such, observed "structural developments" cannot be exclusively attributed to either topographical or compositional fluctuations alone. Through studying the observed fluorescence of a fluorescent polymer in a polymer blend comprising of fluorescent + non-fluorescent polymers, the observed contrast reflects composition, exclusively. The stroboscopic fluorescence set-up, utilises an illumination source with a wavelength matching the excitation wavelength of the fluorophore studied, with an

appropriate filter-cube (excitation filter, dichroic mirror and emission filter) to effectively separate the excitation from the emitted wavelengths.

Fluorescence is the spontaneous emission of radiation occurring within nanoseconds of absorption of excitation radiation. Fluorescence occurs when light radiation is absorbed, exciting an electron from the ground singlet state (S_0), to a higher singlet state ($S_{1,2...}$). The electron will lose some energy via vibrational relaxation (heat) and will nonradiatively decay to the lowest electronically excited state. A radiative transition then occurs as the electron returns to the ground state. Fluorescence occurs at longer wavelengths (lower energies) than the incident radiation as the radiative decay occurs after vibrational energy has been discarded to the surroundings, which is known as Stokes' shift.(9) The sequence of steps that lead to fluorescence and characteristic absorption and emission spectra are shown in Figure 2.5.

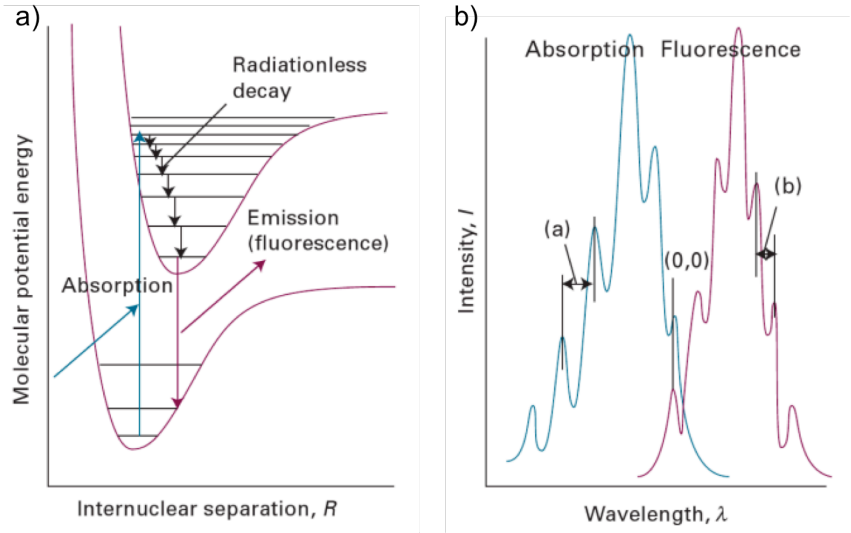

Figure 2.5. Schematics showing; a) steps leading to fluorescence, b) characteristic absorption and fluorescence spectra. Taken and adapted from (9).

The fluorescent polymer chosen for this work this work was poly(9,9'-dioctylflourene) (PFO). The fluorescence spectra of PFO (Figure 2.6), shows the

absorbance occurs between 340 and 400 nm and emission between 400 and 460 nm. A UV LED (λ_{max} = 360 nm) is employed to excite PFO, with a Nikon UVA-2 filter cube to separate the excitation and emission wavelengths.

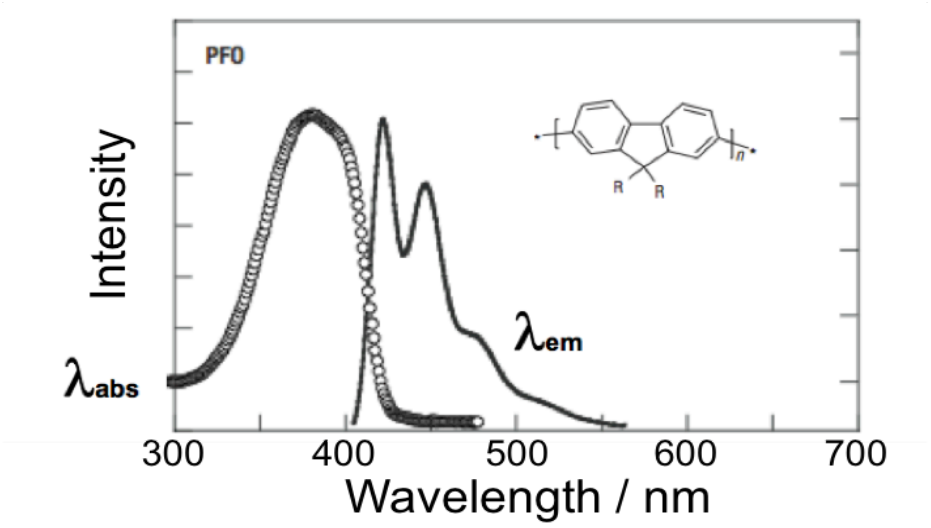

Figure 2.6: The absorption (dotted line) and photoluminescence emission (solid line) spectra for poly(9,9'-dioctly flourene). Taken from reference (10).

In addition, I have further developed this technique to employ real-time fast Fourier transform (FFT) analysis of the acquired images in a feedback loop, which subsequently controls the rotation rate, in order to obtain targeted morphologies. This approach will be discussed in more detail in Chapter 4.

In Chapter 4 I will show how I have used this florescence approach to study the compositional dependence of phase separation in blends of PFO and PS. Further, I will show how *in situ* feedback protocols can be used to control the phase separation processes. This mode of operation was also employed in Chapter 5 to investigate the effect of polydispersity on the phase separation in blends of PFO and PS.

2.3 Crystallisation mode of operation

As discussed in Section 1.2.4, polymer chains often crystallise through either π-π stacking or the formation of chain folded lamellae that may additionally self organise to form high order structures known as spherulites that grow out from central nuclei. Spherulites are highly birefringent (as shown in Figure 2.7) due to their high degree of anisotropic ordering and are therefore typically studied through polarised light microscopy.

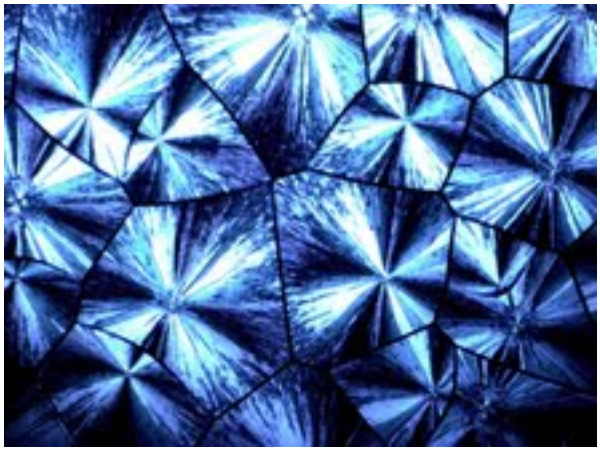

Figure 2.7. A series of spherulites of poly(ethylene glycol) imaged under crossed polarisers.

Electromagnetic radiation propagates through space with oscillating electric and magnetic field vectors alternating in sinusoidal patterns that are perpendicular to one another and to the direction of wave propagation. In the case of non-polarised light, the electric field vectors vibrate in all directions. Whereas, for plane (also referred to as linear) polarised light the electric field vectors are restricted to a single plane, with respect to the propagation direction. . A polarising light filter (or polariser) only allows light of a single vibration direction to pass through, resulting in plane-polarised light. If a second polariser is introduced (termed the analyser),

after the first, the intensity transmitted through the analyser is given by Malus's law:(11)

$$I_\theta = I_0 cos^2\theta \qquad (2.3)$$

where θ is the orientation of the analyser with respect to the polariser.

When the analyser is orientated at an angle of 90°, $I_{90°} = 0$, due to the fact that the electric field of the polarised light from the polariser is perpendicular to the transmission axis of the analyser. When the polariser and analyser filters are aligned perpendicularly they are termed to be crossed, a schematic of which is shown below in Figure 2.8.

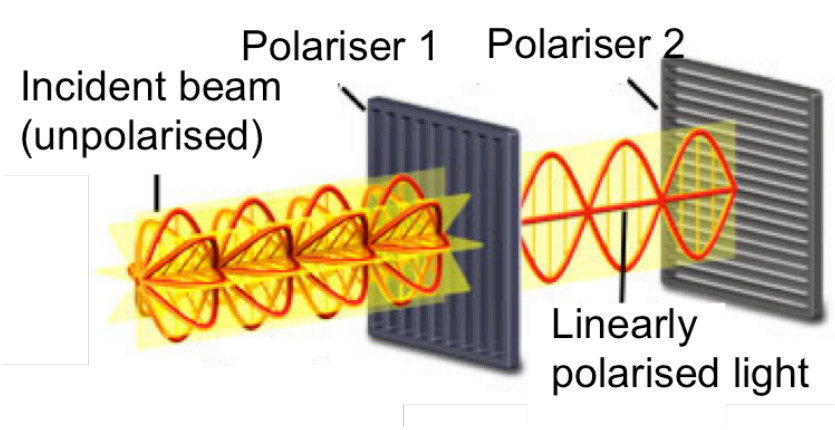

Figure 2.8. Schematic showing a birefringent crystal placed between two polarizers whose vibration directions are perpendicular to each other (and oriented according to the arrows next to the polariser and analyser labels). Taken from (12).

Isotropic samples, such as non-crystalline polymer films, have only one refractive index and no restriction on the vibration direction of the light passing through them. Whereas anistropic samples posses distinct axes and so interactions with light are dependant upon the orientation of crystalline ordering with respect to the incident light. When an anisotropic sample is placed between the polariser and

analyser, image contrast arises from the interaction of the plane polarised light with the birefringent (or doubly refracting) specimen, producing two individual wave components, termed the ordinary and extraordinary. These wave components are orientated perpendicularly to each other and will have different velocities. The ordinary component travels at the same velocity in every direction through the sample, whilst the velocity of extraordinary component is dependant upon the propagation direction of the sample. The result of these differing velocities is that the two components will become out of phase and this phase difference increases with increasing crystal thickness. The ordinary and extraordinary wave components will recombine with constructive/destructive interference effects and only those components parallel to the polarisation direction of the analyser will be observed. The birefringence of a material is defined by the difference in the refractive indices of the ordinary and extraordinary components and increases with increasing crystal thickness.

When a polymer spherulite is imaged using polarised light microscopy a 'Maltese cross' shape is observed, as shown in Figure 2.7. This pattern occurs due to the large degree of crystalline ordering orientated 360° from the central nucleus altering the polarisation of the incident light. (13)

In order to study the growth of spherulites during the spin-coating of semi-crystalline polymers a high-intensity white LED with crossed polarisers was incorporated into the stroboscopic microscopy set-up, providing information regarding crystallisation kinetics during processing.

In Chapter 6 I will show the effect of concentration and the rate of acceleration on the crystallisation of a model polymer system poly(ethylene glycol) (PEG). I will further show the interplay between phase separation and

crystallisation in PEG:PS blends by employing tandem experimental runs of normal monochromatic interferometry (phase separation) with crossed polarisers (crystallisation).

2.4 References

1. Cree. Cree XLamp Product Family Data Sheet 2014 [cited 2014 9.4.2014]. Available from: http://www.cree.com/~/media/Files/Cree/.../XLamp/.../XLampXPE.pdf.
2. Koyama K. Simple interferometric microscopy for in situ real time two dimensional observation of crystal growth. Rev Sci Instrum. 1996;67(7):2584.
3. Heriot SY, Jones RAL. An interfacial instability in a transient wetting layer leads to lateral phase separation in thin spin-cast polymer-blend films. Nat Mater. 2005;4(10):782-6.
4. Emslie AG, Bonner FT, Peck LG. FLOW OF A VISCOUS LIQUID ON A ROTATING DISK. Journal of Applied Physics. 1958;29(5):858-62.
5. Meyerhofer D. Characteristics of resist films produced by spinning: AIP; 1978. 3993-7 p.
6. Zeman L, Patterson D. Effect of the solvent on polymer incompatibility in solution. Macromolecules. 1972;5(4):513-6.
7. Ebbens S, Hodgkinson R, Parnell AJ, Dunbar A, Martin SJ, Topham PD, et al. In situ imaging and height reconstruction of phase separation processes in polymer blends during spin coating. ACS Nano. 2011;5(6):5124-31.
8. Toolan DTW, Haq Eu, Dunbar A, Ebbens S, Clarke N, Topham PD, et al. Direct observation of morphological development during the spin-coating of polystyrene-poly(methyl methacrylate) polymer blends. Journal of Polymer Science Part B: Polymer Physics. 2013;51(11):875-81.
9. Atkins P, De Paula J. Atkins' physical chemistry: Oxford University Press; 2010.
10. Chappell J, Lidzey DG, Jukes PC, Higgins AM, Thompson RL, O'Connor S, et al. Correlating structure with fluorescence emission in phase-separated conjugated-polymer blends. Nature Materials. 2003;2(9):616-21.
11. Hecht E, Zajac A. Optics Addison-Wesley. Reading, Mass. 1974:301-5.
12. Olympus microscopy - birefringence [Web Article]. 2014 [cited 2014 29.3.2014]. Image of crossed polariser microscope set-up]. Available from: http://www.olympusmicro.com/primer/lightandcolor/birefringence.html.
13. Geoghegan M, Hadziioannou G. Polymer Electronics: Oxford University Press; 2013.

Chapter 3. Effect of spin-speed

Parts of this chapter were published in:

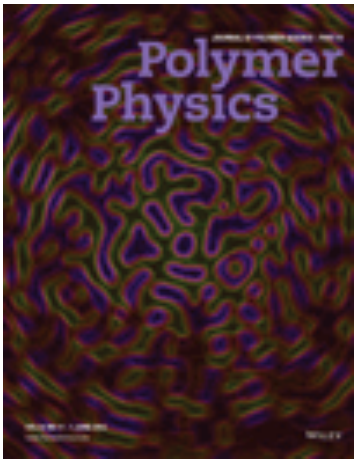

Toolan, D. T. W., *et al*. "Direct observation of morphological development during the spin-coating of polystyrene-poly(methyl methacrylate) polymer blends". *Journal of Polymer Science Part B: Polymer Physics* **51**, (2013) 875-881, DOI:10.1002/polb.23288.

3.0 Introduction

Whether a polymer blend is processed via melt or solution processing techniques, the variable in all cases is the interaction parameter χ, which characterises the strength of the interactions between the components of the polymer blend. As discussed in Section 1.2, the strength of this interaction is controlled via either the temperature of the system ($\chi \propto 1/T$) in a simple binary component (polymer:polymer) system, or via the addition of solvent in ternary system (polymer:polmer:solvent).(1, 2) Rapid changes in χ, equivalent to large jumps through the phase diagram can be achieved through rapid temperature quenches.(3) However, in the case of ternary systems, when solvent is present, the path, or steepness, of the jump is limited by the time required to physically remove the solvent. In such systems, variable quenches in χ are possible, for films prepared by spin coating, where the quench is highly dependant upon the rate of evaporation and hence the rotation rate. Faster spin-speeds have the effect of increasing the rate of evaporation of the solvent from the surface of the film, through increased air flow.

Numerous studies have shown that the characteristic final length-scale of phase-separated morphologies decreases with increasing spin speed.(4-6) However, all of these studies have been based upon *ex situ* measurements of the final cast film and so the mechanism by which morphological development proceeds must be inferred from an informed hypothesis. Due to the large number of parameters that have been shown to affect the final morphology, (molecular weight,(7) tacticity,(8) viscosity,(9) substrate surface chemistry,(10) topography(11) and the process parameters spin-speed(12) and acceleration(13))

this approach is challenging. Walheim *et al.* observed that the morphologies of polymer blends spin-coated at decreasing spin-speeds appeared to exhibit similar domain structures with an increasing length-scale. This was attributed to longer drying times, allowing longer diffusion times and a higher degree of phase coarsening.(4)

In this chapter I show how I have employed the technique of stroboscopic interference microscopy,(14) to study the effect of spin-speed on morphological development in a blend of PS:PMMA spin-coated from a low vapour pressure solvent, *ortho*-xylene. This approach has allowed direct observation of the bicontinuous morphologies formed through spinodal decomposition, which subsequently coarsen and coalesce. I am able to show how spin-speed, and hence the rate of the quench through the phase diagram, controls the amount of phase coarsening allowed to take place, which determines the characteristic length-scale of the final bicontinuous morphology. Through post processing the *in situ* optical micrographs (as outlined in Section 2.1) it is possible to obtain quantitative drying rate information and polymer volume fraction over the course of the process, at different spin-speeds.

3.1 Experimental

The technique of stroboscopic microscopy in an interference set-up was employed (as described in Section 2.1), where a extra long working distance (ELWD) 20x objective, 620 nm LED (Cree X lamp) and an Andor Neo sCMOS where employed (quantum efficiency of 55% at 620 nm, field of view of 183 x 180 μm when used in conjunction with a ELWD objective x20, NA 0.45).

Solutions of poly(methyl methacrylate) (PMMA) (Polymer Laboratories M_p = 685,000 Da (M_p is the molecular weight at the peak maximum), M_w/M_n = 1.1, part no: 20240) and polystyrene (PS) (Polymer Source Inc. M_w = 641,000 Da, M_w/M_n = 1.11, sample no: P2767-S) were made up in *ortho*-xylene (Aldrich) at 3 wt% and stirred continuously for 24 hr. The solutions were then mixed at 1:4 volume ratios prior to spin casting. Silicon substrate (100) was cleaned in piranha solution (H_2SO_4:H_2O_2, 1:1) for 6 hrs, followed by multiple rinsing with distilled water. A square of freshly cut Si (10 x 10 mm) was placed on the spin-coater and the focusing was adjusted to "imperfections" on the substrate surface. 50 µl of solution was dispensed onto the substrate and then spun at the designated speed, with data collected for 600 exposures, corresponding to 24 seconds (at 1500 rpm) and 6.6 seconds (at 5500 rpm).

3.2 Results and Discussion

Real-space stroboscopic interference images, reciprocal space Fast Fourier transforms (FFTs) and the radially averaged FFT intensity plot show the morphological development of a PS:PMMA blend spun-cast at 1500 rpm (Figure 3.1 and Figure 3.2, Movie 3.1).[a]

Faint structure is first visible in both the real-space and FFT images at 5.04 s (Figure 3.1i and Figure 3.2). The real-space image reveals that a phase separated bicontinuous morphology is present, which has a corresponding well

[a] All movies related to this thesis are available at http://www.youtube.com/user/danieltwtoolan

Movie 3.1 is available at http://youtu.be/ShvR3X8NJow.

defined ring in the FFT data, indicating a dominant length-scale of ~ 4.2 μm (1.5 ±0.4 μm^{-1}). This bicontinuous morphology is indicative of spinodal decomposition. The initial structure appears faint due to the film being thick, and the difference between maxima and minima is much smaller compared to that of a thinner film. After 5.04 s the dominant length-scale of the bicontinuous morphology grows and domain coarsening begins to take place (Figure 3.1ii-v). The growth of the dominant length-scale is highly visible in the radially averaged FFT data (Figure 3.2), where Q[b] rapidly decreases from ~1.5 to ~0.5 ±0.1 μm^{-1} pixels. The real-space data shows that a bicontinuous morphology is maintained throughout this process. After 8s the growth of domains is considerably slower than initially observed and the morphology resembles that of the final cast film. However, much slower large scale domain coarsening occurs until ~14 s (Figure 3.1vi-xi). This process is highlighted in Figure 3.3, which has an outline of the final morphology overlaid on-top of the real-space images. Domain growth and coarsening is driven by an increase in the χ_{eff} as the film thins through the loss of solvent, which in turn causes polymer diffusion from areas of low concentration to those of high concentration in order to minimise the interfacial energy.

[b] Where Q is the reciprocal lengthscale ($d = (2\pi)/Q$)

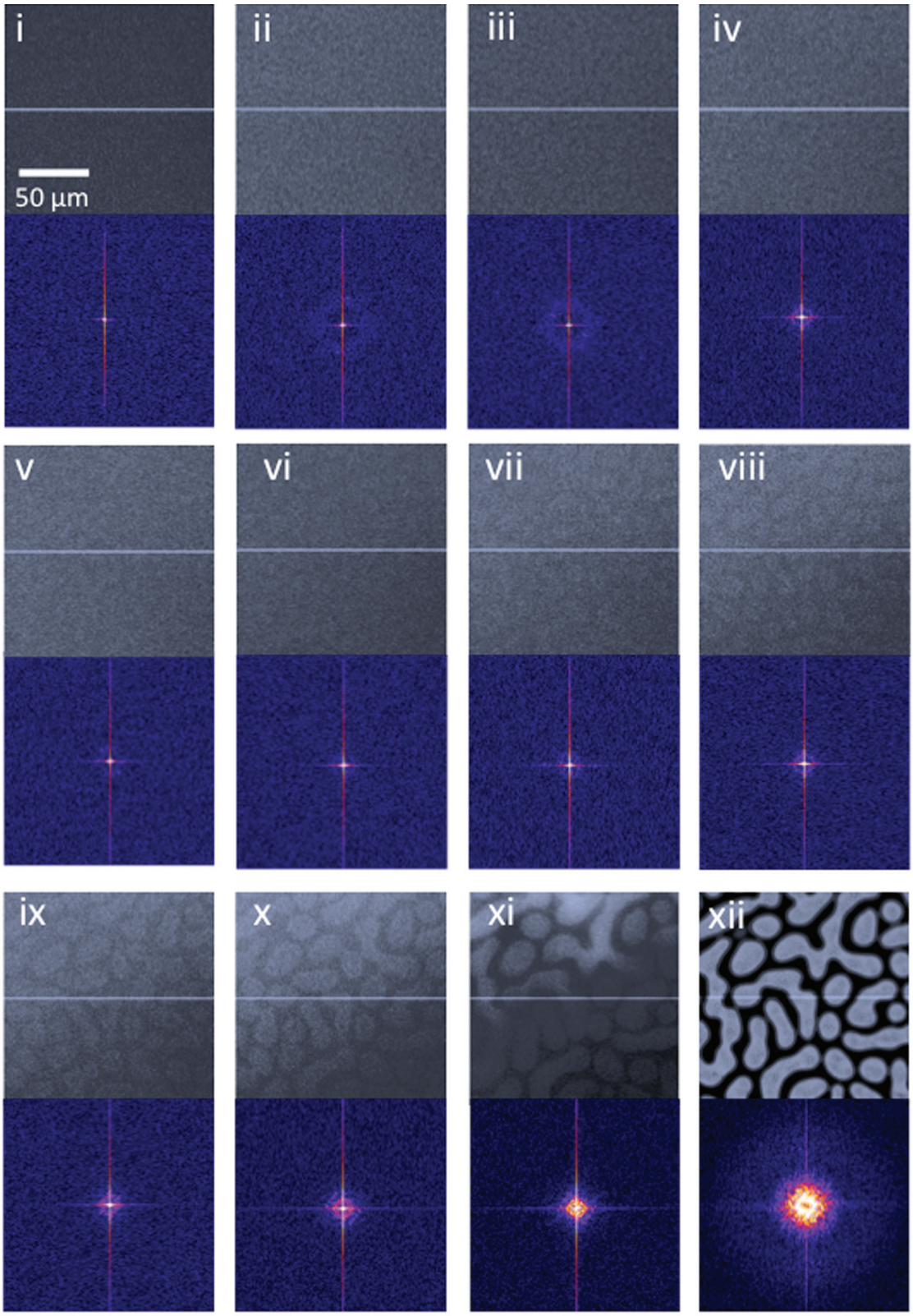

Figure 3.1. Direct observation of phase separation in blends of PS:PMMA (1:4 by volume) spun-cast (3 wt% at 1500 rpm) from *ortho*-xylene, (i-xii) 0.00, 5.04, 5.48, 6.00, 6.52, 7.04, 7.60, 8.16, 8.72, 9.84, 12.56 and 15.60 s.

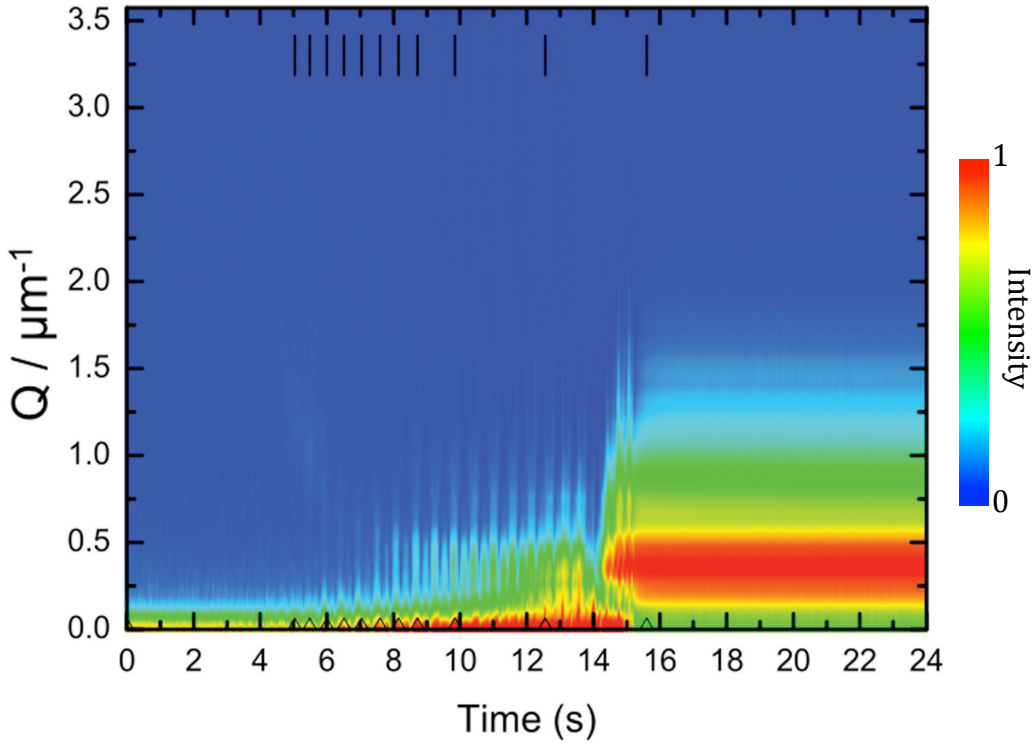

Figure 3.2. Radial averages of Fourier transformed data as a function of time of PS:PMMA (1:4 by volume) spun-cast (3 wt% at 1500 rpm) from *ortho*-xylene.

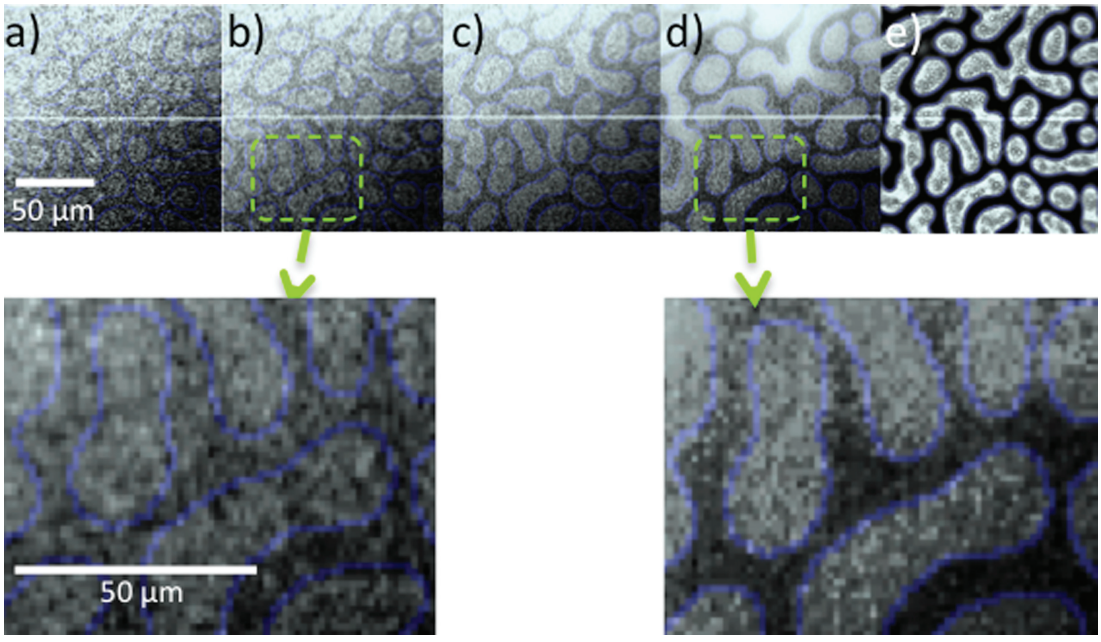

Figure 3.3. Stroboscopic optical reflectance images overlaid with the final morphology of the dry film at (a-e) 8.16, 8.72, 12.56 13.84 and 15.60 s, respectively, highlighting the ripening process.

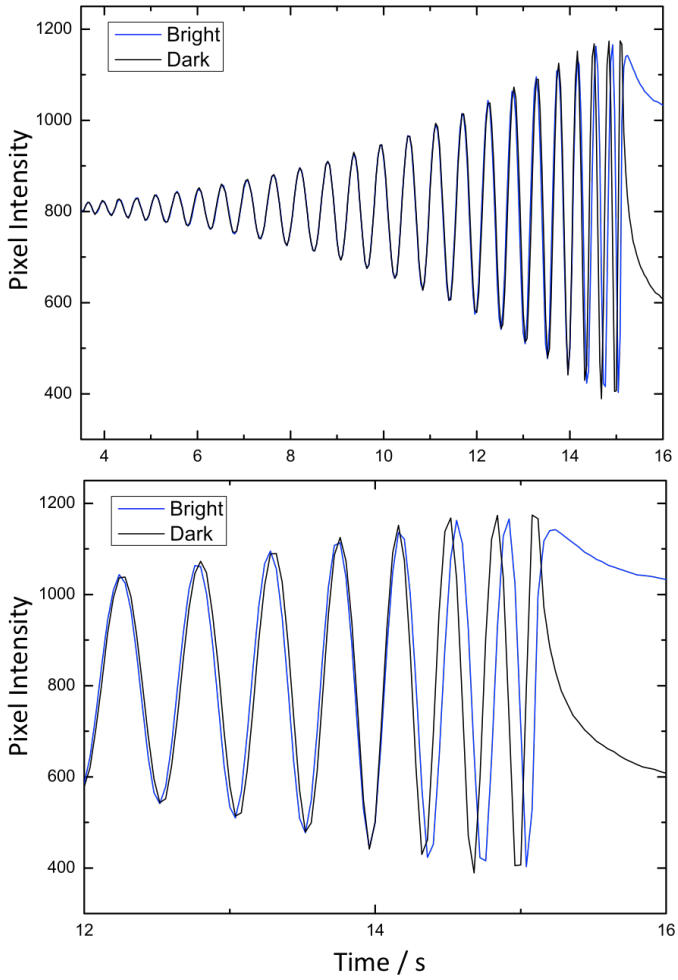

Figure 3.4. Profiles of pixel intensity for final bright and dark pixels taken from *in situ* optical reflectance images for blends of PS:PMMA (1:4 by volume) spun-cast (3 wt% at 1500 rpm) from *ortho*-xylene, highlighting an interference phenomenon at 14 s, leading to an apparent loss of structure.

At 14 s there is an apparent "loss" of structure in the radially averaged data (Figure 3.2). Mokarian-Tabari *et al.*(15) observed a similar phenomenon in laser scattering data studying blends of PS:PMMA, spun-cast in an environmental cell to control the evaporation rate (Figure 1.28). The loss in structure was thought to be caused by a break-up in structure occurring before the final structure was formed. Analysis of the frames in the real-space data either side of this phenomena indicate that there was no apparent change in the morphology of the film (Figure 3.3 d and e).

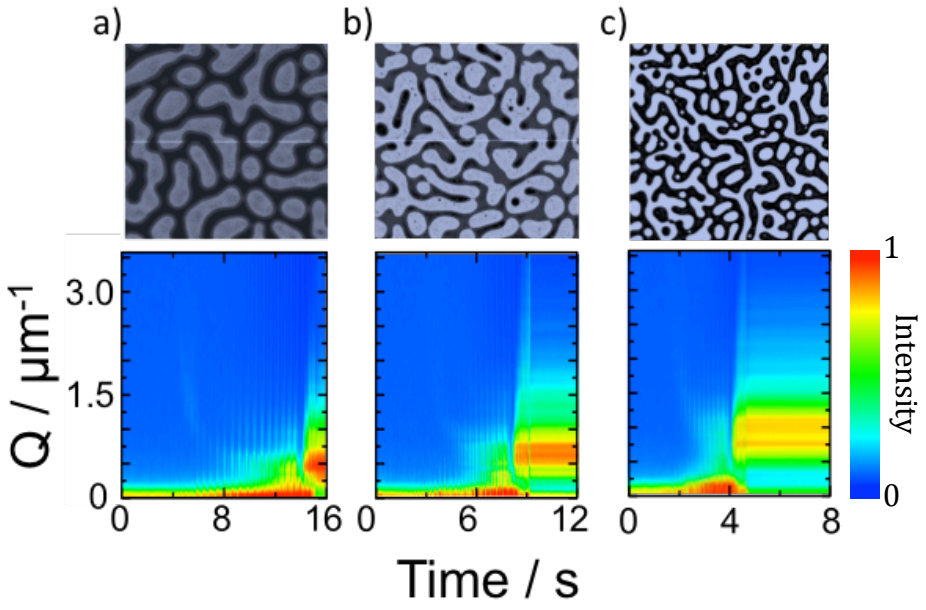

Figure 3.5 Final optical reflectance images (top) and radially averaged Fourier transformed data as a function of time (bottom) showing the morphological development for blends of PS:PMMA (1:4 by volume) spun-cast at (a) 1500, (b) 2000, (c) 3000 rpm spun-cast from 3 wt% *ortho*-xylene.

Figure 3.4 (top) shows curves for representative final "bright" and "dark" pixel regions for the morphological development of the PS:PMMA blend spun-cast at 1500 rpm, showing the characteristic maxima/minima arising due to constructive interference as the film thins. Figure 3.4 (bottom) graph focuses on oscillations in the pixel intensity between 12 and 16 s, where the FFT (Figure 3.2) shows an apparent loss of structure. The graph shows that before and after 14 s the intensity oscillations of the final bright and dark pixels are slightly out of phase, which results in contrast in the real-space images, whilst at 14 s the bright and dark pixel intensities are completely in phase and so there is no contrast between bright and dark pixels and so there appears to be a "loss" of structure. The analysis presented here shows that for this system studied, there is no break-up in structure as observed by Mokarian-Tabari *et al*.

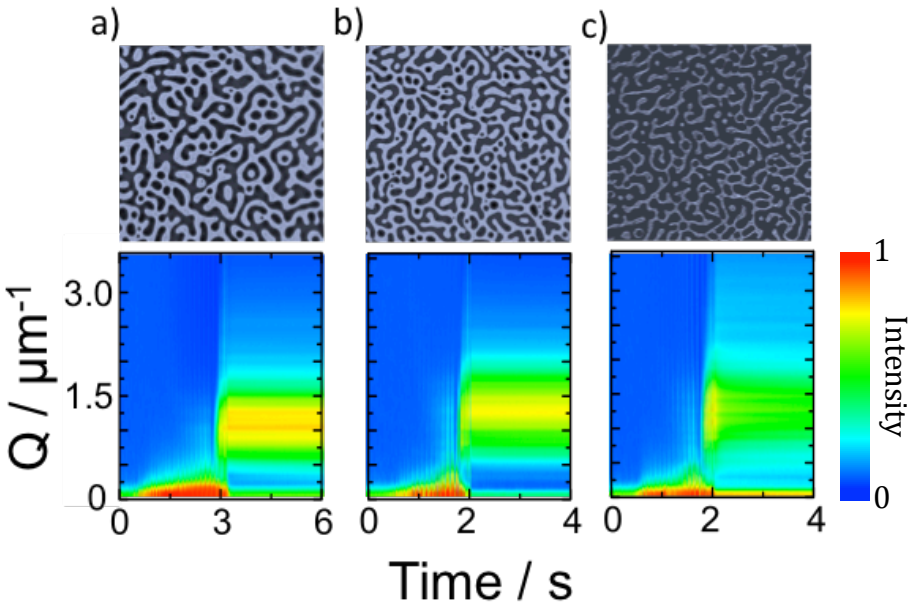

Figure 3.6 Final optical reflectance images (top) and radially averaged Fourier transformed data as a function of time (bottom) showing the morphological development for blends of PS:PMMA (1:4 by volume) spun-cast at (a) 4000, (b) 5000, (c) 5500 rpm spun-cast from 3 wt% *ortho*-xylene.

Figure 3.5 and 3.6 (Movies 3.5 - 3.6[c]) show the final morphologies and radial average of the FFT of the stroboscopic images for films spin-coated at speeds between 1500 and 5500 rpm. All of the films exhibit a well-defined phase separated, bicontinuous morphology, independent of spin-speed. As observed previously by Walheim *et al.*(4) the dominant length-scale of the final morphology decreased with increasing spin-speed. The radially averaged FFT data shows that morphological development proceeds in a similar manner for all of the films independent of spin-speed: all films exhibit an initial "faint" length-scale with a

[c] Movies for blends spun-cast at various speeds are available at: http://youtu.be/awm5sUr-9bY (2000 rpm), http://youtu.be/1edIgwlMoIU (3000 rpm), http://youtu.be/M46JsxtXhmo (4000 rpm) and http://youtu.be/M46JsxtXhmo (5000 rpm).

high value of Q, corresponding to small scale structure. The Q value then proceeds to decrease as a function of time and corresponds to the process of domain coarsening shown in Figure 3.2 and Figure 3.3. Both the onset of the initial observable length-scale and the point at which the morphology is fixed are inversely proportional to spin-speed. Therefore higher spin-speeds cause phase separation to occur at an earlier point in time from where the process initially starts as well as fixing the morphology through earlier vitrification. Such processes are related to the depth of the quench through the phase diagram.

Quantitative drying and polymer volume fraction curves are shown in Figure 3.7 and 3.8 respectively, for polymer blends spun-cast between 1500 and 5500 rpm. Drying height curves where obtained by subtracting a thickness of $d = \frac{\lambda}{4n}$, between maxima and minima and offsetting the final height with averaged *ex situ* film thickness measurements made via AFM. The polymer volume fraction curves where obtained from the drying height curves and are based on the assumption of an initial homogenous mixture (3 wt% polymer), when consecutive maxima/minima are first observed and that the film is completely free of solvent (100 wt% polymer). Drying height data (Figure 3.7) is presented for both bright and dark phases in the *in situ* optical micrographs. Whether a phase appears bright or dark is determined by the Bragg equation, for our experimental set-up constructive interference occurs at multiples of 206.67 nm. The initial height of the films at the point when successive constructive/destructive interference was observed decreased with increasing spin-speed. This is caused by a greater degree of hydrodynamic thinning for polymer blends spun-cast at higher speed. The drying rate curves show that as spin-speed increases the rate of film thinning

increases, due to increased air-flow. At spin-speeds of 5000 and 5500 rpm there is only a small increase in the rate of film thinning, indicating the system is approaching the limit at which solvent can diffuse to the surface of the film.

The standard error of the drying height data was calculated based on six regions on three different samples. The error was found to have a maximum value of 15 nm over the whole drying process, indicating the homogeneity and reproducibility of polymer films produced via spin-coating. As such, error bars have not been plotted in Figure 3.7 due to the difference in the orders of magnitude of the error and the film height.

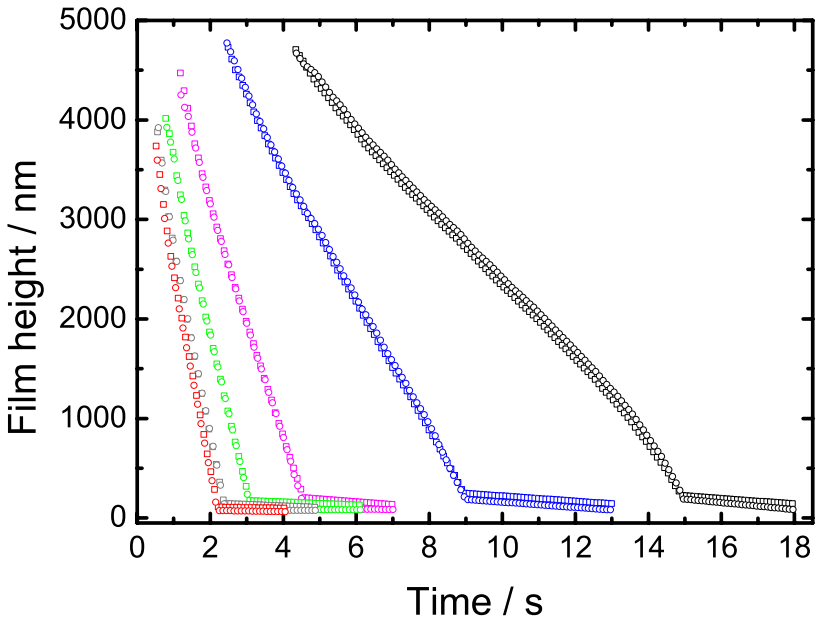

Figure 3.7. Quantitative drying curves obtained from stroboscopic interference image time stacks for blends of PS:PMMA (1:4 by volume) spun-cast at 3 wt% from *ortho*-xylene at speeds of 1500 (black), 2000 (blue), 3000 (magenta), 4000 (green), 5000 (grey) and 5500 rpm (red) for both bright (circles) and dark (squares) phases in the movies showing that as spin-speed increases the rate of film thinning increases.

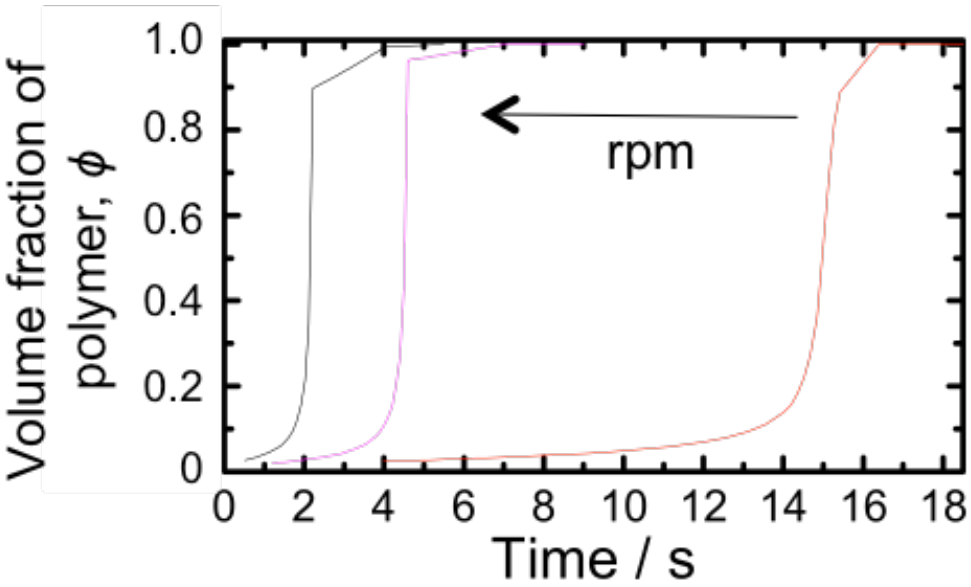

Figure 3.8. Graph showing volume fraction of polymer vs time for a 3 wt% PS:PMMA (1:4 by volume) in *ortho*-xylene spun at speeds of 1500 (black), 3000 (magenta) and 5500 rpm (red) showing the depth of the quench through the phase diagram.

The curves of volume fraction of polymer for blends spun-cast between 1500 and 5500 rpm provide information regarding the nature of the quench through the phase diagram and show that as the spin-speed increases the rate that the polymer blend is quenched is greater and so the resultant morphology is "frozen" further from equilibrium. In contrast, a blend spun-cast at a slower spin-speed, is quenched much more slowly and the system is able to adopt a morphology with a larger lengthscale in order to minimize the interfacial energy. The rate of the quench is therefore critical in dictating the dominant length-scale of the final morphology, as it determines the degree of phase coarsening that occurs to minimise the interfacial energy, explaining the relationship between the spin-speed, quench and the dominant length-scale.

The direct observation of domain growth in this study is contrary to observations made by Ebbens *et al*,(14) studying the phase separation of PS:PI spun from *ortho*-xylene, at 1500 rpm. The PS:PI blend was studied using the same experimental set-up discussed in this work, apart from the use of a green LED with a 10 nm bandpass filter as the illumination source. For the PS:PI blend spun at 1500 rpm from *ortho*-xylene the final structure appeared to be fixed early on in the drying process. The alternate behaviour observed between blends of PS:PMMA and PS:PI may be ascribed to the difference in the surface free energies of PS, PMMA & PI. In the blend of the PS:PMMA blend there is a large difference in the surface free energies of the homopolymers and as-such there is a large driving force for domain coarsening. On the other hand, in the blend of PS:PI there is a smaller difference in the surface free energies of the homo-polymers, and so the driving force for domain coarsening is reduced and so the morphology appears to

be simply controlled by phase separation as opposed to a combination of phase separation and coarsening.

Dalnoki-Veress studied phase separation in high molecular weight PS:PI spun-cast from toluene at spin-speeds ranging from 700 to 7000 rpm.(5) Their study revealed a decrease in domain area with increasing spin-speed. From the information obtained in this study and of that by *Ebbens*, I believe that a steeper quench in a PS:PI blend through employing either a higher vapour pressure solvent or a higher spin-speed, may result in the observation of a morphology with a smaller characteristic length-scale.

3.3 Conclusions

I have been able to directly observe bicontinuous morphologies grow and coarsen, using the technique of high-speed stroboscopic interferometry. Furthermore we have been able to obtain quantitative drying and χ_{eff} curves, allowing me to quantify the depth of the quench into the two-phase region of the phase diagram, at spin-speeds ranging from 1500 to 5500 rpm. I have shown that for the blend of PS:PMMA spun-cast from *ortho*-xylene the process of morphological development occurs in the same manner independent of spin-speed. However, spin-speed affects the characteristic length-scale of the final morphology by affecting the amount of phase coarsening which can occur before vitrificaiton occurs. Therefore blends spin-coated at a high spin-speed and thus a high rate of evaporation had a significantly smaller degree of phase coarsening than blends spun-cast at slower speeds.

3.4 References

1. Jones RAL. Soft condensed matter: Oxford University Press; 2002.
2. Zeman L, Patterson D. Effect of the solvent on polymer incompatibility in solution. Macromolecules. 1972;5(4):513-6.
3. Okada M, Kwak KD, Chiba T, Nose T. Phase separation morphology in the critical to off-critical crossover region. Macromolecules. 1993;26(24):6681-3.
4. Walheim S, Boltau M, Mlynek J, Krausch G, Steiner U. Structure formation via polymer demixing in spin-cast films. Macromolecules. 1997;30(17):4995-5003.
5. Dalnoki-Veress K, Forrest JA, Stevens JR, Dutcher JR. Phase separation morphology of spin-coated polymer blend thin films. Physica A: Statistical Mechanics and its Applications. 1997;239(1-3):87-94.
6. Fang L, Wei M, Barry C, Mead J. Effect of Spin Speed and Solution Concentration on the Directed Assembly of Polymer Blends. Macromolecules. 2010;43(23):9747-53.
7. Li X, Xing R, Zhang Y, Han Y, An L. Molecular weight effects on the phase morphology of PS/P4VP blend films on homogeneous SAM and heterogeneous SAM/Au substrates. Polymer. 2004;45(5):1637-46.
8. Lee HK, Kim SC. Relation between liquid-liquid phase separation and crystallization in isotactic and syndiotactic polypropylene solutions. Journal of Applied Polymer Science. 1998;67(1):159-63.
9. Wu KH, Lu SY, Chen HL. Formation of parallel strips in thin films of polystyrene/poly(vinyl pyrrolidone) blends via spin coating on unpatterned substrates. Langmuir. 2006;22(19):8029-35.
10. Krausch G. SURFACE-INDUCED SELF-ASSEMBLY IN THIN POLYMER-FILMS. Materials Science & Engineering R-Reports. 1995;14(1-2):1-94.
11. Peurrung LM, Graves DB. FILM THICKNESS PROFILES OVER TOPOGRAPHY IN SPIN COATING. J Electrochem Soc. 1991;138(7):2115-24.
12. Hall DB, Underhill P, Torkelson JM. Spin coating of thin and ultrathin polymer films. Polymer Engineering & Science. 1998;38(12):2039-45.
13. Rehg TJ, Higgins BG. The effects of inertia and interfacial shear on film flow on a rotating disk: AIP; 1988. 1360-71 p.
14. Ebbens S, Hodgkinson R, Parnell AJ, Dunbar A, Martin SJ, Topham PD, et al. In situ imaging and height reconstruction of phase separation processes in polymer blends during spin coating. ACS Nano. 2011;5(6):5124-31.
15. Mokarian-Tabari P, Geoghegan M, Howse JR, Heriot SY, Thompson RL, Jones RAL. Quantitative evaluation of evaporation rate during spin-coating of polymer blend films: Control of film structure through defined-atmosphere solvent-casting. European Physical Journal E. 2010;33(4):283-9.

Chapter 4. Compositional Studies

Parts of this chapter were published in:

Toolan, D. T. W., Parnell, A. J., Topham, P. D. & Howse, J. R. "Directed phase separation of PFO:PS blends during spin-coating using feedback controlled in situ stroboscopic fluorescence microscopy". *Journal of Materials Chemistry A* **1**, 3587-3592 (2013), DOI: 10.1039/C3TA01530K.

4.0 Introduction

As discussed in Chapter 2, one of the drawbacks of using near monochromatic illumination is that the contrast in the resulting images is a consequence of both topography and refractive index, both of which change during phase separation. In addition it is not possible to determine which phase is polymer *a* or polymer *b*, respectively. The process of spinodal decomposition (Section 1.2.2) occurs through the amplification of compositional fluctuations and in order to study such processes it would be hugely beneficial to be able to resolve the composition of the polymer components during spin-coating.

In this Chapter, I have employed stroboscopic microscopy in a fluorescent mode of operation (Section 2.2) to study the development of compositional fluctuations and the effect of composition on phase separation in blends of fluorescent and non-fluorescent polymers, poly(9, 9' – dioctyl flourene) (PFO) and PS, respectively. Through studying a fluorescent and non-fluorescent polymer, it is possible to map composition directly to intensity. A maximum pixel intensity will occur only in regions containing the fluorescent polymer and any variations in this detected fluorescence must be due to the presence of a mixed phase containing both fluorescent and non-fluorescent polymer. Such compositional information is not accessible through "normal" interferometry, which is more sensitive to topographical fluctuation than composition fluctuation due to the similarity of the polymers refractive indices.

PFO and related co-polymers have been investigated for applications in LEDs and OPVs and numerous studies have utilised fluorescence microscopy, atomic force microscopy and scanning near-field optical microscopy to investigate the interplay between the final phase-separated morphology and device

performance.(1, 2),(3, 4) Arias *et al* utilised *in situ* fluorescence microscopy to study vitrification in poly[(9,9'-di-n-octylfluorenyl-2,7-diyl)-alt-(benzo[2,1,3]thiadiazol-4,8-diyl)] (F8BT) and poly(9,9'-dioctylfluorene-co-bis-N,N-(4-butylphenyl)-bis-N,N-phenyl-1,4-phenylenediamine) (PFB) films during solvent-casting onto a static substrate, and were able to observe liquid coalescence and coarsening as a solvent front swept across the film.(2)

Further, this chapter also investigates the potential of including real time processing of the acquired images to enable feedback over the spin-coating parameters in order to control and direct the processes of phase separation occurring during spin-coating.

4.1 Experimental

The technique of stroboscopic microscopy in an fluorescence set-up was employed (as described in Section 2.2), comprising of an extra long working distance (ELWD) 60x objective (NA = 0.7), UV illumination from a 360nm LED (Ledegin), a UV2A (Nikon) beam cube to separate the excitation and emission wavelengths, with Andor iXON (897^{+}) and Zyla detectors, which have fields of view of 132 x 132 μm & 104 x 104 μm when used in conjunction with the 60x objective, respectively.

In situ feedback was performed through real-time analysis of stroboscopic fluorescence images captured using LabView, which took an radial integral of the FFT of the stroboscopic image giving a plot of intensity vs Q. An increase in spin speed was triggered when a peak in the high Q region was detected (2.5 μm^{-1} < Q < 2.8 μm^{-1}). Atomic force microscopy images of final morphologies where imaged with a MultiMode SPM with a Nanoscope III controller.

Solutions of poly(9,9'-dioctylfluorene) (PFO) (supplied by Cambridge Display Technologies as CDTGreen003/22) M_w ~ 221,000 Da, M_w/M_n ~ 2.70 and Polystyrene (PS) (Polymer Source Inc.) M_w = 641,000 Da, M_w/M_n = 1.11, sample no: P2767-S where made up in *ortho*-xylene (Aldrich) at 2 wt% and stirred continuously for 24 hr. The solutions where then mixed at 65:35, 60:40 & 55:45 volume ratios prior to spin casting. Silicon substrate (100) were cleaned in piranha solution (H_2SO_4:H_2O_2) (1:1) for 6 hrs, followed by multiple rinsing with distilled water. Glass substrate (Fisher Scientific) were used as received. Each substrate was placed on the chuck and the focusing was adjusted to "imperfections" on the surface. 20 µl of solution was dispensed onto the substrate and then spun at the designated rpm, with data collected for 500 exposures, corresponding to 20 s at 1500 rpm.

4.2 Results and discussion

In situ stroboscopic fluorescence data for PFO:PS blends spun-cast on silicon substrates at compositions of 55:45, 60:40 and 65:35 are shown in Figure 4.1 (corresponding Movies 4.1 a - c, respectively[a]), along with final static fluorescence and AFM images (Figure 4.2) and the radial integrals of the Fourier form transform (FFT) of the respective movies taken for the blends (Figure 4.3).

[a] Movies accompanying Figure 4.1 a – c are available at http://youtu.be/UFBIbfCzAfo (55:45), http://youtu.be/BFJWrK3GYk0 (60:40) and http://youtu.be/QN8AXiZARIk (65:35).

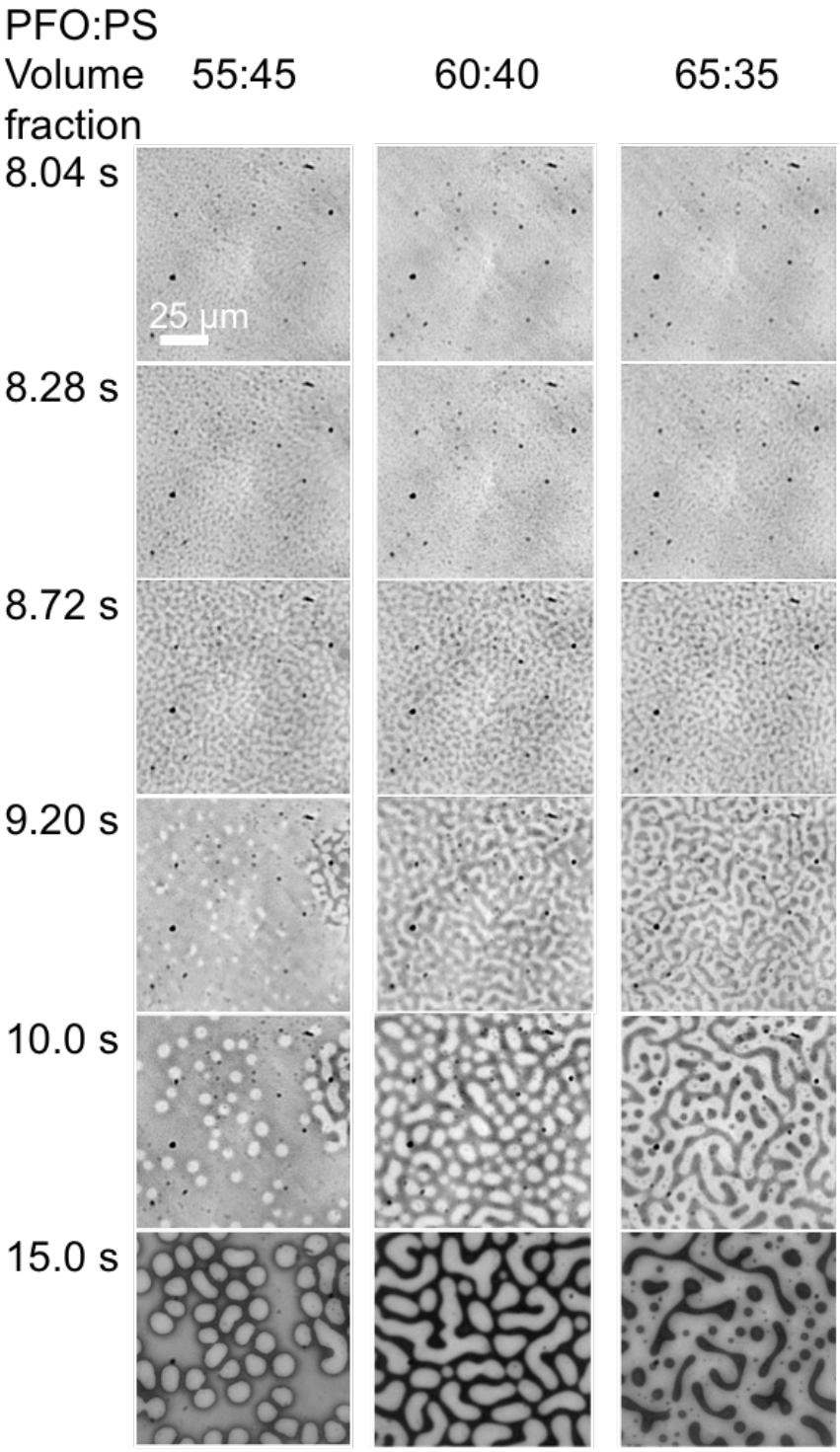

Figure 4.1. Direct observation of phase separation in a blends of PFO:PS (55:45, 60:40, 65:35) spun-cast (2 wt% at 1500 rpm) from *ortho*-xylene on silicon; Stroboscopic fluorescence images at 8.04, 8.28, 8.72, 9.20, 10 & 15 s, respectively.

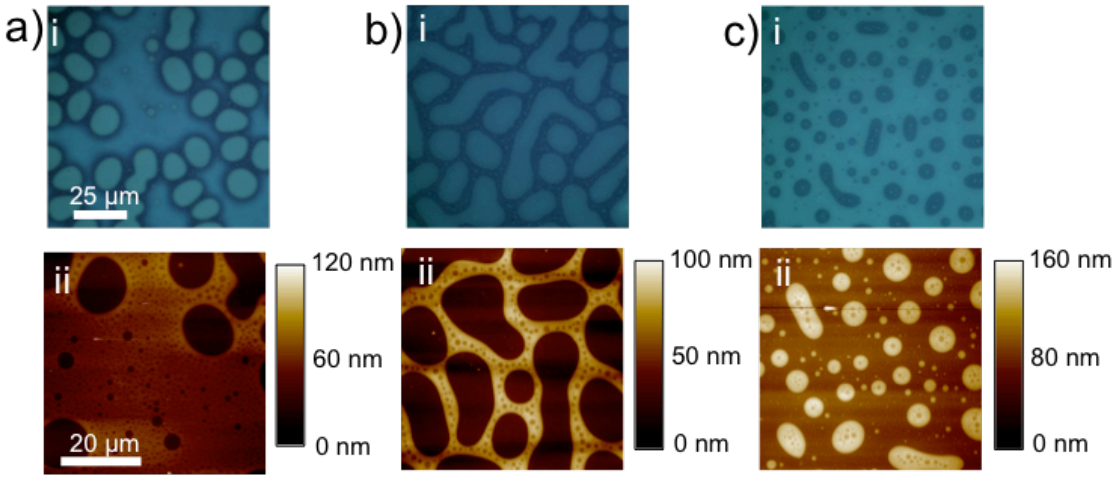

Figure 4.2. Fluorescence (top) and AFM (bottom) images of final morphologies of PFO:PS blends spun-cast at 1500 rpm from *ortho*-xylene on silicon at compositions of; a) 55:45, b) 60:40 and c) 65:35.

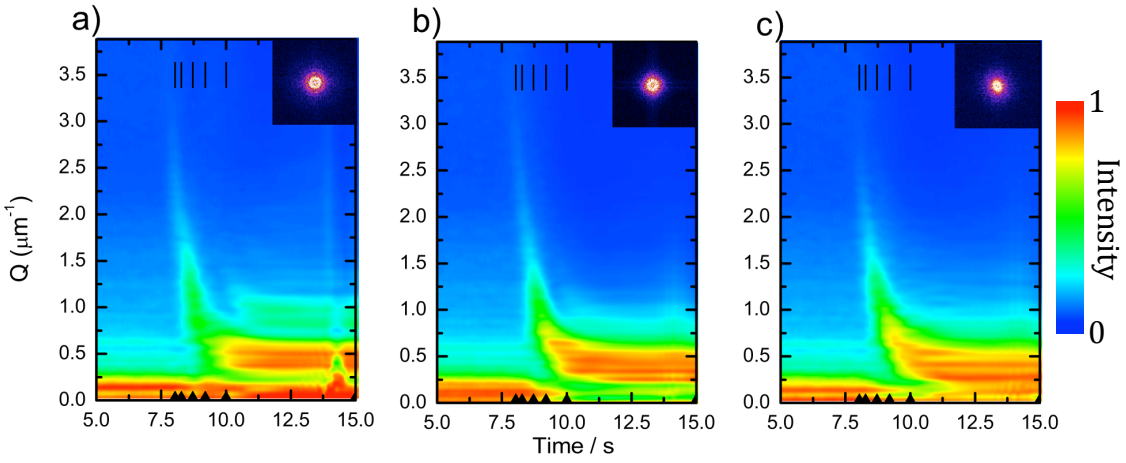

Figure 4.3. Intensity plots of the radial intergrated Fourier transform for a selection of each *in situ* data series for PFO:PS blends spun-cast at 1500 rpm from *ortho*-xylene on silicon at compositions of; a) 55:45, b) 60:40 and c) 65:35. The vertical lines correspond to times for images in Figure 4.1.

The stroboscopic fluorescence data for the 55:45 blend (Figure 4.1 left) show that an initial bicontinuous morphology formed through spinodal decomposition is first visible at 7.5 s, which proceeds to grow through Ostwald ripening. The radially averaged FFT (Figure 4.3) shows the lengthscale of the initial structure ~2.2 μm (Q = 2.8 ±0.3 μm^{-1}), which then grows rapidly to ~14.4 μm (Q = 0.44 ±0.1 μm^{-1}) until 8.68 s. After which point the bicontinuous morphology breaks up, forming discrete islands rich in PFO and a mixed phase of PFO and PS. The resultant islands of PFO then proceed to grow through Ostwald ripening. The radially averaged FFT shows that the rate of domain growth was unaffected by the break-up of the bicontinuous morphology. Secondary domain growth with an initial lengthscale of ~4.5 μm (Q = 1.4 ±0.2 μm^{-1}) is evident on the radial averaged FFT data from 10 s, which grows similarly to the initial primary lengthscale. The mixed phase observed at 8.68 s is apparent in the final fluorescence images (Figure 4.2 a (top)), due to the presence of regions with an intensity corresponding to neither a pure PS phase or a pure PFO phase. The AFM data (Figure 4.2 b (bottom)) reveals that the apparent mixed phase contains sub micron domains of PFO, below the resolution limit of this optical technique. [b] Therefore we can assume that the stroboscopic fluorescence images after 8.68 s contain regions with a sub-micron lengthscale. The data shows (Figure 4.1) that the 55:45 blend undergoes spinodal decomposition forming a bicontinuous morphology, which grows through Ostwald ripening. An instability causes the break up of the bicontinuous morphology,

[b] Optical resolution during spin-coating is a product of dimension, radial velocity and pulse length. Therefore we are not able to resolve domains <1 μm, despite these being well above the resolution limit.

resulting in the formation of discrete islands of PFO with two distinct lengthscales within a matrix of PS. The islands of PFO then proceed to grow through Ostwald ripening to form the final morphology.

Data for the 60:40 blend (Figure 4.1 centre) indicates that phase separation initially proceeds similarly to the 55:45 blend. Unlike the 55:45 blend, following the formation of discrete islands of PFO, phase coarsening re-establishes a bicontinuous morphology. Static fluorescence and AFM data (Figure 4.2 b) reveal a large degree of secondary islands of PFO within the continuous PS phase. The radially averaged FFT data (Figure 4.3 b) show that the initial onset of phase separation and rate of domain growth occurs similarly to the 55:45 blend. As with the previous blends the 65:35 blend exhibits an initial bicontinuous morphology at 7.5 s (Figure 4.1 right), that grows through Ostwald ripening. Both the PFO and PS domains grow, until 9.76 s. At this point the PFO domains continue to grow forming a PFO rich matrix, whilst the PS domains shrink to a smaller size, forming distinct PS islands that are not interconnected. The radially averaged FFT data (Figure 4.3 c) show the same trends as observed for the 55:45 & 60:40 blends. Static fluorescence and AFM data (Figure 4.2 c) show secondary islands of PFO within the PS phase.

For all compositions there exists a common bicontinuous morphology at 7.5 s formed through spinodal decomposition that then grows and coarsens though Ostwald ripening. The bicontinuous morphology breaks up, resulting in the formation of distinct islands within a matrix. We believe this process is triggered by an interfacial instability that leads to the break-up of the bicontinuous morphology. The point at which decay was triggered was shown to be dependent upon composition, occurring at 8.68 s for the 55:45 blend and 9.76 s for the 65:35

blend, which has a critical effect on the final morphology. When the break-up of the bicontinuous morphology is triggered earlier during spin-coating, as in the 55:45 blend, the viscosity of the polymer blend is much lower, so the rate of diffusion is greater and decay triggers the formation of sub micron features. In comparison, when the break up of the bicontinuous morphology is triggered at a much later stage, as in the 65:35 blend, when the viscosity is much greater, the rate of diffusion is much slower. As such the process of decay occurs much more slowly, resulting in the formation of comparatively large distinct islands of PS. A final interconnected morphology is formed in the 60:40 blend as the break up occurs sufficiently early to allow a large degree of phase coarsening of the discrete islands as they grow through Ostwald ripening, whilst not so early as to form structures smaller than that first formed through spinodal decomposition. As the point at which decay was triggered showed a compositional dependence, the effect is likely to be an interfacial instability caused by the difference in surface free energy of the PFO and PS, the contact angles of which are 84.1 ±0.4° and 95.4 ±0.6°, respectively.

The radially averaged FFT data for all blends spun-cast on silicon (Figure 4.3) shows bright/dark banding corresponding to intensity fluctuations between 13 and 15 s, where the last of the solvent is removed via evaporation. These fluctuations occur due to interface effects caused by reflections between the substrate and the surface of the thinning film. The point where consecutive constructive/destructive interference depends on both the wavelenth distribution of the light and the film thickness, as defined by Equation 2.2. The full half width maximum (FWHM) of the emitted fluorescence from PFO is approximately 80 nm and so interference effects are not observed until late on in the spin-coating process, when the film is thinner.

The interference effects observed for blends cast on silicon, were removed by changing the substrate from silicon to glass. Glass is significantly less reflective than silicon and so interference effects between the substrate and the surface of the thinning film are greatly reduced. The morphological evolution of the 55:45, 60:40, and 65:35 PFO:PS blends spun-cast onto glass are shown in Figure 4.4. The radially averaged Fourier transformed data (Figure 4.5) now exhibit no successive bright/dark bands at any point during the spinning process, indicating the technique is sensitive to composition at all points during the spin-coating process.

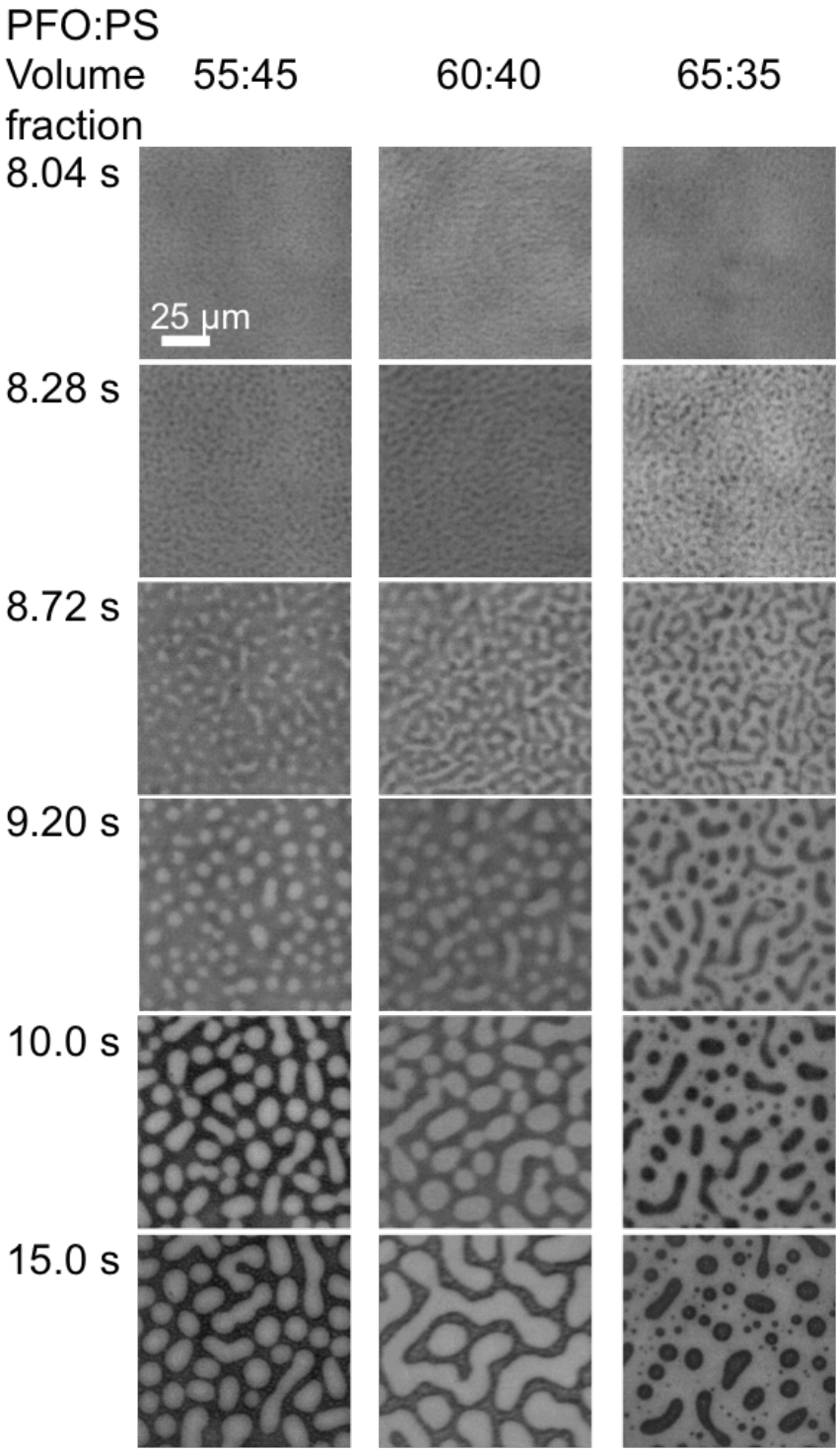

Figure 4.4. Direct observation of phase separation in a blends of PFO:PS (55:45, 60:40, 65:35) spun-cast (2 wt% at 1500 rpm) from *ortho*-xylene on glass; Stroboscopic fluorescence images at 8.04, 8.28, 8.72, 9.20, 10 & 15 s, respectively.

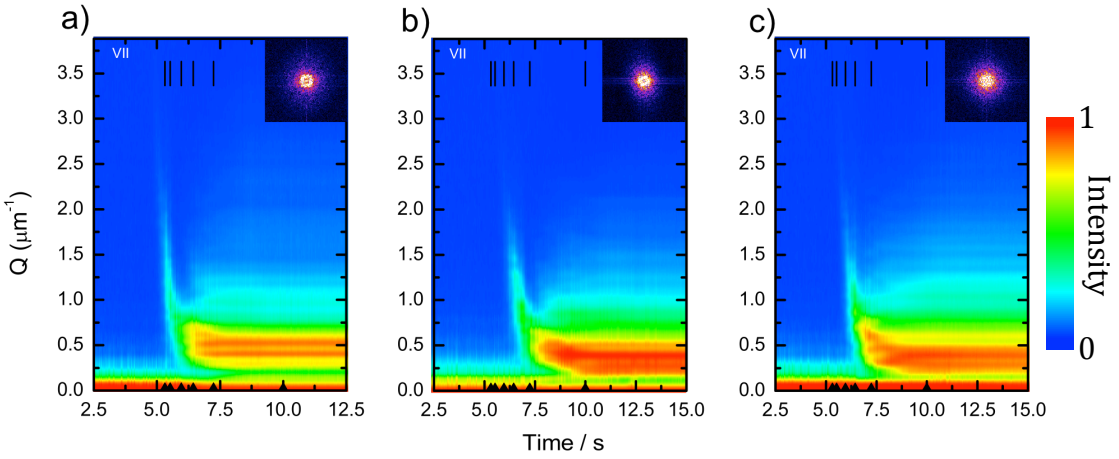

Figure 4.5. Intensity plots of the radial averaged Fourier transform for a selection of each *in situ* data series for PFO:PS blends spun-cast at 1500 rpm from *ortho*-xylene on glass at compositions of; a) 55:45, b) 60:40 and c) 65:35. The vertical lines correspond to times for images in Figure 4.4.

For blends spun-cast on glass the onset of phase separation was observed at an earlier point (~5.0 s) than blends spun-cast on silicon (~7.5 s). The stroboscopic fluorescence data shows that all blends form a bicontinuous morphology (Figure 4.4), which grows through Ostwald ripening (Figure 4.4) until an instability disrupts the bicontinuous morphology. The point where this occurs shows the same compositional dependence as observed for blends spun cast on silicon, occurring at 5.72, 6.00, and 6.40s respectively for 55:45, 60:40, and 65:35 for blends spun-cast on glass. The discrete islands of PFO formed in the 55:45 & 60:40 blends then proceed to grow through Ostwald ripening and coarsening, re-establishing interconnectivity (Figure 4.4 left and centre, respectively). As observed for blends spun-cast on silicon, for the blends spun-cast on glass the bicontinuous morphology is lost at a later point for the 65:35 blend and the PFO phase grows to form a matrix, whilst the PS phase shrinks (Figure 4.4 right), as

observed for the 65:35 blend spun on silicon. The radially average data (Figure 4.5) show the initial lengthscale of ~2.2 μm (Q = 2.8 ±0.5 μm^{-1}) grows through Ostwald ripening at a greater rate that observed for blends spun-cast on silicon.

The difference observed in the onset of phase separation and the rate of morphological development between samples spun on silicon and glass is attributed to the wetting characteristics of the two substrates. Glass is more hydrophilic than silicon. When the polymer solution is deposited on the substrate a greater degree of wetting will take place on glass, compared to silicon, leading to a initial film that is thinner, with a larger surface area, which will alter the initial dynamics of film thinning, triggering phase separation to occur at an earlier point due, to coupling between hydrodynamics and phase separation and increases the rate of morphological development.(5, 6)

With this insight of how morphological development proceeds in blends of PFO:PS we extended our approach to include real time FFT analysis of the acquired images. This has allowed us to precisely follow lengthscale development, facilitating real-time feedback over the spin-coating parameters and enabling directed phase separation. Through the use of feedback we have guided the process of phase separation to form a bicontinuous morphology, in blends that would not normally exhibit such a final morphology as in the case of the 65:35 blend.

This was achieved by applying a threshold to a high Q region in the radially averaged FFT data, which we have shown earlier (Figure 4.1), corresponded to a bicontinuous morphology. The occurrence of a peak in this high Q region triggered an increase in the rotation rate, to quench the polymer blend at a faster rate and

"freeze" morphological development before the interconnected morphology was disrupted.

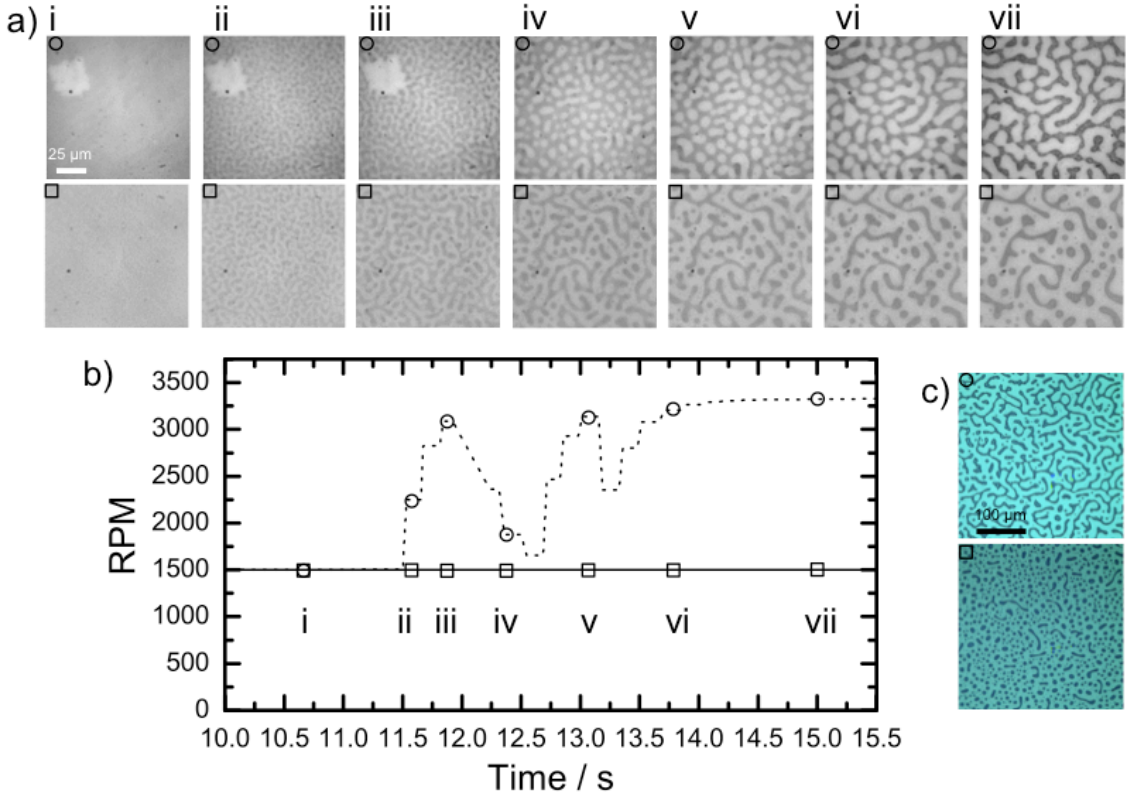

Figure 4.6. Direct observation of phase separation in blends of PFO:PS (65:35) (2 wt% at 1500 rpm) from *ortho*-xylene on silicon with (circle) and without (square) feedback. a; Stroboscopic fluorescence images at 10.60, 11.60, 11.80 12.40, 13.12 13.75 & 15.00 s.[c] b; radial speed in RPM as a function of time with (dotted) & without (solid) feedback. c; final (x20) fluorescence images.

[c] Data for 65:35 blend spun-cast without feedback has been offset in time to align with data of blend spun-cast with feedback. As time is not recorded by software for samples ran without feedback – time is inferred from frame number and radial speed.

Figure 4.6 shows *in situ* stroboscopic fluorescence data and the spin profiles for a 65:35 blend spun-cast on silicon and the corresponding spin profiles (Figure 4.6b) of blends spun with (Figure 4.6 - ○) and without (Figure 4.6 - □) feedback. An early bicontinuous morphology is observed for both blends at 10.6 s (Figure 4.6a i), which grows as previously observed. At 11.5 s, the lengthscale of the morphology triggers an increase in the rate of rotation from 1500 to 3000 rpm. Both films exhibit similar bicontinuous morphologies until 12.4 s (Figure 4.6 iii). After this point the higher rate of evaporation, caused by the higher rate of rotation in the feedback sample, triggered an instability, resulting in the formation of discrete islands of PFO within a continuous matrix of PS (Figure 4.6 iv ○). The averaged FFT of the resultant morphology did not exhibit a strong enough peak to trigger the higher rate of rotation, so the rate of rotation reduced to 1600 rpm.[d] The discrete islands of PFO then coarsened (Figure 4.6 iv-vi), as observed previously for the 60:40 blend (Figure 4.1 iv-vi), re-establishing a bicontinuous morphology. At 12.6 s feedback triggers an increase in the rate of rotation to 3000 rpm, leading to vitrification. In comparison the 65:35 blend spun without feedback exhibited a bicontinuous morphology that was lost as the PS domains shrank to a smaller size (Figure 4.6 v-vii □), losing their interconnectivity. The final *ex situ* fluorescence images (Figure 4.6 c) show that the 65:35 blend spun with feedback has a much greater degree of interconnectivity than the same blend spun at 1500 rpm.

[d] Due to the nature of the synchronisation between the motor, camera and LED changes to the rate of rotation lead to imaging of a different area about the centre of rotation.

4.3 Conclusions

We have observed that blends spun cast on either silicon or glass first form a bicontinuous morphology as expected from spinodal decomposition, which grows through Ostwald ripening. At a point in time depending upon composition and substrate, a decay of this lengthscale occurs, resulting in a break-up of the bicontinuous structure and the formation of a morphology comprising of distinct islands within a continuous matrix. The point at which the bicontinuous morphology broke up, shows compositional dependence and is likely to be caused by an interfacial instability. For the 60:40 blend a large degree of phase coarsening occurred, acting to re-establish an interconnected bicontinuous morphology. Whilst for the 55:45 blend the instability was triggered earlier, resulting in the formation of a smaller secondary lengthscale and for the 65:35 blend the instability was triggered later, resulting in the interconnected PS domains shrinking as the matrix of PFO grew. I have utilised this insight into how phase separation proceeds in blends of PFO:PS to obtain an interconnected morphology at a composition which ordinarily would not be interconnected. This was achieved through the use of real time FFT analysis of stroboscopic fluorescence images facilitating feedback over spin-coating parameters. This approach has allowed us to direct phase separation in order to achieve bicontinuous morphologies at a composition, which would not readily exhibit such interconnectivity.

The technique of stroboscopic fluorescence microscopy offers insight and understanding into previously unseen processes that take place during the spin coating of a polymer blend containing fluorescent and non-fluorescent polymers, and has allowed unprecedented control over the fast, non-equilibrium processes.

This technique could be further extended for the study of a wide range of non-fluorescent polymer systems, through doping a polymer with a suitable fluorophore.

4.4 References

1. Arias AC, Corcoran N, Banach M, Friend RH, MacKenzie JD, Huck WTS. Vertically segregated polymer-blend photovoltaic thin-film structures through surface-mediated solution processing: AIP; 2002. 1695-7 p.
2. Arias AC, MacKenzie JD, Stevenson R, Halls JJM, Inbasekaran M, Woo EP, et al. Photovoltaic performance and morphology of polyfluorene blends: A combined microscopic and photovoltaic investigation. Macromolecules. 2001;34(17):6005-13.
3. Chappell J, Lidzey DG, Jukes PC, Higgins AM, Thompson RL, O'Connor S, et al. Correlating structure with fluorescence emission in phase-separated conjugated-polymer blends. Nature Materials. 2003;2(9):616-21.
4. Cadby A, Dean R, Fox AM, Jones RAL, Lidzey DG. Mapping the Fluorescence Decay Lifetime of a Conjugated Polymer in a Phase-Separated Blend Using a Scanning Near-Field Optical Microscope. Nano Letters. 2005;5(11):2232-7.
5. Clarke N. Instabilities in thin-film binary mixtures. The European Physical Journal E. 2004;14(3):207-10.
6. Clarke N. Toward a Model for Pattern Formation in Ultrathin-Film Binary Mixtures. Macromolecules. 2005;38(16):6775-8.

Chapter 5. Effect of polydispersity

5.0 Introduction

Expanding on the work conducted in Chapter 4, I have utilised stroboscopic fluorescence microscopy to study the effect of polydispersity on phase separation. The majority of phase separation studies have focused on polymer systems possessing narrow molecular weight distributions. However, the majority of polymers employed in organic electronic devices are highly polydisperse, possessing broad molecular weight distributions, due to the synthetic routes employed, which is in stark contrast to the research done on such systems.

A number of theoretical studies have extended the Cahn-Hilliard theory of spinodal decomposition to allow for polydisperse components.(1, 2) Clarke showed that for polydisperse systems, the Q dependence of the growth rate of the dominant length scale of phase separation is commensurate with the behavior of monodisperse systems, and that for shallow quenches through the phase diagram, the early stages of spinodal decomposition are slower for more polydisperse polymers.(3) Mumby *et al*. derived an equation (Equation 1.19) for the predicted critical composition for a binary polydisperse system, where both components (*a* and *b*) are polydisperse, which is dependent upon M_w and M_z.(4)

In this chapter I will show the direct visualisation of the effect of polydispersity on morphological development in spin-coated polymer blends using stroboscopic fluorescence microscopy. Blends of poly(9,9'-dioctyl flourene) (PFO) with polystyrene (PS) of different polydispersities have been investigated.

5.1 Experimental

The technique of stroboscopic microscopy in an flouresence set-up was employed (as described in Section 2.2), comprising of an extra long working distance (ELWD) 60x objective, NA 0.7 (Nikon), UV illumination from a 360nm LED (Ledegin), a UV2A (Nikon) beam cube to separate the excitation and emission wavelengths, with an Andor iXON (897^{+}) detector, with a field of view of 132 x 132 μm.

Solutions of poly(9,9'-dioctylfluorene) (PFO) (supplied by Cambridge Display Technologies as CDTGreen003/22) M_n ~81,000 Da, M_w/M_n ~ 2.70 and polystyrenes (PS) with different polydispersities were provided by the Topham research group; M_n 58,800 Da, M_w/M_n 1.68; M_n 58,000 Da, M_w/M_n 1.8; M_n 56,000 Da, M_w/M_n 2.8. Solutions of PFO and PS were made up in *ortho*-xylene (Aldrich) at 2 wt% and stirred continuously for 24 h. They were mixed at the appropriate volume ratios prior to spin-casting. Silicon substrates (100) were cleaned in piranha solution (H_2SO_4 : H_2O_2) (1 : 1 v/v) for 6 h, followed by multiple rinsing with distilled water. Each substrate was placed on the chuck and the focusing was adjusted to "imperfections" on the surface. 20 μl of solution was dispensed onto the substrate and then spun at the designated spin speed, with data collected for 500 exposures, corresponding to 20 s at 1500 rpm.

5.2 Results and discussion

In situ stroboscopic fluorescence data for PFO:PS blends containing PS with different polydispersities (M_w/M_n = 1.68, 1.80 and 2.8, respectively), spun-cast at 1500 rpm, are shown in Figure 5.1 (Movie 5.1[a]), with the corresponding radial integrals of the fast Fourier transform (FFT) taken for each frame of the movies (Figure 5.2).

[a] Movie accompanying Figure 5.1 available at http://youtu.be/HtA7knJ9pOc.

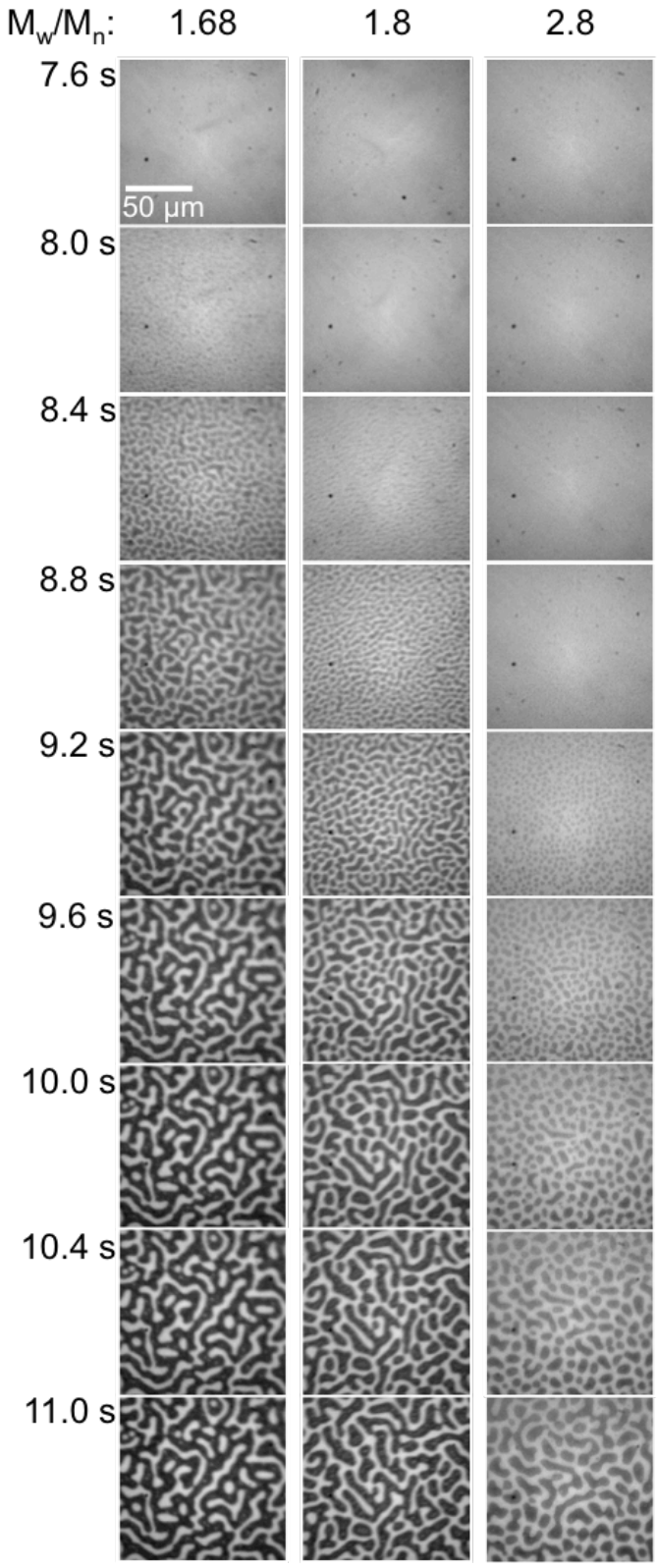

Figure 5.1. Direct observation of phase separation in blends of PFO:PS (3:7) spun-cast (2 wt% at 1500 rpm) from *ortho*-xylene, with (left) PS M_n = 58.8k, M_w/M_n = 1.68; (centre) PS M_n = 58.0k, M_w/M_n = 1.8; and (right) PS M_n = 56.8k, M_w/M_n = 2.8; showing sequences of stroboscopic fluorescence images.

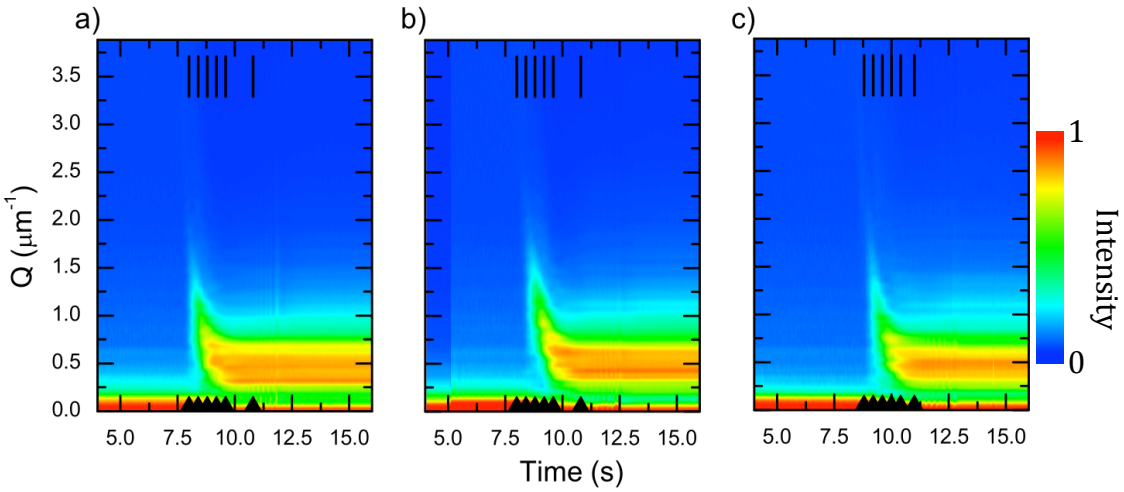

Figure 5.2. Direct observation of phase separation in blends of PFO:PS (3:7) spun-cast (2 wt% at 1500 rpm) from *ortho*-xylene, with (a) PS M_n = 58.8k, M_w/M_n = 1.68; (b) PS M_n = 58.0k, M_w/M_n = 1.8; and (c) PS M_n = 56.8k, M_w/M_n = 2.8; showing radially-averaged Fourier transform for the dynamic data.

The stroboscopic fluorescence data for the blend containing PS with the lowest polydispersity (M_w/M_n = 1.68) are shown in Figure 5.1 left, indicate that phase separation is initially occurs at 7.6 s. At the onset of phase separation a bicontinuous morphology is observed, which has a characteristic length scale of 2.28 μm (Q = 2.75 ±0.6 μm^{-1}). Between 8.0 and 10.8 s the length scale of this bicontinuous morphology rapidly increases from 3.1 to 12.6 μm, as coarsening and coalescence behaviour is observed as shown in Figure 5.2 a. Some smaller discrete islands of PFO are visible within the PS domains, indicative of secondary phase separation processes.

Data for the blend containing PS with a slightly high polydispersity (M_w/M_n = 1.8) (Figure 5.1 centre) show that the polymer behaves similarly to that of the blend with the lowest polydispersity PS, where a bicontinuous morphology is initially observed that subsequently coarsens and coalesces. However, the onset

of phase separation occurs at a later point in time, with structure first observable at 8.2 s.

The behaviour of the blend containing the highest polydispersity (M_w/M_n = 2.8) (Figure 5.1 right), is different to that of the lower polydispersity blends. Stroboscopic microscopy shows that the initial morphology comprises of a matrix of PFO (bright) with small discrete islands of PS (dark). The PS domains have an initial size of ~1.80 μm (Q = 3.5 ±0.6 μm^{-1}), growing to a size of 13.96 μm (Q = 0.45 ±0.1 μm^{-1}) as shown in Figure 5.2 c. At this point the domains begin to coalesce, resulting in the formation of fewer, larger domains. Using this direct imaging approach we are clearly able to identify the point at which domain coarsening begins to occur, in place of domain growth. At ~10.5 s the morphology strongly resembles the interconnected bicontinuous morphologies formed by the blends containing PS with polydispersities of 1.68 and 1.8, respectively. Phase separation in the blend containing PS with the highest polydispersity occurred at 8.9 s, much later than for the lower polydispersity blends.

Using Equation 1.19**,** the critical points of the 1.68, 1.8 and 2.8 blends were calculated as 0.456, 0.459 and 0.542, respectively. The observed difference in the initially observed morphology may be ascribed to the increasing polydispersity shifting the volume fraction of the two components away from the critical point, resulting in the morphology appearing more droplet-like, than bicontinuous.

In order to control morphological development of PFO:PS blends, bimodal PS blends were utilised, so that the critical point of the system could be tuned. PS (M_w/M_n = 1.8 & 2.8) was blended at weight ratios of 1:1 and 7:3, and stroboscopic data for these blends are shown in Figure 5.3. The data for the 1:1 blend (Figure 5.3 a) show that phase separation now initially proceeds via the formation

of a bicontinuous morphology (indicative of spinodal decomposition), whilst the data for the 7:3 blend (Figure 5.3 b) show that phase separation still initially proceeds via a nucleation and growth mechanism. Concomitantly, the onset of phase separation occurs earlier for the blends with higher loadings of the lower polydispersity PS. The final morphology of the 7:3 blend does not exhibit the same degree of interconnectivity as the pure 2.8 PS blend.

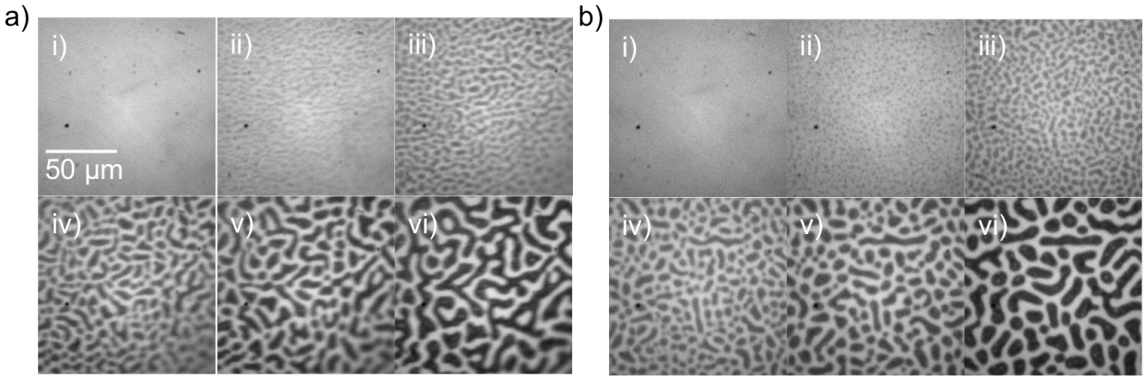

Figure 5.3. Direct observation of phase separation in blends of PFO:PS (3:7) spun-cast (2 wt% at 1500 rpm) from ortho-xylene, with PS (a) M_n = 58k:56k (1:1); (b) M_n = 58k:56k (3:7); showing sequences of stroboscopic fluorescence images at 8.4, 8.8, 9.2, 9.6, 10.0 and 11.2 s in (i) to (vi), respectively.

5.3 Conclusions

To summarise, we have observed the effect of polydispersity on phase separation for spin-coated blends of PFO:PS using the direct imaging technique of stroboscopic fluorescence microscopy. The results show that for low polydispersity systems the initial phase separated morphology is bicontinuous, indicative of spinodal decomposition. On the other hand, for the high polydispersity system, the initial morphology comprises of discrete islands of PS within a matrix of PFO, indicative of a nucleation and growth. The difference in the morphological development is attributed to a shift in the critical point of the phase diagram. We have further shown that through blending polymers of high and low

polydispersity, it is possible to shift behaviour from nucleation and growth to the spinodal regime. These findings are of particular relevance in the field of organic electronics, where the highly conjugated polymers employed are often highly polydisperse. Blending polymers of different polydispersities may offer a route to tuning the morphology of devices, or providing a way to make use of lower grade, higher polydispersity polymers that may not necessarily have been previously thought viable.

5.4 References

1. Schichtel TE, Binder K. Kinetics of Phase-Separation in Polydisperse Polymer Mixtures. Macromolecules. 1987;20(7):1671-81.
2. Huang C, Delacruz MO. The Early Stages of the Phase-Separation Dynamics in Polydisperse Polymer Blends. Macromolecules. 1994;27(15):4231-41.
3. Clarke N. Early stages of phase separation from polydisperse polymer mixtures. The European Physical Journal E. 2001;4(3):327-36.
4. Mumby SJ, Sher P, van Ruiten J. Liquid—liquid phase separation in blends of polydisperse linear and branched polyethylenes. Polymer. 1995;36(15):2921-7.

Chapter 6. Crystallisation

Parts of this chapter were published in:

Toolan, D. T. W., *et al*. "*In Situ* studies of Phase Separation and Crystallization Directed by Marangoni Instabilities during spin-coating". Advanced Materials 25 (48), 7033-3037 (2013), DOI: 10.1002/adma.201302657.

6.0 Introduction

The crystalline structure adopted by conjugated polymers employed in organic electronic devices effects their electronic and optoelectronic properties.(1) As discussed in Section 1.2.5 polymers are semi-crystalline as different portions along a chain are able to participate with different crystal nuclei of different polymers, prohibiting the formation of a perfect polymer crystal.(2) Polymer crystallisation proceeds through the formation of chain folded lamellae that are created through the straightening and packing of polymer chains. An optimum lamella thickness is observed owing to the balance between the entropic drive to reduce extensive chain straightening (which would produce thick crystals) and the energetic desire to minimise excessive interfacial energy and unfavorable interactions from surface folds.(3) To overcome unfavorable interactions lamellae are organised into spherulites that grow out from a central nucleus.(4)

In the case of bulk heterojunction (BHJ) organic photovoltaic devices, efficiency is related to the formation of a well-defined nanoscale interconnected phase-separated morphology with a high degree of crystallinity, facilitating the separation and movement of charges.(5) As such, furthering our understanding of how crystallisation proceeds during spin-coating and how it interacts with phase separation is an important goal.

The most commonly studied semi-crystalline polymer is poly(ethylene glycol) (PEG) via a variety of techniques such as quartz crystal microbalance,(6) differential scanning calorimetry,(7, 8) atomic force microscopy,(6, 9, 10) cross polarised optical microscopy(11-13) and x-ray scattering. Shi *et al* have conducted a number of studies investigating the interplay between crystallisation and phase

separation in blends of PEG and PMMA,(14-16) however, these studies have concerned phase separation and crystallisation in polymer melts, and as such are only two component binary systems, which do not show the rich variety of morphologies accessible through solution processing routes. The recent study by Chou *et al* that employed a combination of time resolved spectroscopic reflectometry and grazing incidence small and wide angle x-ray scattering to investigate the formation of spin-coated OPV active layers from solution reported, "importantly, the crystallisation and phase separation are found to go hand-in-hand from start to end".(17)

In this chapter I have studied the process of polymer crystallisation from solution during spin-coating for a model crystalline:amorphous blend, in order to further investigate the interplay between crystallisation and phase separation. The crystallisation of pure PEG was studied using stroboscopic microscopy, incorporating white light illumination with crossed polarisers (Section 2.3). The interplay between phase separation and crystallisation in the model system of PEG:PS, through performing cross-polarised and interferometric experiments in tandem. This approach has enabled me to directly observe the effect of polymer concentration and substrate acceleration on the crystallisation of PEG from solution and show that the crystallisation occurs very late on during the spin-coating process. We have observed that for blends of PEG:PS phase separation and crystallisation are completely independent processes. For all compositions, phase separation occurs early on, whilst crystallisation occurs much later in the spin-coating process, indicating that in the systems we have studied these two process clearly do not "go hand-in-hand from start to end". Depending upon composition and polymer molecular weight we observe a rich variety of different phase

separation behaviour, including nucleation and growth and spinodal decomposition. Additionally, we observe the formation of Bérnard cells and the effects of Marangoni-type instabilities on morphological development.

6.1 Experimental

The stroboscopic microscope in both crossed polarised and interferometric set-ups is described in Chapter 2. Poly(ethylene glycol) (PEG) (4 & 10k Da) (Aldrich) used as supplied, polystyrene (28k) was provided by the Topham research group. Solutions of PEG and polystyrene, where made up in chloroform (Aldrich) at 8 wt% and stirred continuously for 24 h. The solutions where then mixed at 7:3, 1:1 and 3:7 volume ratios prior to spin-casting. Silicon substrate (100) were cleaned in piranha solution (H_2SO_4 : H_2O_2) (1 : 1) for 6 h, followed by multiple rinsing with distilled water. Glass substrates (Fisher Scientific) were used as received. Each substrate was placed on the chuck and the focusing was adjusted to "imperfections" on the surface. 30 µl of solution was dispensed onto the substrate and then spun at the designated rpm, with data collected for 2000 exposures.

6.2 Results and discussion

6.2.1 Crystallisation of PEG

In this chapter I have investigated the effect of polymer concentration, molecular weight and composition on phase separation and crystallisation (for clarity, information on all blends studied in this chapter is shown in Table 6.1 below).

Table 6.1. Polymer blends studied

Polymer volume fraction			wt% Polymer
PEG (4K)	PEG (10k)	PS (28k)	
1	0	0	4
1	0	0	8
1	0	0	16
0	1	0	4
0	1	0	8
0	1	0	16
0.3	0	0.7	8
0.5	0	0.5	8
0.7	0	0.3	8
0	0.3	0.7	8

I have directly observed the effect of concentration on the crystallisation of 10k PEG spun-cast at 1500 rpm from chloroform (at 8 wt%) with a ramp time of 10s (Figure 6.1 (top)[a]). When the spin-coating process is imaged under crossed polarisers the images appear dark until the formation of a two nuclei at ~ 7.0 s, after which clear crystallisation fronts are observed as the spherulites grow. The final crystallised state is reached at ~ 13 s. From such a series of images I have been able to obtain the crystal radius,(12) as a function of time at varying polymer concentrations for 4k PEG (Figure 6.1 left) and 10k PEG (Figure 6.1 right).[b] For both 4k and 10k PEG as the concentration is increased the onset of crystallisation is delayed. It is apparent that the rate of crystallisation remains unaffected by these changes in concentration (as shown in Table 6.2), which is consistent with

[a] Associated movie available at http://youtu.be/cHMhDd4Gc18.

[b] The standard error was calculated from three separate experimental runs at each composition.

isothermal crystallisation.(18) These changes in the onset of crystallisation with concentration may be attributed to the differences in film thinning, with the spontaneous development of crystal nuclei only occurring when the polymer concentration becomes sufficiently high within the film.

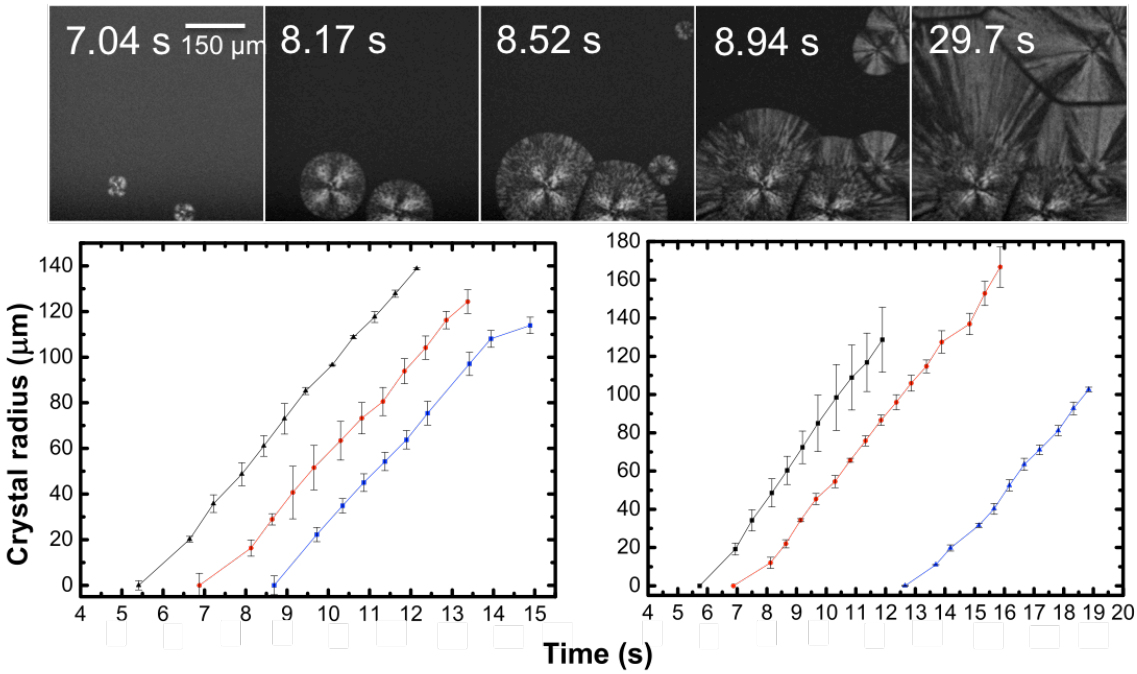

Figure 6.1. (top) Series of cross polarised stroboscopic images showing spherulite growth in 4k PEG, spun-cast at 8 wt%, at 1500 rpm with a ramp of 10s. (bottom) Spherulite radius as a function of time for 4k PEG (left) and 10k PEG (right) spun-cast from; 4 wt% (black), 8 wt% (red) and 16 wt% (blue) chloroform.

Table 6.2. Crystallisation rate for 4k and 10k PEG

Polymer	wt % Polymer	Ramp [s]	Crystallisation rate [μm s^{-1}]
4k PEG	4	10	21.5564
4k PEG	8	10	18.91897
4k PEG	16	10	17.24837
10k PEG	4	10	20.37628
10k PEG	8	10	19.74603
10k PEG	16	10	19.44474

6.2.2 Interplay between phase separation and crystallisation

To study the interplay between phase separation and crystallisation for blends of 4k and 10k PEG blended with 28k PS spun-cast from 8 wt% chloroform at compositions of 7:3, 1:1 and 3:7 (PEG:PS), *in situ* stroboscopic microscopy runs were performed with either near monochromatic or cross polarised illumination at each composition.

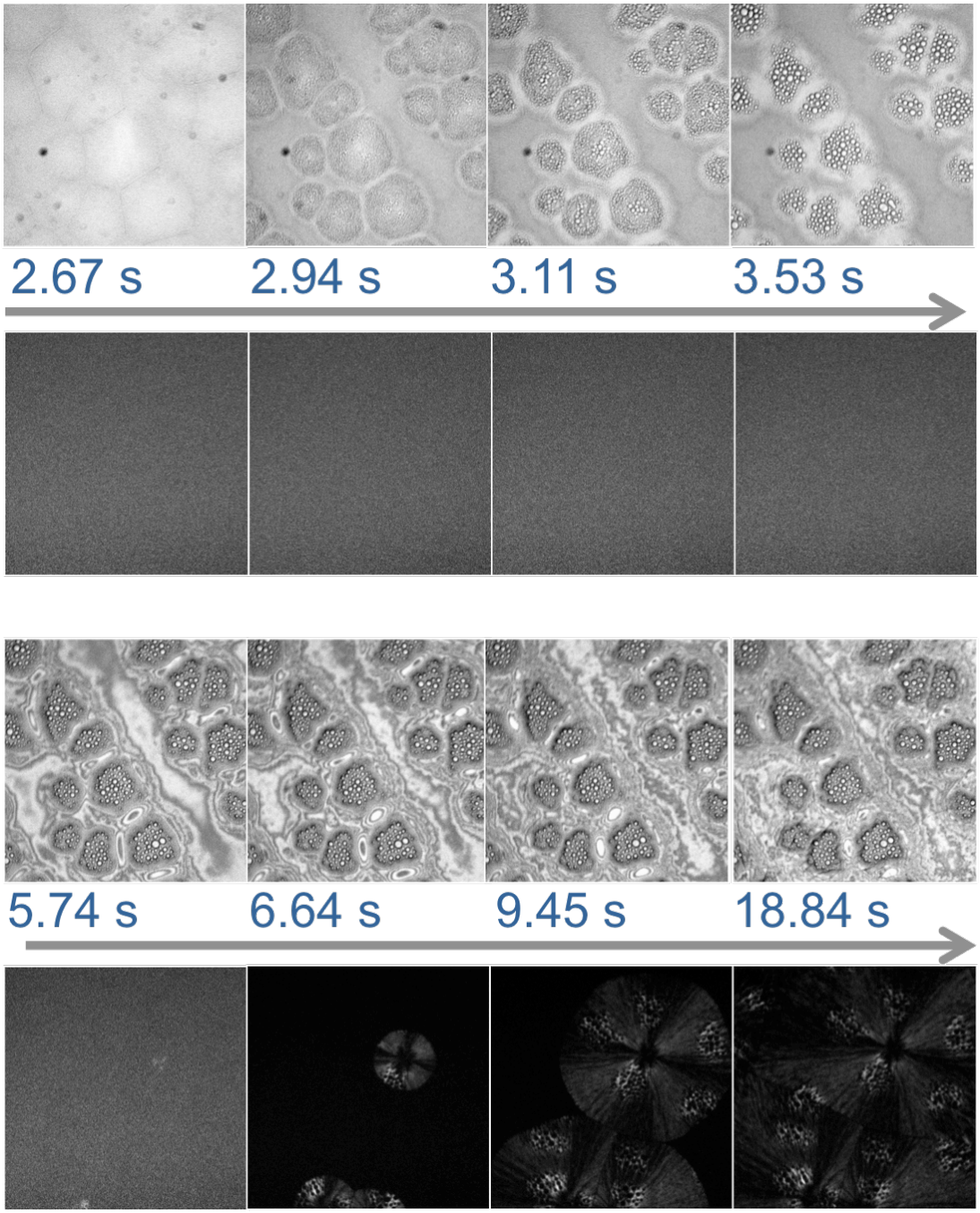

Figure 6.2. Direct observation of phase separation and crystallisation in blends of 4k PEG: 28k PS spun-cast from 8 wt% chloroform solution at 1500 rpm with a ramp of 10 s at composition of 7:3. Performed using either near monochromatic (top) or cross polarised illumination at each composition (bottom).

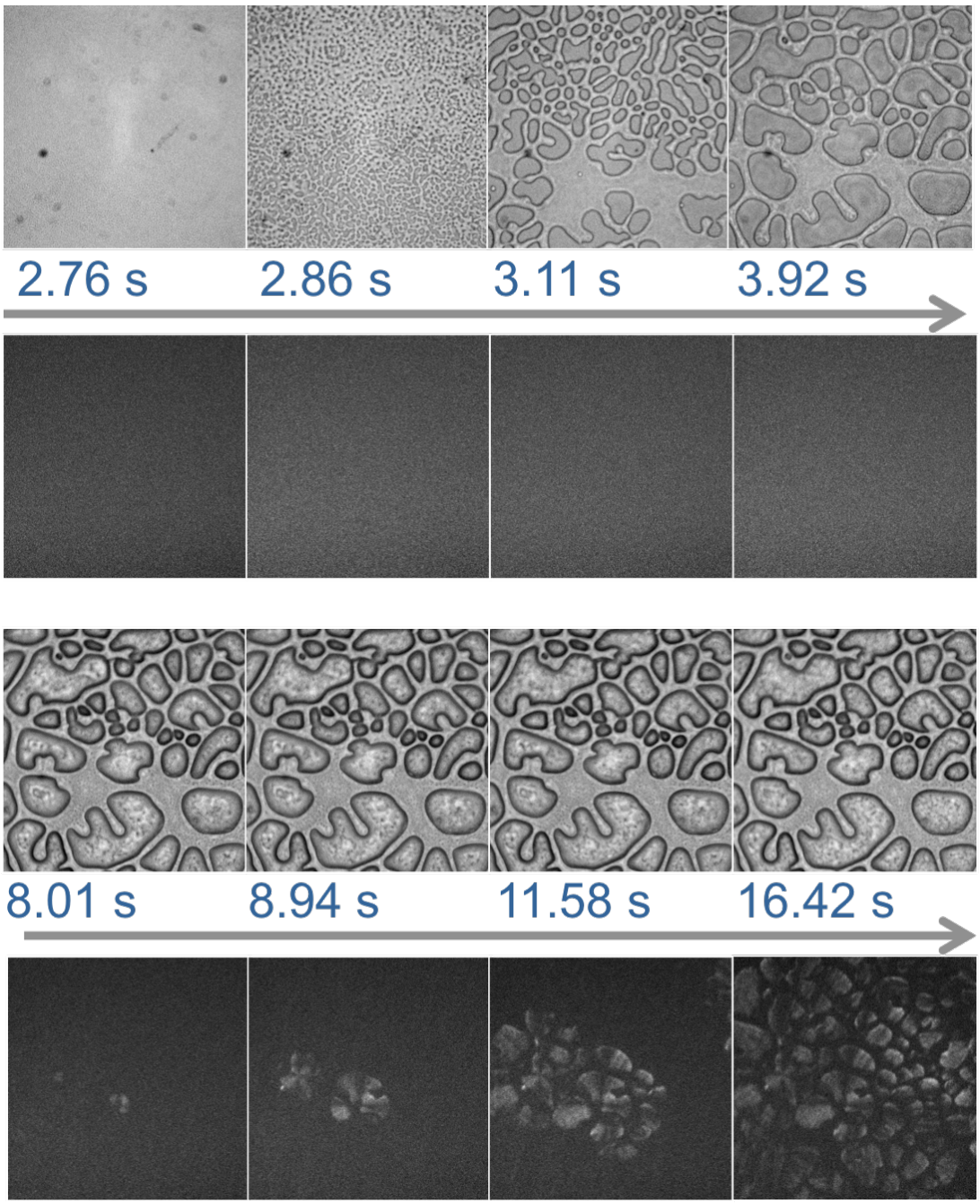

Figure 6.3. Direct observation of phase separation and crystallisation in blends of 4k PEG: 28k PS spun-cast from 8 wt% chloroform solution at 1500 rpm with a ramp of 10 s at composition of 1:1. Performed using either near monochromatic (top) or cross polarised illumination at each composition (bottom).

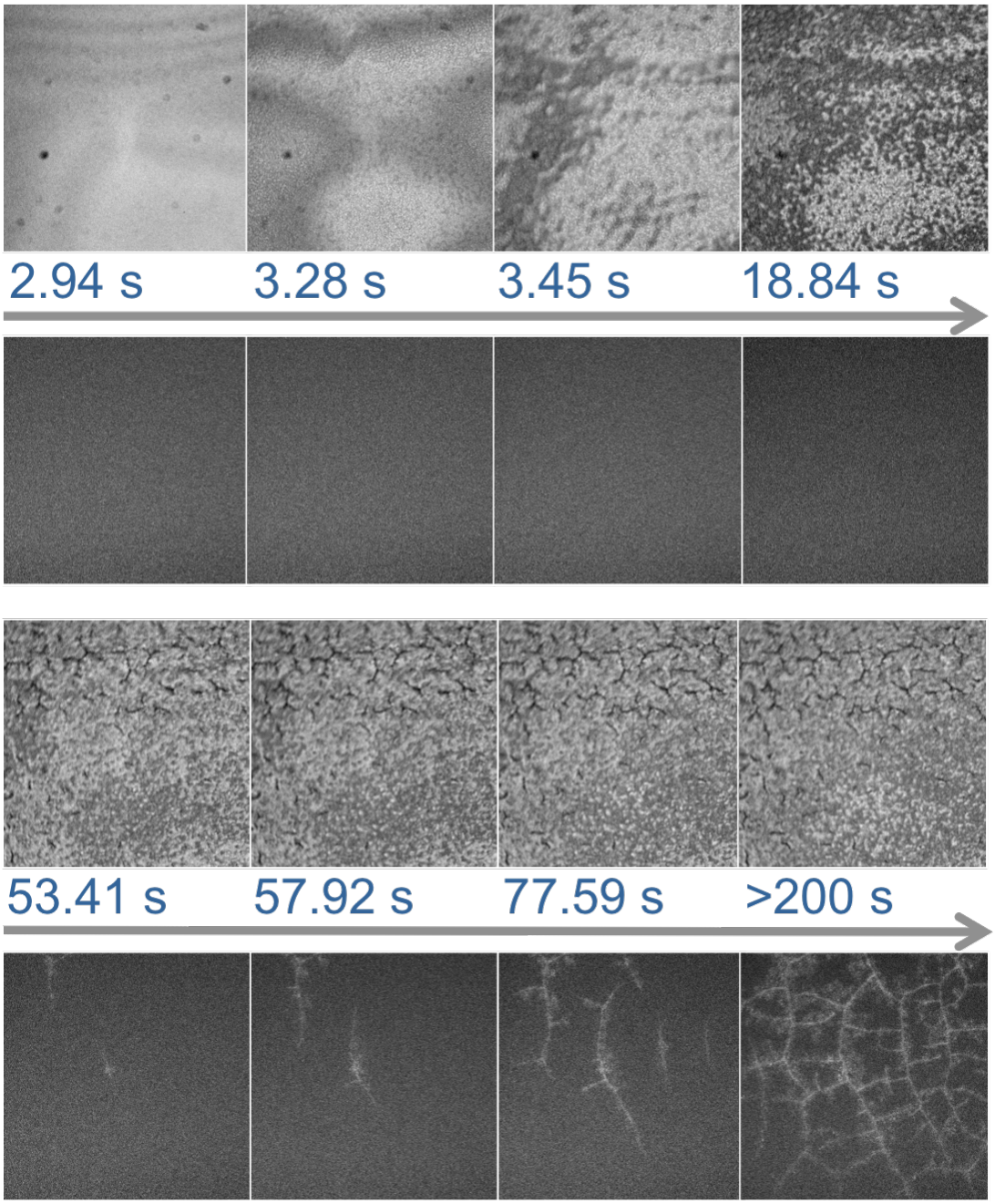

Figure 6.4. Direct observation of phase separation and crystallisation in blends of 4k PEG: 28k PS spun-cast from 8 wt% chloroform solution at 1500 rpm with a ramp of 10 s at composition of 3:7. Performed using either near monochromatic (top) or cross polarised illumination at each composition (bottom).

Figure 6.3-6.5 shows a series stroboscopic and cross polarised images for PEG(4K):PS(28K) 8 wt% in chloroform spun-cast at 1500 rpm with a ramp of 10 s for blends with volume ratios of PEG:PS at 7:3 (Figure 6.2), 1:1(Figure 6.3) and 3:7 (Figure 6.4). Stroboscopic interferometry frames (Figure 6.3) for the 7:3 blend

show that at 2.67 s relatively large (~ 100 μm) hexagonal & pentagonal cells form. Such pattern formation occurs readily in nature and is commonly referred to as Bérnard cells,(19) with such behavior indicative of Marangoni effects. Phase separation proceeds to take place at 2.94 s, within the Bérnard cells through a nucleation & growth mechanism, producing discrete islands of one phase that subsequently coarsen (2.94 - 3.53 s), resulting in the formation of larger islands within the cells. At 5.74 s the phase-separated morphology appears predominantly fixed. The cross-polarised data confirms that no crystallisation of the PEG domains occurred during the phase separation process. After 5.74 s the cross-polarised data show that crystallisation proceeds through the growth of a spherulitic crystal front, until all of the PEG domains appear crystallised at ~18 s.

Data for the 1:1 blends (Figure 6.3) show that an initial bicontinuous phase separated morphology is formed at 2.76 s that subsequently grows and coarsens (2.76 - 3.92 s). The phase separated morphology appears mostly fixed at 3.92 s, earlier than the PEG-rich (7:3) blend. Crystallisation is first observed at 8.01 s, and as with the previous blend the crystallisation front grows until all of the PEG domains appear crystallised at 16.42 s.

Data for the PS-rich (3:7) blends (Figure 6.4) show a much more disordered morphology with no common length scale. Crystallisation is first visible at ~19 s, and unlike the 7:3 & 1:1 blends, dendrite type crystals form in favour of spherulites. Crystallisation occurs significantly slower in the 3:7 blend taking > 200 s to form the final morphology. Dendritic crystal growth occurs in the 3:7 blend due to the lower PEG fraction,(20) and the large crystallisation time is indicative of a diffusion-limited crystallisation process. The high viscosity observed in the PEG solutions is a result of the dipole-dipole interactions between the PEG

chains. As a result, blends richer in PEG exhibit higher viscosities and so for solutions richer in PEG, diffusion is reduced and film thinning occurs the slowest. The Marangoni effect is triggered when solvent evaporation at the surface occurs faster than diffusion of solvent through the bulk. We attribute the formation of the observed Bérnard cells to the higher viscosity of the 7:3 blend, creating a thick, solvent rich film, giving rise to the observed Marangoni instabilities.

Figure 6.6-6.8 shows a series stroboscopic and cross polarised images for PEG(10K):PS(28K) in 8 wt% chloroform spun-cast at 1500 rpm with a ramp of 10 s for blends with ratios of PEG:PS; 7:3 (Figure 6.5), 1:1(Figure 6.6) and 3:7(Figure 6.7).

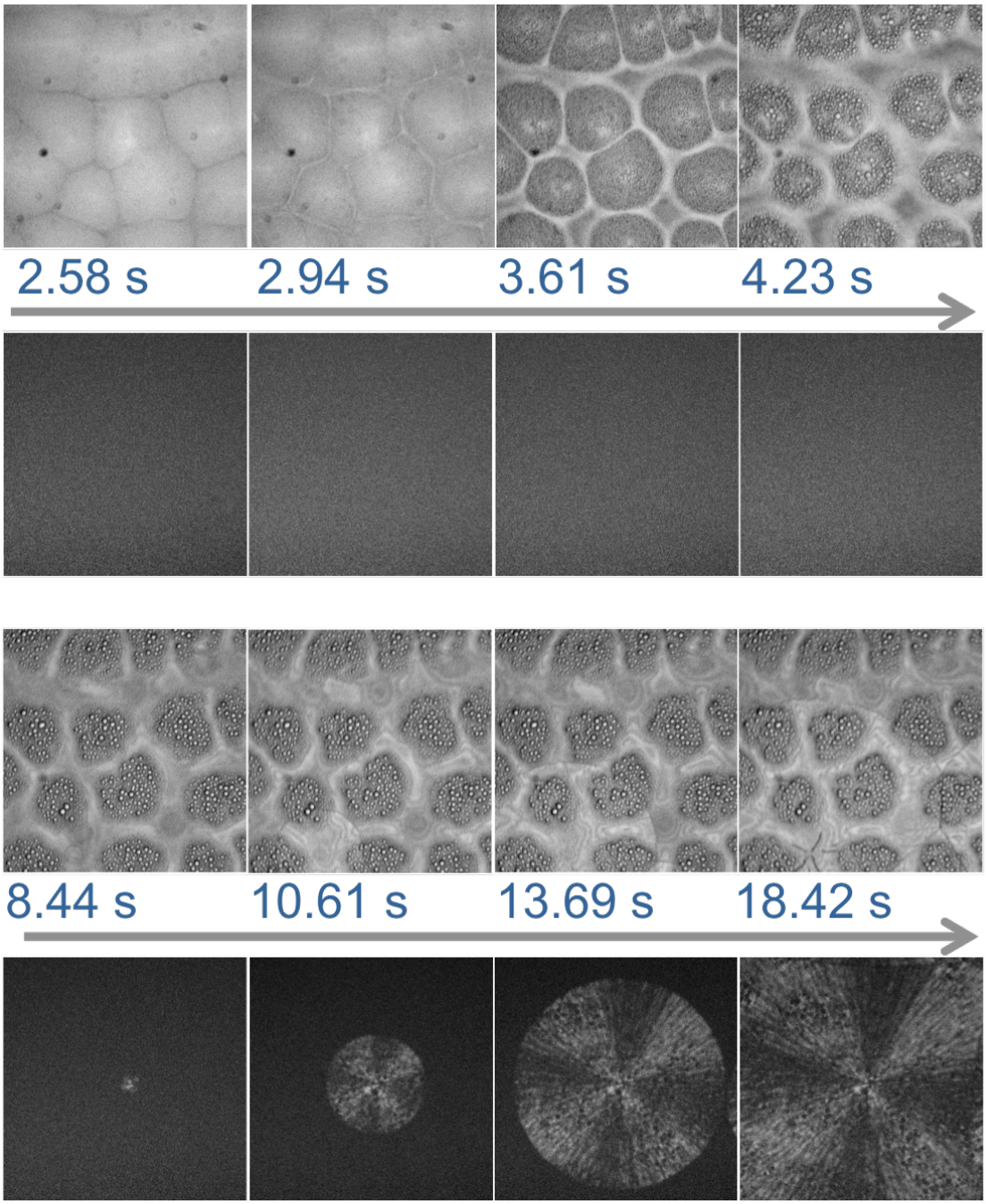

Figure 6.5. Direct observation of phase separation and crystallisation in blends of 10k PEG: 28k PS spun-cast from 8 wt% chloroform solution at 1500 rpm with a ramp of 10 s at a composition of 7:3. Performed using either near monochromatic (top) or cross polarised illumination at each composition (bottom).

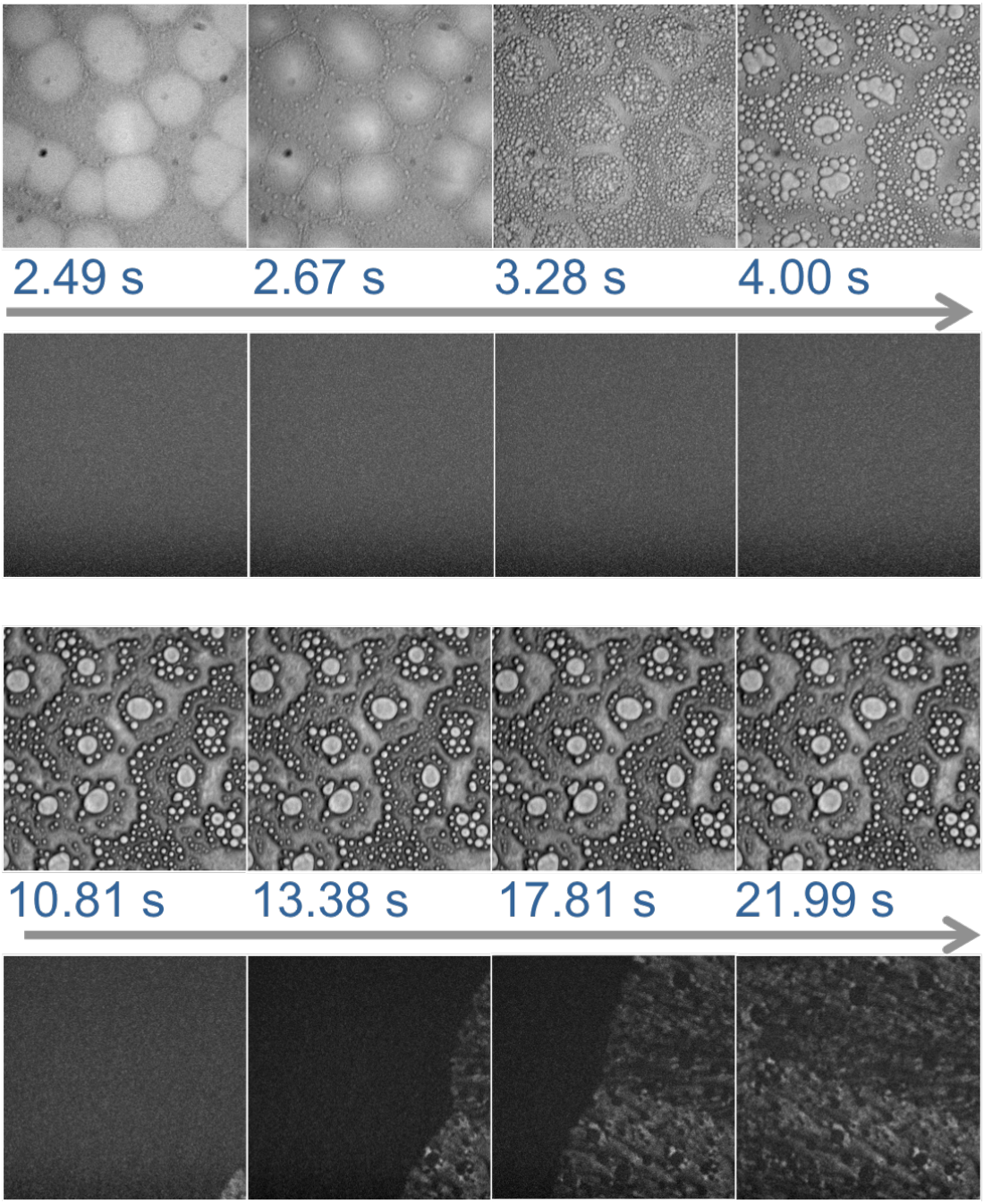

Figure 6.6. Direct observation of phase separation and crystallisation in blends of 10k PEG: 28k PS spun-cast from 8 wt% chloroform solution at 1500 rpm with a ramp of 10 s at a composition of 1:1 Performed using either near monochromatic (top) or cross polarised illumination at each composition (bottom).

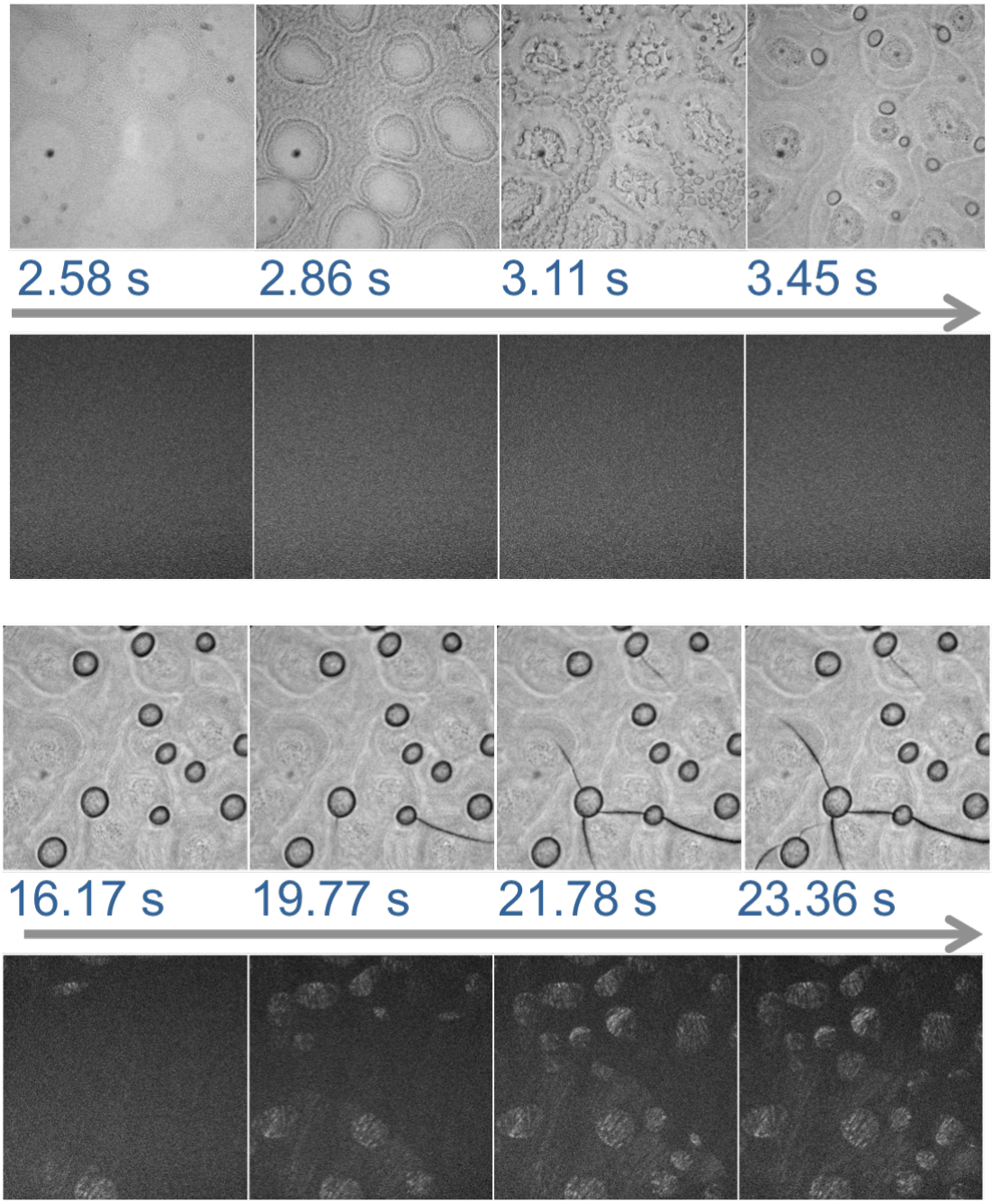

Figure 6.7. Direct observation of phase separation and crystallisation in blends of 10k PEG: 28k PS spun-cast from 8 wt% chloroform solution at 1500 rpm with a ramp of 10 s at a composition of 1:1 Performed using either near monochromatic (top) or cross polarised illumination at each composition (bottom).

Data for the 10k PEG:PS blends shows that Bérnard cells form through the Marangoni effect, at all compositions (7:3, 1:1 & 3:7), due to the higher viscosity of these blends containing higher molecular weight PEG. For the 7:3 blend phase separation takes place similarly to that observed in the PEG(4K):PS(28k) 7:3

blend, where the growth of nucleated domains appears to be directed to take place within the Bérnard cells and domain coarsening/coalescence occurs between 3.61 s to 8.44 s, leading to the formation of discrete islands of PS. Growth of the spherulitic crystal structure is first observed at 8.44 s, by the appearance of a single nucleus in the center of the image, the PEG phase appears fully crystallised within ~18 s. The Bérnard cells formed in the PEG(10K):PS(28k) 1:1 and 3:7 blends are not completely interconnected as observed in the 4k and 10k 7:3 blends. Instead, the cells are more spherical (due to less interfacial interactions between adjacent cells) and are within a matrix of the two polymers, which are undergoing phase separation. The data for the PEG(10K):PS(28k) 1:1 blend (Figure 6.6) show that at 2.67 s nucleated domains are most prominent at the interface of the Bérnard cells. At 3.28 s phase separation occurs within the Bérnard cells, resulting in the formation of nucleated islands. Despite phase separation occurring later within the Bérnard cells, phase separation appears to progress much more rapidly inside of the cells (compared to outside) and is apparent by the fact that at 4.00 s the domains within the Bérnard cells have undergone extended coarsening/coalescence. Domain growth then proceeds similarly for all domains until the final phase separated morphology is fixed at ~10.00 s and is characterised by nucleated domains of PS with two different length scales (~5 & ~30 μm), where the larger of these length scales is separated by a large PEG phase. Crystallisation of the PEG phase was first visible at 10.61 s and the morphology appears fully crystallised by 21.99 s.

Phase separation in the PEG(10K):PS(28k) 3:7 blend occurs similarly to the PEG(10K):PS(28k) 1:1 blend (Figure 6.7), however, initial phase separation outside of the Bérnard cells at 2.58 s appears to take place through spinodal

decomposition (as opposed to nucleation & growth), forming a bicontinuous morphology. At 2.86 s, phase separation begins to take place within the Bérnard cells, occurring from the interface towards the centre of the cell (leaving a region in the centre of the cell that has not undergone phase separation). By 3.11 s, a significant degree of domain coarsening/coalescence results in the loss of the bicontinuous morphology outside of the Bérnard cells, discrete islands within a thin matrix of another phase forming, whilst, within the Bérnard cells a significant degree of phase separation occurs. Although, this initial morphology has a large number of features at 3.45 s, the majority of this early complex morphology is lost, instead there are only a few nucleated domains (~40 μm). Crystallisation is first observed at 16.17 s, with the growth of spherulitic crystallites, which grow to dominate the whole of the morphology by 23.36 s. This behavior is very different to that observed in the PEG(4K):PS(28k) 3:7 blend, where dendrite crystal growth was observed due to the low PEG content. As crystal growth occurs across the whole morphology for the PEG(10K):PS(28k) 3:7 blend, we attribute this to self-stratification, triggered by a Marangoni-type instability, resulting in distinct PS and PEG layers, stacked on top of each of parallel to the plane of the substrate. Such a morphology would appear completely crystalline under cross-polarises, despite the low PEG content.

The behaviour of the PEG(4K):PS(28k) is different to the PEG(10k):PS(28k) blends due to the increased blend viscosity in the 10k system leading to the occurrence of more Marangoni-induced effects, which either directs phase separation or at some compositions leads to an instability in selected regions, altering the course through the phase diagram.

6.3 Conclusions

This work has provided new insight into spin coating and the roles that phase separation, crystallisation and the Marangoni effect plays in governing morphological development in polymer blends comprising of semi-crystalline and amorphous components. The recently presented data by Chou *et al* suggesting that "phase separation and crystallsation go hand in hand", is clearly not true for this system. We attribute the difference between these observations to the difference in the mobility of the crystallisable polymers investigated. P3HT has a stiff, conjugated polymer backbone that is significantly more rigid than the PEG studied here. Consequently, P3HT is likely to crystallise earlier on in the spin-coating process than PEG.

This study indicates that in a different polymer blend system phase separation and crystallisation occur independently and we demonstrate through appropriate control over spin-coating parameters the point at which crystallisation occurs. We have been able to directly observe the Marangoni effect and the formation of Bérnard cells, which lead to the formation of different morphologies to those that would be formed from either standard nucleation and growth or spinodal decomposition mechanisms of phase separation. These results offer important insights into the complex nature of the spin-coating of polymer blends.

6.4 References

1. Geoghegan M, Hadziioannou G. Polymer Electronics: Oxford University Press; 2013.
2. Muthukumar M. Commentary on theories of polymer crystallization. European Physical Journal E. 2000;3(2):199-202.
3. Jones RAL. Soft condensed matter: Oxford University Press; 2002.

4. Gránásy L, Pusztai T, Tegze G, Warren JA, Douglas JF. Growth and form of spherulites. Physical Review E. 2005;72(1):011605.
5. Brabec CJ, Heeney M, McCulloch I, Nelson J. Influence of blend microstructure on bulk heterojunction organic photovoltaic performance. Chemical Society Reviews. 2011;40(3):1185-99.
6. Mellbring O, Oiseth SK, Krozer A, Lausmaa J, Hjertberg T. Spin coating and characterization of thin high-density polyethylene films. Macromolecules. 2001;34(21):7496-503.
7. Long Y, Shanks RA, Stachurski ZH. Kinetics of Polymer Crystallization. Progress in Polymer Science. 1995;20(4):651-701.
8. Galeski A, Bartczak Z, Pracella M. Spherulite Nucleation in Polypropylene Blends with Low-Density Polyethylene. Polymer. 1984;25(9):1323-6.
9. Schönherr H, Frank CW. Ultrathin films of poly (ethylene oxides) on oxidized silicon. 1. Spectroscopic characterization of film structure and crystallization kinetics. Macromolecules. 2003;36(4):1188-98.
10. Schönherr H, Frank CW. Ultrathin films of poly (ethylene oxides) on oxidized silicon. 2. In situ study of crystallization and melting by hot stage AFM. Macromolecules. 2003;36(4):1199-208.
11. Dalnoki-Veress K, Forrest JA, Massa MV, Pratt A, Williams A. Crystal growth rate in ultrathin films of poly(ethylene oxide). Journal of Polymer Science Part B-Polymer Physics. 2001;39(21):2615-21.
12. Massa MV, Dalnoki-Veress K, Forrest J. Crystallization kinetics and crystal morphology in thin poly (ethylene oxide) films. The European Physical Journal E: Soft Matter and Biological Physics. 2003;11(2):191-8.
13. Maclaine JQG, Booth C. Effect of Molecular-Weight on Spherulite Growth-Rates of High Molecular-Weight Poly(Ethylene Oxide) Fractions. Polymer. 1975;16(3):191-5.
14. Shi WC, Yang J, Zhang Y, Luo J, Liang YR, Han CC. Lamellar Orientation Inversion under Dynamic Interplay between Crystallization and Phase Separation. Macromolecules. 2012;45(2):941-50.
15. Shi WC, Xie XM, Han CC. Frustrated Crystallization in the Coupled Viscoelastic Phase Separation. Macromolecules. 2012;45(20):8336-46.
16. Shi WC, Chen FH, Zhang Y, Han CC. Viscoelastic Phase Separation and Interface Assisted Crystallization in a Highly Immiscible iPP/PMMA Blend. Acs Macro Letters. 2012;1(8):1086-9.
17. Chou KW, Yan B, Li R, Li EQ, Zhao K, Anjum DH, et al. Spin-cast bulk heterojunction solar cells: a dynamical investigation. Adv Mater. 2013;25(13):1923-9.
18. Yang J, McCoy BJ, Madras G. Temperature effects for isothermal polymer crystallization kinetics. The Journal of Chemical Physics. 2005;122(24):244905-8.
19. Ball P. The self-made tapestry: pattern formation in nature: Oxford Univ. Press, Oxford.
20. Okerberg BC, Marand H. Crystal morphologies in thin films of PEO/PMMA blends. Journal of Materials Science. 2007;42(12):4521-9.

Chapter 7. Colloidal Crystallisation

Parts of this chapter were published in:

Toolan, D. T. W., *et al*. "*On the mechanisms of colloidal self-assembly during spin-coating*". Soft Matter (2014), DOI: 10.1039/C4SM01711K.

7.0 Introduction

So far I have investigated self-assembly processes that occur during the spin-coating of polymer solutions, motivated by applications of polymer blends in organic electronics. The self-organisation of colloidal dispersions is an important phenomena, influencing processes as varied as the formation of dense ring-like deposits when coffee is spilled on a surface(1) and the formation of highly ordered two and three dimensional crystalline structures known as colloidal crystals, which have potential applications as photonic band-gap materials.(2) One of the main obstacles to exploiting these exciting materials is developing and understanding fabrication strategies that allow for fine control over the complex self-assembly processes that occur, such that large, defect free colloidal crystals may be obtained, via an industrially scalable manufacturing methods.

Spin-coating has been demonstrated as a facile method for the production of colloidal crystals.(3-8) As with the spin-coating of polymer blends there are a large number of parameters that affect the final morphology of spin-coated colloidal crystals, which include; viscosity, concentration, volatility, particle size, particle size distribution, Péclet number, rotation rate, acceleration rate and hold times.(4, 5, 7, 9-11) Due to this large parameter space and the rapid rotating sample we still do not fully understand how colloidal crystallisation proceeds during spin-coating.

Guiliani *et al* utilised high speed imaging to study symmetry transitions that occur during the spin-coating of silica particles (~460 nm) from methyl ethyl ketone (MEK) and acetone, where transitions from six-fold to four-fold and back to six-fold symmetries where observed, corresponding to either hexagonal (six-fold)

or square (four-fold) arrangements of particles in the substrate plane.(12) A drawback of this approach is that as these symmetries arise as a consequence of ordering and it is therefore not possible to directly ascertain the absolute mechanism through which ordering proceeded as observations are made in a scattering geometry and thus are based in reciprocal space.

There are numerous factors that affect structure formation of spin-coated colloidal crystals which may be described as solution properties and spin-coating parameters. Solution properties include particle size, size distribution, dispersant (volatility, viscosity), dispersant mixture (often dispersant mixtures are employed to tune properties such as solvent evaporation rate profiles) and the particle concentration.(3-5) Spin-coating parameters include the rotation and acceleration rates, which influence how the colloidal mixture is spread and subsequently dries.(7, 11)

In this chapter I show the direct observation of the ordering of 5 μm polystyrene colloidal dispersions during spin-coating to form highly ordered colloidal crystals. As discussed in Section 1.2.5 the self-organisation of colloidal dispersions has been observed as a consequence of; volume fraction, capillary forces and shear forces. (13-17) Importantly it is possible to observe a variety of different mechanisms by which ordering proceeds and to what extent these different processes control both intermediate and final morphologies of colloidal crystals.

7.1 Experimental

The technique of stroboscopic microscopy was employed (as described in Section 2.1) in a "pseudo transmission" geometry, whereby the sample was mounted on a transparent platter and illuminated by three LED's positioned as close to normal incidence as possible. A small DC motor acts as a spin-coater, which is mounted directly under a 40× objective (Nikon CFI S Plan Fluor ELWD 40X, NA 0.6). The sample was illuminated by 50 μs pulses of white light from three white LEDs (Cree X-Lamp, XP-G2, cool white). An Andor iXON (897+) was used, with a field of view of 464 × 464 μm when used in conjunction with the ELWD ×40 objective.

Micrometer-sized PS particles, with a number-average diameter of 5.16 μm and a polydispersity of 1.01 (determined by SEM) were purchased from Microbeads, Norway. The micrometer-sized polymer particles are stabilised with anionic sodium dodecyl sulfate surfactant in combination with a cellulosic stabiliser.

Glass microscope cover slips where utilised as the substrate and where used as supplied. Each substrate was placed on a transparent perspex chuck (15mm Ø, 10mm thick). 50 μl of the colloidal dispersion was dispensed onto the substrate and then spun at 1250 rpm, with data collected for 1000 exposures, corresponding to 48 s.

7.2 Results and discussion

Figures 7.1 – 7.3 show a series of stroboscopic microscopy images (along with corresponding reciprocal space Fast Fourier transforms) taken during spin-coating

of colloidal dispersions of 5 μm polystyrene particles in water at 1250 rpm, at concentrations of 25, 35 and 45 wt%, respectively.

The stroboscopic data for the 25 wt% solution (Figure 7.1, accompanying movie http://youtu.be/PWJNqLlV9pA) shows that initially, the solution and particles flow towards the bottom left of the image until ~4.8 s. During this initial flow stage the particles move in clusters. The reciprocal space FFT images reveal a diffuse ring,[a] indicating that the particles within these clusters are arranged loosely and randomly and do not posses the high degree of order, characteristic of crystalline ordering. We ascribe this initial radial flow of the particles to shear thinning of both components of the colloidal dispersion. Between ~5 – 8 s, the particles then move towards the top of the image, this change in the direction of particle flow arises from a transition from shear thinning to evaporative thinning. Shear forces act as a result of the rotation of the sample and thus the direction of such forces is fixed, and away from the center of rotation. The change in the direction of the forces acting upon the colloidal solution gives further evidence to the change in the origin of the forces dominating colloid flow and consequent ordering. At 10.1 s, the particles begin to order due to capillary effects, where an ordered monolayer of regularly close packed particles forms due to the random appearance of holes in the wetting film, capillary forces subsequently force the particles to be displaced along the drying fronts as the wetting film recedes. The observation of the growth of such drying fronts as the film evaporates is consistent with observations of Elbaum and Lipson, who studied the evaporation of water on freshly cleaved mica.(18)

The morphology becomes fixed at ~16s, comprising of highly crystalline regions containing large open voids. The FFT of the final structure shows a large

number of bright spots at uniform distance from the center and indicative of a final polycrystalline film.

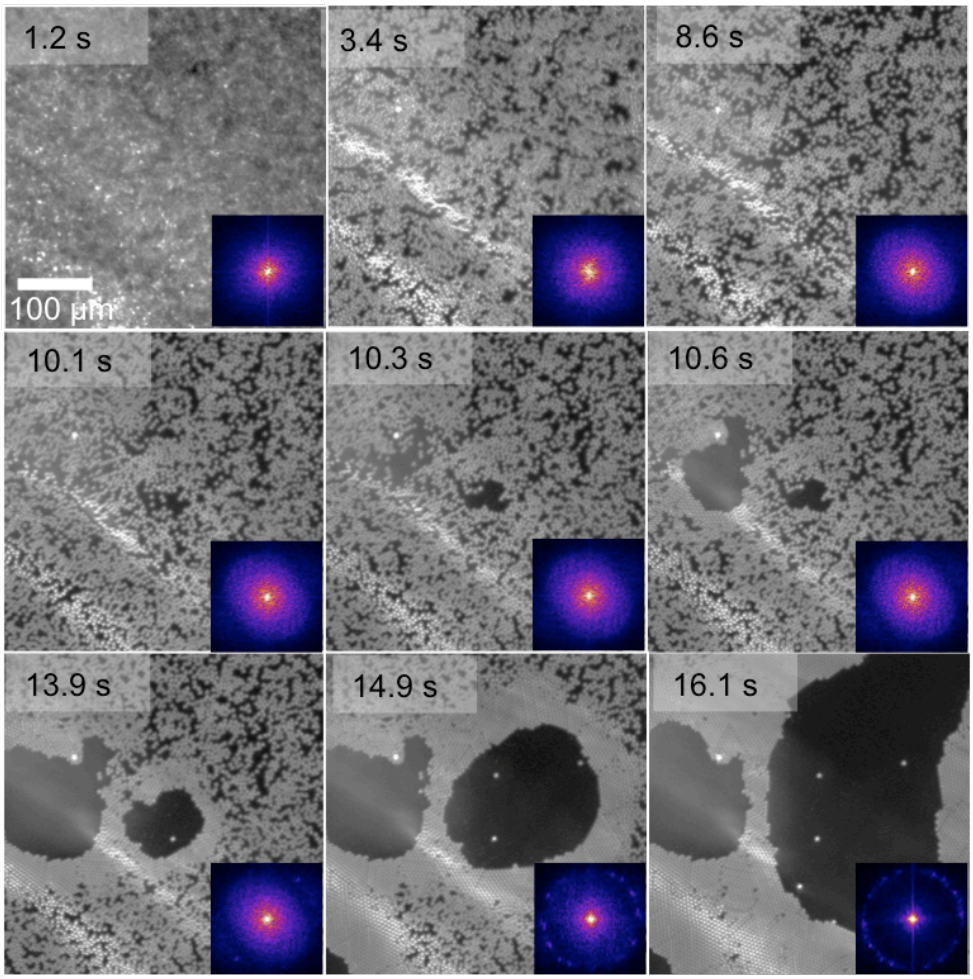

Figure 7.1. Series of stroboscopic microscopy images (with corresponding FFTs) for a 25 wt% colloidal dispersion in water spun-cast at 1250 rpm.

Figure 7.2, (accompanying movie http://youtu.be/u0pTz6p0d08) shows the structural development of the 35 wt% colloidal dispersion, which initially behaves in a similar manner to the 25 wt% dispersion, with directional flow occurring towards the bottom right of the image due to shear forces.[a] However at ~8 s, the

[a] The direction of flow is different between the 25 and 35 wt% samples and is related to the synchronisation between the motor and the illumination source,

FFT image reveals the onset of weak 6-fold symmetry, consistent with regular close packing that is also highly visible in the real space images. The onset of this symmetry appears to coincide with the shift from shear to evaporative thinning. During this evaporative thinning where the dispersant is being removed from the system, the particle concentration increases. Ordering occurs in order to maximise the packing of the particles resulting in the formation of a more ordered morphology (8 – 20 s), the evolution of which is highly apparent in both the real space and reciprocal space images. The FFTs show that despite the high degree of crystallinity, the structure is polycrystalline. After 20 s, the film thins further and voids form in the wetting film, resulting in capillary induced ordering, occurring due to incomplete particle coverage.

The 45 wt% (Figure 7.3) dispersion exhibits regular close packed structures at ~ 2 s, which are highly apparent in both the real and reciprocal space images (occurring significantly earlier than the in 35 wt% solution), during the shear thinning stage, which stops at approximately 8 s as evaporative thinning begins to dominate. During this thinning stage a large degree of re-organisation of the colloids occurs. The 45 wt% dispersion forms ordered structures earlier on in the thinning process due to the high initial concentration of colloid particles, making regular close packing becomes favorable to arrange the greater number of colloid particles. The morphology becomes fixed at ~15 s and after this we observe a drying front sweep across the film as the last of the dispersant evaporates. In this case there is an excess of particles for complete surface coverage and so a

---

which has three possible positions and therefore three different orientations about the center of rotation.

multilayer is formed (as opposed to the monolayers formed by the 25 and 35 wt% solutions). The final structure formed is a highly crystalline, multilayer colloidal crystal containing both HCP and FCC regions, with small crystalline regions separated by defects.

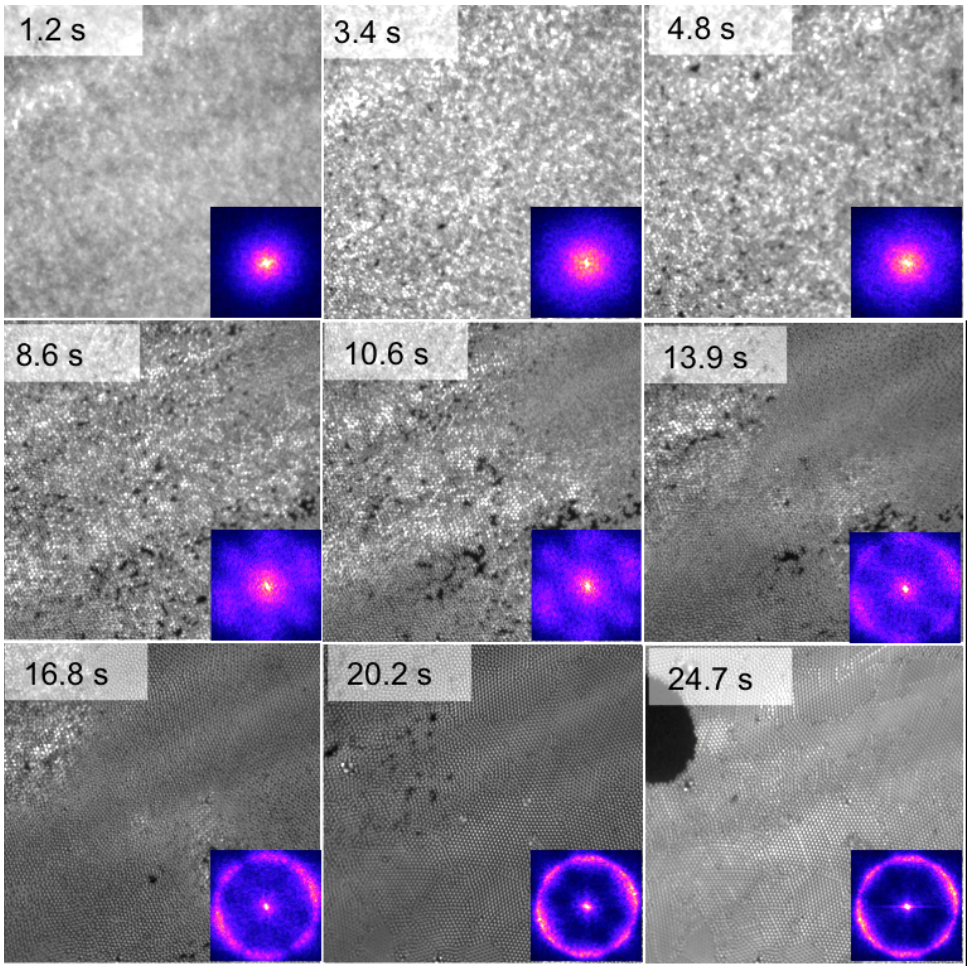

Figure 7.2. Series of stroboscopic microscopy images (with corresponding FFTs) for a 35 wt% colloidal dispersion in water spun-cast at 1250 rpm.

The 45 wt% (Figure 7.3, accompanying movie http://youtu.be/egT_G8oiX-Q) dispersion exhibits regular close packed structures at ~ 2 s, which are highly apparent in both the real and reciprocal space images (occurring significantly earlier than the in 35 wt% solution), during the shear thinning stage, which stops at approximately 8 s as evaporative thinning begins to dominate. During this thinning stage a large degree of re-organisation of the colloids occurs. The 45 wt%

dispersion forms ordered structures earlier on in the thinning process due to the high initial concentration of colloid particles, making regular close packing favourable so as to arrange the greater number of colloid particles. The morphology becomes fixed at ~15 s and after this we observe a drying front sweeping across the film as the remains of the dispersant evaporates. In this case there is an excess of particles for complete surface coverage and so a multilayer is formed (as opposed to the monolayers and incomplete monolayers formed by the 25 and 35 wt% solutions). The final structure formed is a highly crystalline, multilayer colloidal crystal containing both HCP and FCC regions, with small crystalline regions separated by defects.

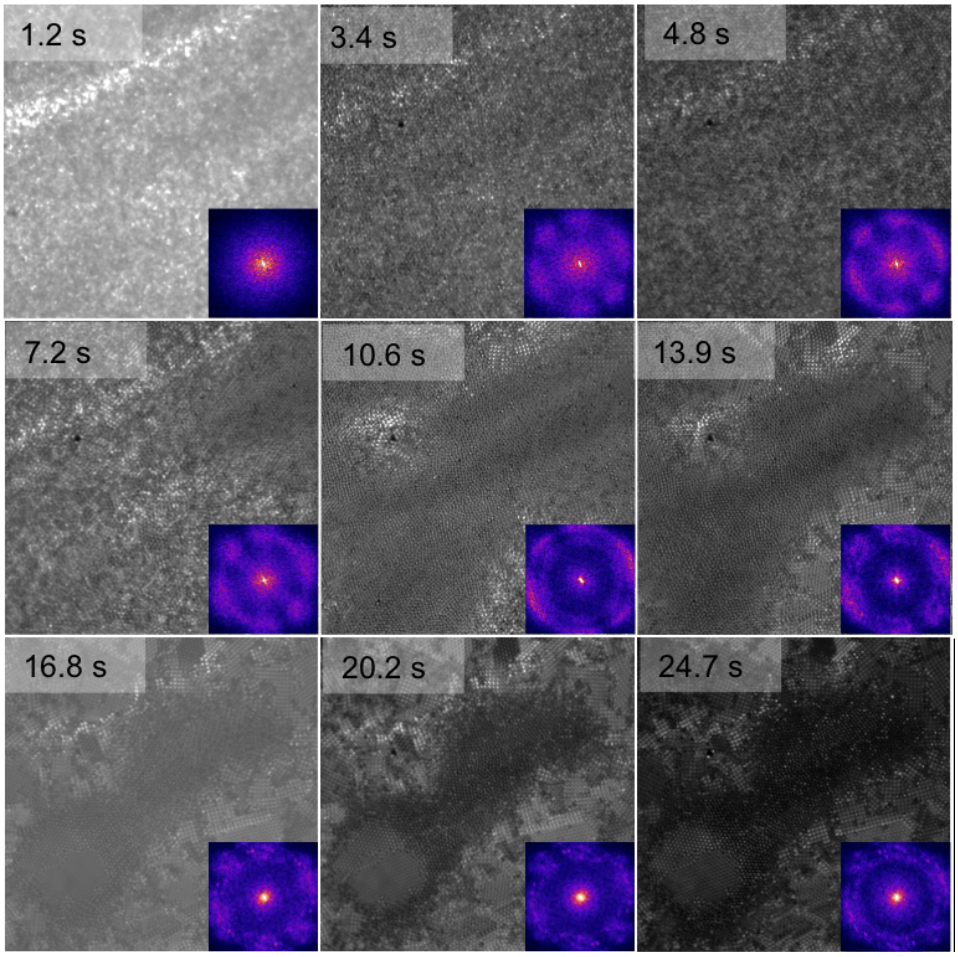

Figure 7.3. Series of stroboscopic microscopy images (with corresponding FFTs) for a 45 wt% colloidal dispersion in water spun-cast at 1250 rpm.

The behaviour observed for the colloidal dispersion spun-cast from water at varying concentrations show two distinct ordering mechanisms, where ordering may occur due to capillary drying fronts or simply due to packing constraints arising due to high particle concentration, reducing the inter-particle separation.

In order to investigate the role of the dispersant volatility, colloidal dispersions were made up in ethanol (vapour pressure = 5.83 kPa, compared to that of water = 2.30 kPa at 20 °C) at similar particle concentrations ranging from 25 to 45 wt%.

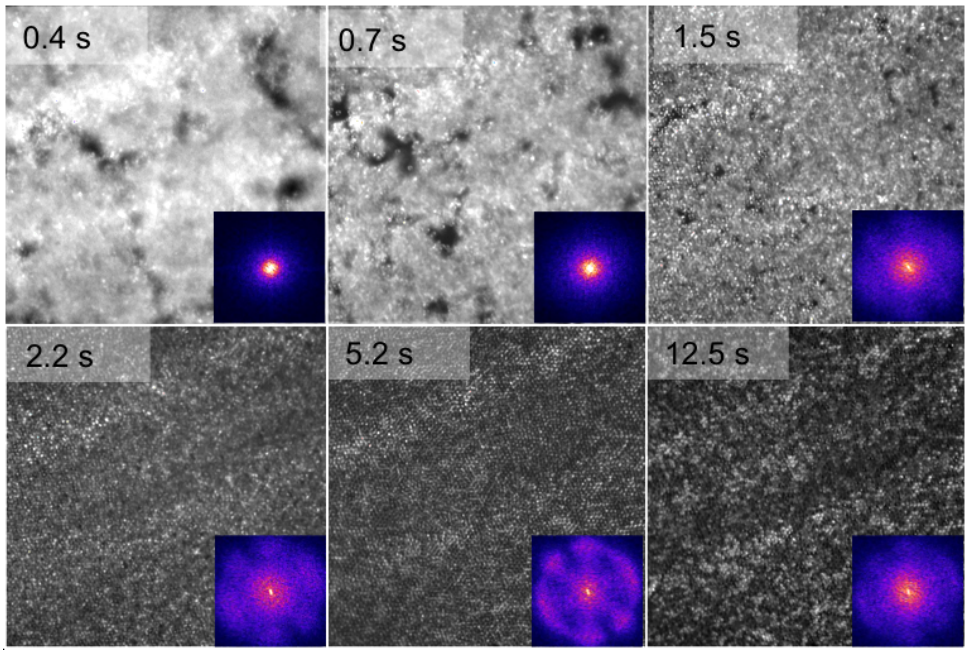

Figure 7.4. Series of stroboscopic microscopy images (with corresponding FFTs) for a 25 wt% colloidal dispersion in ethanol spun-cast at 1250 rpm.[b]

In situ stroboscopic microscopy data for a 25 wt% colloidal dispersion made up in ethanol, spun-cast at 1250 rpm is shown in Figure 7.4 (accompanying movie http://youtu.be/aPfY-tu03ZY). Unlike the dispersions spun-cast from water there is no apparent radial flow, indicating that even early on in the spin-coating process

[b] Only six frames are presented in Figures 7.4 – 7.6 as there is significantly less evolution in structure between the frames.

thinning is already dominated by evaporation of the dispersant. At 1.5 s a densely packed monolayer forms. The FFT image reveals that there is very weak six-fold symmetry, indicating that there are some regular close packed regions. The strength of this symmetry increased between ~2 – 10 s, indicating that the structure undergoes a degree of re-organisation, forming crystalline domains. However, after 10 s the strength of this symmetry appears to become significantly weaker. Due to the formation of a number of random close packed layers on top of the initial monolayer. This to a highly disordered structure, which forms in this system is attributed to the rapid evaporation of the dispersant preventing particles being incorporated into equilibrium positions in the particle arrays, and instead the particles become trapped in non-equilibrium, disordered arrangements. In effect, a skin of random packed particles is formed. Similarly to the 25 wt% dispersion in ethanol, when the 35 and 45 wt% (Figure 7.5 and Figure 7.6, respectively) dispersions were spun-cast the particles formed highly disordered arrangements. The data shows that as the concentration increases a greater number of particles remain out of focus, longer into the spin-coating process, which we attribute to the presence of Marangoni flows. Unlike the dispersions made up in water, those in ethanol do not posses any significant order, with particles arranged in a fashion similar to a disordered glass. The presence of such flows, coupled with a higher vapour pressure solvent (than water) prevents the system from re-ordering to form ordered colloidal crystal like structures.

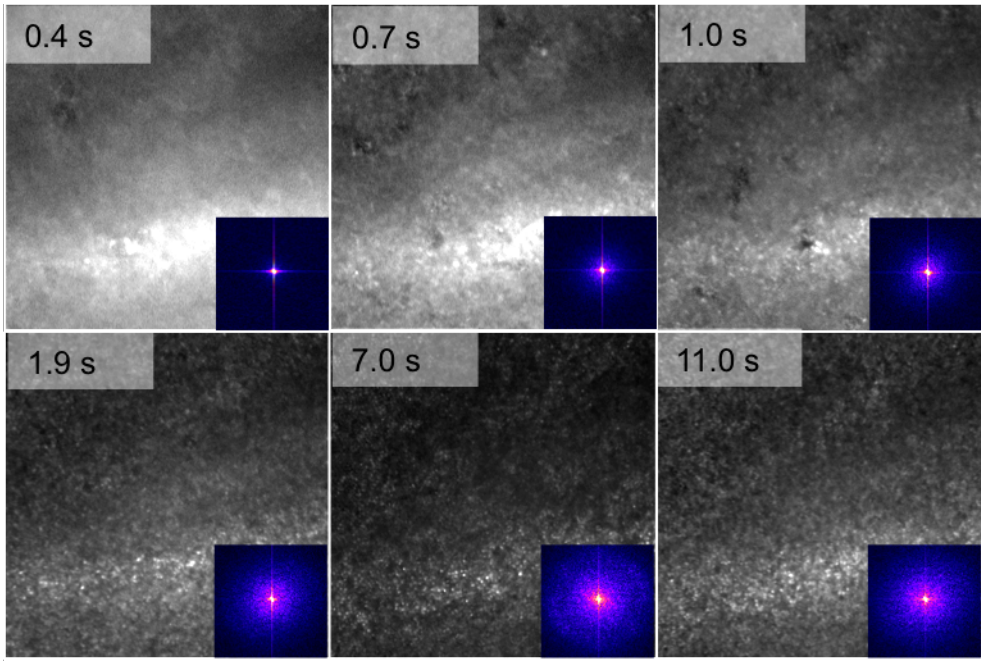

Figure 7.5: Series of stroboscopic microscopy images (with corresponding FFTs) for a 35 wt% colloidal dispersion in ethanol spun-cast at 1250 rpm.

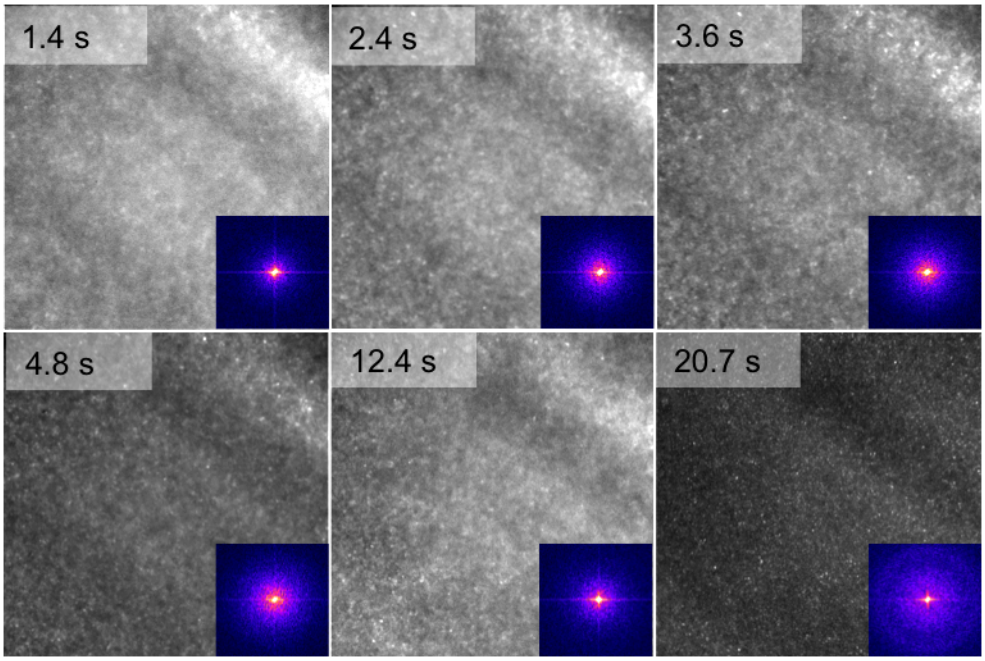

Figure 7.6. Series of stroboscopic microscopy images (with corresponding FFTs) for a 45 wt% colloidal dispersion in ethanol spun-cast at 1250 rpm.

Early on in the spin-coating of the 35 and 45 wt% dispersions from ethanol ($t < 4$ s), a large number of particles appear out of focus for dispersions spun-cast from either water or ethanol at various concentrations. As the focal plane lies on the substrate, we can infer that any out of focus particles are therefore above the

substrate. For the dispersions spun-cast from ethanol, a larger proportion of particles are above the substrate. We attribute this behaviour to the occurrence of Marangoni flows that act to drag the particles towards the evaporating surface of the thinning film. Figure 7.7 Show SEM micrographs of the final structures of colloidal dispersions spun cast from water (a and b) and ethanol (c and d) at concentrations of 25 wt% (a and c) and 45 wt% (b and d). These micrographs clearly show the ordered structures that form when the colloids where spin-coated from water, which are arranged in regular close packed arrays and the relatively disordered structures that form when colloids where spun-cast from ethanol.

The formation of a skin layer of particles was modelled by Routh and Zimmerman.[27] The concept of their work was that in a system where diffusion dominates the particles remain uniformly distributed. However, if the diffusive processes are weak, evaporation of the dispersant results in a non-uniform particle distribution with the formation of a skin.[28] Reyes and Duda performed Monte Carlo simulations showing that at slow evaporation rates particles are able to crystallise, whilst for faster evaporation rates random close packed structures will form.[29] It is possible that for the solutions spun-cast from ethanol, rapid evaporation, results in a colloidal glass transition,[30,31] where the particles are jammed and unable to re-arrange into thermodynamically favourable arrangements.[32]

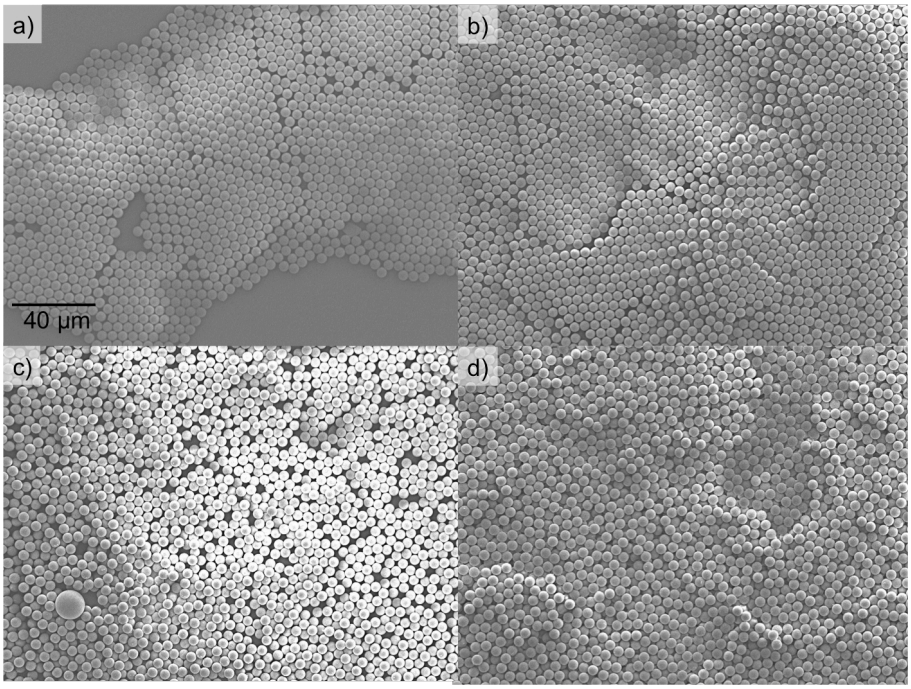

Figure 7.7. Scanning electron micrographs showing the final structures of colloidal dispersions; a) 25 wt% in water, b) 45 wt% in water, c) 25 wt% in ethanol and d) 45 wt% in ethanol spun-cast at 1250 rpm.

Through studying the assembly processes of polystyrene colloids from both water and ethanol we have been able to show how the dispersant volatility has a large impact upon the uniformity and order of the final morphology with the density of particle coverage and the rate of evaporation determining if ordering takes place via the formation of capillary fronts or through re-organisation.

In order to further explore these relationships I have studied colloidal dispersions in mixtures of water and ethanol. Figures 7.8 – 7.9 show the ordering of spin-coated 25 wt% colloidal dispersions made up in water:ethanol mixtures mass compositions of 6:4, 1:1 and 4:6, having combined vapour pressures of 3.8, 4.2, 4.5 kPa , respectively.

Data for the 6:4 (water:ethanol, 25 wt%) dispersion is shown in Figure 7.8 (accompanying movie http://youtu.be/6hwLPv1BX3U). Early on during the coating process (~1.25 s) the dispersion behaves in a similar manner to that of the pure

ethanol dispersion, forming a monolayer (with weak six-fold symmetry), containing a large number of voids, with a large amount of particle flow occurring above the image plane. As the film thins voids become filled by particles which sediment. By 3 s the monolayer contains no voids and begins to flow (from the bottom to the top of the image plane) due to shear forces. This shear flow induces further ordering within the particles, which can be readily seen in the FFT images. At ~10 s a number of particles become pinned at the substrate surface and much slower particle flow may be observed until ~34 s, after which, ordering proceeds via capillary effects occurring due to the presence of voids in the morphology.

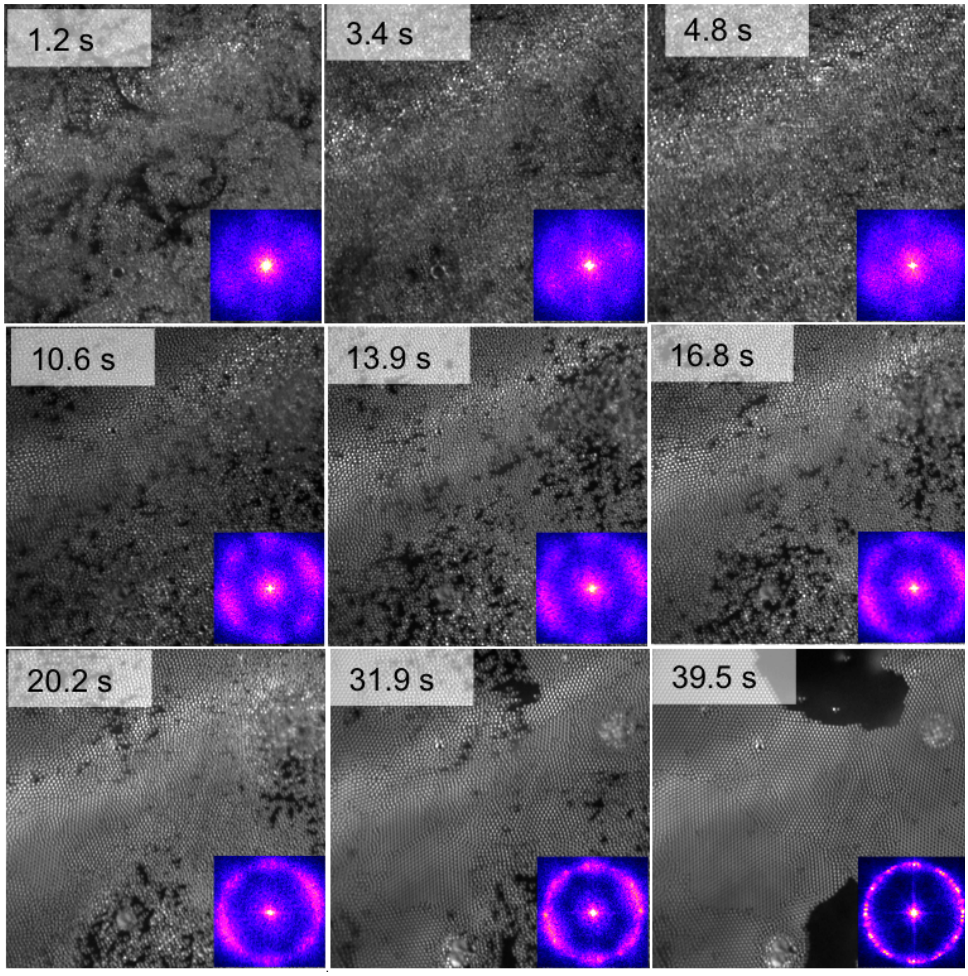

Figure 7.8. Series of stroboscopic microscopy images (with corresponding FFTs) for a 25 wt% colloidal dispersion in a water:ethanol mixture (6:4) spun-cast at 1250 rpm.

The colloidal dispersion spun-cast from a 1:1 mixture of water and ethanol (Figure 7.9, accompanying movie http://youtu.be/6XxcPaE_OdY) initially forms a monolayer on the substrate surface (~ 1 s). The coverage of which, increases through the sedimentation of subsequent particles as a result of particle flow. The FFT images reveal that the monolayer shows weak six-fold symmetry from 2.4 s onwards and by ~3.5 s the monolayer appears to completely cover the substrate. Particle flow occurs above the monolayer, until 8.9 s, after which the monolayer begins to order due to the shear forces. Initially, this process involves the flow of particles to fill any void spaces. At ~24 s the whole monolayer begins to flow

(towards top right of image) as a consequence of shear. During this period the FFT images reveal a dramatic increase in the crystallinity of the colloid array structure and at ~29 s, it is possible to observe clear rotation of crystallisation spots evoked by shear induced re-organisation and we attribute this to be an example of shear induced crystallisation.

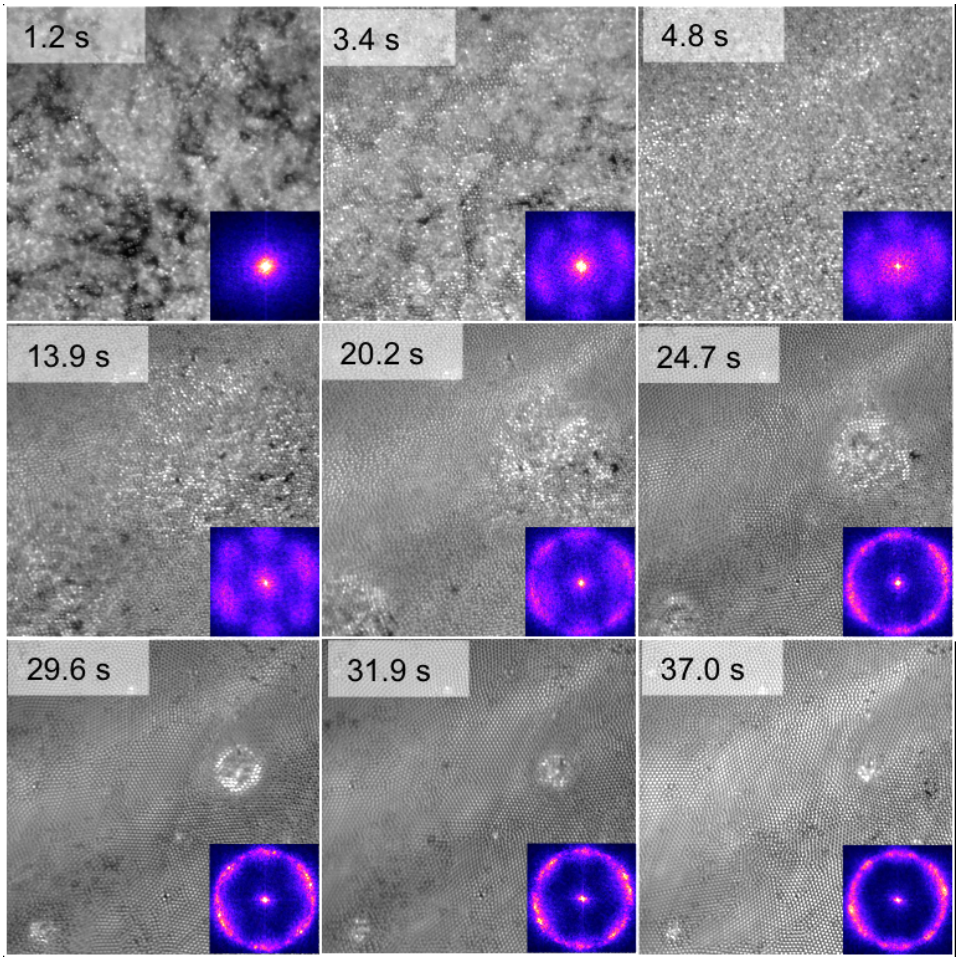

Figure 7.9. Series of stroboscopic microscopy images (with corresponding FFTs) for a 25 wt% colloidal dispersion in a water:ethanol mixture (1:1) spun-cast at 1250 rpm.

Data for the 4:6 dispersion (Figure 7.10, accompanying movie http://youtu.be/4ssdBrFJ48A) shows that an initial ordered monolayer forms early on (~ 1 s), which then re-orders due to shear forces (1 – 5 s) resulting in the formation of a highly ordered regular close packed structure. This structure forms

in a similar manner to that of the 1:1 dispersion, however, in the case of the 4:6 dispersion this ordering is disrupted due to excessive shear, resulting in the formation of voids and subsequent capillary ordering. This capillary induced ordering occurs between 20 and 25 s (as described earlier), resulting in the formation of a highly ordered regular close packed polycrystalline structure, containing large voids.

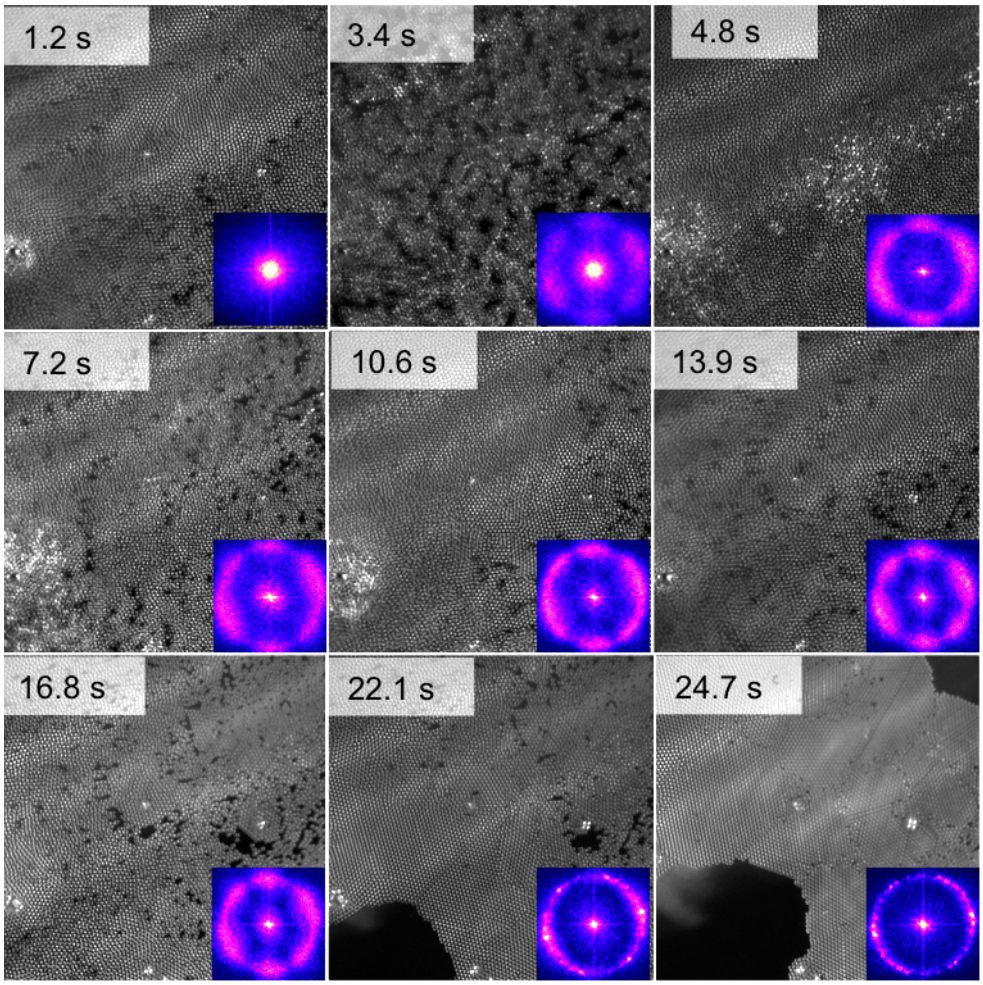

Figure 7.10. Series of stroboscopic microscopy images (with corresponding FFTs) for a 25 wt% colloidal dispersion in a water:ethanol mixture (4:6) spun-cast at 1250 rpm.

For the water:ethanol colloidal dispersions it is evident that early on colloids are distributed at both the substrate and above the image plane (towards the film-air interface) due to both particle sedimentation and evaporation inducing the formation

of a skin.[27,33] As the film thins the particles become constrained and only a single monolayer at the substrate is observed. For the water:ethanol dispersion with the lowest volume fraction of ethanol, capillary effects dominate the ordering of the final structure, whilst for the 1:1 water:ethanol dispersion shear induced re-ordering leads to the formation of highly ordered structures and for the dispersion with the highest volume fraction of ethanol, excessive shear leads to the formation of holes within the system and so hole formation induces a large degree of order. This excessive shear is analogous to shear-induced melting described by Ackerson *et al*.[34]

7.3 Conclusions

In Figure 7.11 shows a schematic summarising the results from this chapter. I have directly observed ordering occurring due to high concentrations of colloid particles (where volatility is relatively low), resulting in the formation of ordered HCP and FCP arrays. Conversely when the system in spun-cast from a much more volatile solvent, highly disordered non-equilibrium arrangements of particles form. When spin-coating a low concentration, low volatility dispersion, ordering is dominated by the occurrence of capillary drying fronts that from the formation of holes within the wetting film. At certain volatility, of an intermediate value between that of water and ethanol, ordering occurs predominantly via shear forces. Finally when the volatility is further increased above this intermediate value at the shear ordering regime, excessive shear leads to the formation of holes within the system and so hole formation induces a large degree of order.

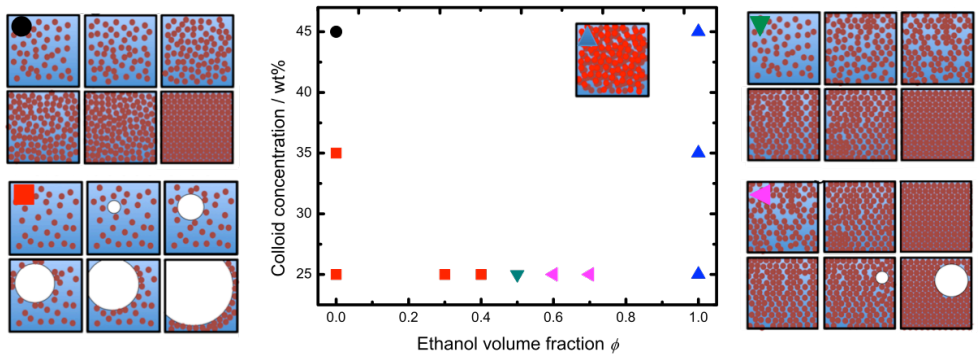

Figure 7.11. Schematic summarising the observed mechanisms of colloidal ordering that depend upon the colloid concentration and the solvent volatility, where the mechanisms ordering are; ●, concentration induced, capillary induced ▼, shear induced , shear collapse followed by capillary induced and ▲, disordered structures.

7.4 References

1. Deegan RD, Bakajin O, Dupont TF, Huber G, Nagel SR, Witten TA. Capillary flow as the cause of ring stains from dried liquid drops. Nature. 1997;389(6653):827-9.
2. Wijnhoven JEGJ, Vos WL. Preparation of Photonic Crystals Made of Air Spheres in Titania. Science. 1998;281(5378):802-4.
3. Jiang P, McFarland MJ. Large-Scale Fabrication of Wafer-Size Colloidal Crystals, Macroporous Polymers and Nanocomposites by Spin-Coating. Journal of the American Chemical Society. 2004;126(42):13778-86.
4. Mihi A, Ocana M, Miguez H. Oriented colloidal-crystal thin films by spin-coating microspheres dispersed in volatile media. Adv Mater (Weinheim, Ger). 2006;18(17):2244-9.
5. Chen J, Dong P, Di D, Wang C, Wang H, Wang J, et al. Controllable fabrication of 2D colloidal-crystal films with polystyrene nanospheres of various diameters by spin-coating. Applied Surface Science. 2013;270(0):6-15.
6. Bartlett AP, Pichumani M, Giuliani M, Gonzalez-Vinas W, Yethiraj A. Modified spin-coating technique to achieve directional colloidal crystallization. Langmuir. 2012;28(6):3067-70.
7. Colson P, Cloots R, Henrist C. Experimental Design Applied to Spin Coating of 2D Colloidal Crystal Masks: A Relevant Method? Langmuir. 2011;27(21):12800-6.
8. Mihi A, Ocaña M, Míguez H. Oriented Colloidal-Crystal Thin Films by Spin-Coating Microspheres Dispersed in Volatile Media. Advanced Materials. 2006;18(17):2244-9.
9. Arcos C, Kumar K, González-Viñas W, Sirera R, Poduska KM, Yethiraj A. Orientationally correlated colloidal polycrystals without long-range positional order. Physical Review E. 2008;77(5):050402.

10. Rehg TJ, Higgins BG. Spin coating of colloidal suspensions. Aiche J. 1992;38(4):489-501.
11. Shereda LT, Larson RG, Solomon MJ. Local stress control of spatiotemporal ordering of colloidal crystals in complex flows. Physical review letters. 2008;101(3):038301.
12. Giuliani M, González-Vinas W, Poduska KM, Yethiraj A. Dynamics of crystal structure formation in spin-coated colloidal films. The Journal of Physical Chemistry Letters. 2010;1(9):1481-6.
13. Jones RAL. Soft condensed matter: Oxford University Press; 2002.
14. Pusey PN, Vanmegen W. Phase-Behavior of Concentrated Suspensions of Nearly Hard Colloidal Spheres. Nature. 1986;320(6060):340-2.
15. Denkov N, Velev O, Kralchevsky P, Ivanov I, Yoshimura H, Nagayama K. Two-dimensional crystallization. 1993.
16. Kralchevsky PA, Denkov ND. Capillary forces and structuring in layers of colloid particles. Current Opinion in Colloid & Interface Science. 2001;6(4):383-401.
17. Ohara PC, Gelbart WM. Interplay between hole instability and nanoparticle array formation in ultrathin liquid films. Langmuir. 1998;14(12):3418-24.
18. Elbaum M, Lipson SG. How does a thin wetted film dry up? Physical Review Letters. 1994;72(22):3562-5.

Chapter 8. Conclusions and future work

8.0 Conclusions and future work

In this thesis I have advanced the technique of stroboscopic microscopy to allow the study of topographies, composition and crystallisation, directly during the spin-coating of a number of polymer systems, investigating a number of key parameters.

The first parameter investigated was the effect of rotation rate on the phase separation of PS:PMMA blends. I was able to directly visualise and follow the growth of an initial bicontinuos interconnected morphology, that subsequently coarsened and coalesced. The degree of coarsening and coalescence that could occur was controlled by the quench through the phase diagram, which is dependant upon the rate of evaporation of solvent from the system, as expected faster rotation rates, lead to greater evaporation rates and subsequently morphologies with a smaller characteristic length-scale. I also observed that a loss in the reciprocal length-scale in the system I have studied resulted in no significant change in the lateral phase separated morphology.

Future work (1): The PS:PMMA system that I have studied had a significantly higher molecular weight than the systems studied by Heriot and Jones and Mokarian *et al.* where lateral structure was believed to have formed through an interfacial instability in transient wetting layers. In order to confirm this mechanism of structural development it would be useful to study the same PS:PMMA systems (molecular weight, polydispersity, solvent, concentration) using the direct imaging technique I have developed.

The second parameter that I studied was the effect small differences in composition have on morphological development of blends of PS:PFO. I found that for the compositions studied all blends exhibited an initial bicontinuous phase-separated morphology, indicative of spinodal decomposition early on in the spin-coating process. At a point in time depending upon composition, a decay of this initial morphology occurs, resulting in a break-up of the bicontinuous structure and the formation of a morphology comprising of distinct islands within a continuous matrix. The point at which the bicontinuous morphology broke up, shows compositional dependence, so is likely to be caused by an interfacial instability. The final morphology obtained, was highly dependent upon when the loss of interconnectivity occurred. When triggered a secondary smaller lengthscale is formed that limits the amount of coarsening and coalescence that may occur. When interconnectivity was lost later on, the blend viscosity was too high for a substantial amount of coarsening/coalescence to occur to restore the initial interconnectivity. Whilst, when the interconnectivity was lost at an intermediate between these two extremes a significant amount of coarsening and coalescence restored a high degree of the interconnectivity of the morphology. With the knowledge that early on in the phase separation process all the blends studied exhibited interconnected morphologies, I employed an *in situ* feedback protocol that allowed me to direct phase separation to obtain more interconnected morphologies, at compositions that may not readily exhibit such interconnectivities.

Future work (2): The observed "loss of interconnectivity" observed for PFO:PS may be a common phenomena occurring for other blend systems containing highly conjugated polymers, as such it would be interesting to see if the same

behavior is observed in related conjugated polymer blend systems (F8BT, PFB, P3HT, etc…).

Future work (3): The *in situ* fluorescent technique has so far been developed for the study of one fluorophore, however with the implementation of a dual camera set-up with appropriate beam splitters two fluorophores could be studied simultaneously. Such a set-up would allow the behavior of two fluorescent polymers to be observed in greater detail.

The third parameter I have studied was the effect of polydispersity on phase separation in blends of PFO and PS, where PSs of different polydispersities where blended with PFO of a constant polydispersity. For the low polydispersity blends phase separation was initially observed to proceed via spinodal decomposition. Whilst, high polydispersity blends formed an initial droplet like morphology, indicative of nucleation and growth. The difference in this behavior was attributed to a shift in the critical point of the phase diagram. I further showed that through blending PSs of different polydispersities it is possible to tune the critical point and control whether phase separation proceeds via spinodal decomposition or nucleation and growth.

In order to study crystallisation processes during spin-coating I employed a crossed polariser set-up to study crystallisation of pure PEG and the interplay between crystallisation and phase separation in blends of PEG with PS. I found that independent of concentration of polymer in solution, the process occurred at the same rate, indicative of isothermal crystalisation, as found for polymer melts. Through controlling spin-coating parameters such as the acceleration rate, it was possible to control the point at which crystallisation occurred. For the PEG:PS blends I observed that Marangoni effect play an important role in governing phase

separation. Further we found that for this blend system phase separation and crystallisation occur completely independently and not “hand in hand” as reported by Chou *et al.*

Future work (4): Although the my work and the recent work of Chou *et* al has cast new light on the crystallisation processes that may occur during spin-coating, we still only have a limited understanding of how crystallisation proceeds during spin-coating and how the process is affected by; i) thin-film confining geometry,ii) shear forces induced by rotation, iii) non-equilibrium nature of the rapid quench, iv) role of solvent, when compared to that of bulk crystallisation.

Finally I progressed my work beyond that of polymer blends to study the ordering of colloidal dispersions. I have been able to identify a number of different ordering mechanisms that may occur depending upon solution viscosity and the particle concentration.

Future work (5): My studies on colloidal crystallisation during spin-coating examined only a very narrow parameter space (particle size, particle size distribution, viscosity, volatility, spin-speed, acceleration rate). Future experiments should aim to systematically investigate the above mentioned parameters.

Publications (since the start of my PhD in July 2011).

		Journal Impact Factor
9.	**Daniel T. W. Toolan**, Syuji Fujii, Stephen J. Ebbens, Yoshinobu Nakamura, Jonathan R. Howse. On the mechanisms of colloidal self-assembly during spin-coating. Soft Matter (2014). DOI: 10.1039/C4SM01711K	4.151
8.	Ehtsham Ul Haq, Daniel T. W. Toolan, Jillian A. Emerson, Thomas H. Epps III, Jonathan R. Howse, Alan D. F. Dunbar and Stephen J. Ebbens. Real time laser interference microscopy for bar-spread polystyrene/poly(methyl methacrylate) blends. Journal of Polymer Science Part B: Polymer Physics (2014). DOI: 10.1002/polb.23513 ***Featured as the front cover.*** 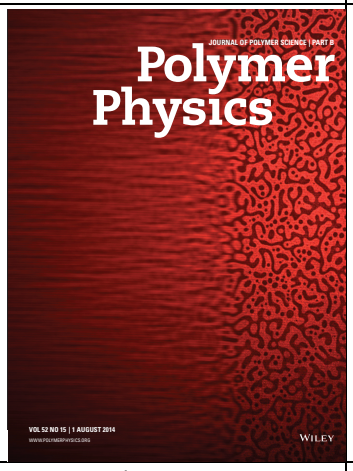	2.211
7.	**Daniel T. W. Toolan,** Richard Hodgkinson, Jonathan R. Howse. Stroboscopic Microscopy – Direct Imaging of Structure Development and Phase Separation During Spin-Coating. Journal of Polymer Science Part B: Polymer Physics (2013). 52 (1), 17-25.	2.211
6.	**Daniel T.W. Toolan**, Nikki Pullan, Michael J. Harvey, Paul D. Topham, Jonathan R. Howse. *In Situ* studies of Phase Separation and Crystallization Directed by Marangoni Instabilities during spin-coating. Advanced Materials (2013), 25 (48), 7033-7037. ***Featured as the front cover.*** 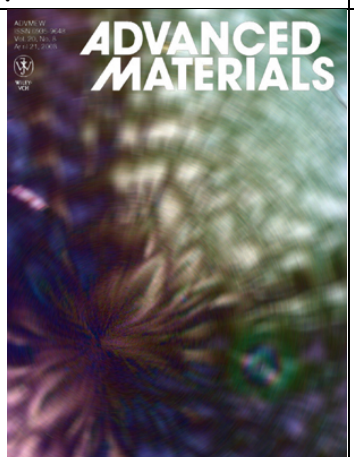	14.829
5.	Jillian A. Emerson, **Daniel T. W. Toolan**, Jonathan R. Howse, Eric M. Furst, Thomas H. Epps, III. Determination of Solvent−Polymer and Polymer−Polymer Flory− Huggins Interaction Parameters for Poly(3-hexylthiophene) via Solvent Vapor Swelling. Macromolecules (2013). 46(16), 6533-6540.	5.521
4.	Paul D. Topham, Andrew Glidle, **Daniel T. W. Toolan**, Michael P. Weir, Maximillian Skoda, Robert Barker, Jonathan R. Howse. The relationship between charge density and polyelectrolyte brush profile using simultaneous neutron reflectivity and *in situ* total internal reflection FTIR. Langmuir (2013). 29(20), 6068-6076. *	4.187

3.	**Daniel T. W. Toolan**, Ehtsham ul Haq, Alan Dunbar, Stephen Ebbens, Nigel Clarke, Paul D. Topham, Jonathan R. Howse. Direct Observation of morphological development during the spin-coating of polystyrene-poly(methyl methacrylate) polymer blends. Journal of Polymer Science Part B: Polymer Physics (2013), 51(11), 875-881. ***Featured as the front cover.*** 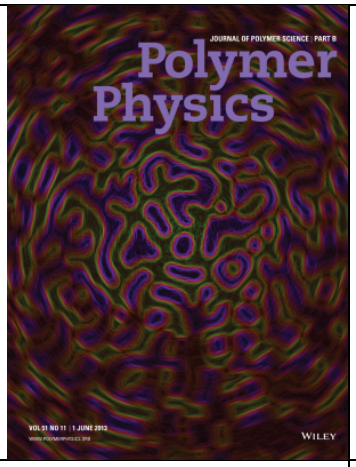	2.211
2.	**Daniel T. W. Toolan**, Andrew J. Parnell, Paul D. Topham, Jonathan R. Howse. Directed phase separation of PFO:PS blends during spin-coating using feedback controlled *in situ* stroboscopic fluorescence microscopy. Journal of Materials Chemistry A (2013), 1, 3587-3592. ***Appeared as part of web collection "Rising Stars and Young Nanoarchitects in Materials Science".*** *Featured the Journals first animated table of contents* (Click here).*	6.101
1.	**Daniel T. W. Toolan**, Jonathan R. Howse.* Development of *in situ* studies of spin coated polymer films. Journal of Materials Chemistry A (2013), 1, 603-616	6.101

Presentations

9.	Dynamical studies of spin-coated polymer blends – Poster presentation. Advanced School in Soft Condensed Matter "Solutions in the Spring", Cambridge 2014. ***Best poster***.
8.	Dynamical studies of spin-coated polymer blends – Poster presentation. SET for Britain Parliamentary Poster Competition, Westminster 2014. ***Bronze award in the physical sciences (chemistry)***.
7.	Stroboscopic microscopy: Direct imaging of structural developments during spin-coating – Oral contribution. Interface Chemistry Association (ICA) the 4th lecture, Osaka 2013. ***Invited lecture.***
6.	Directed phase separation of PFO:PS blends during spin-coating using feedback controlled in situ stroboscopic fluorescence microscopy – Oral contribution. Physical Aspects of Polymer Science, Sheffield 2013. ***Invited lecture as part of the Institute of Physics, Polymer Physics Group, PhD paper of the year 2013.***
5.	Polymers in a spin: Directed phase separation of PFO:PS blends during spin-coating using feedback controlled in-situ stroboscopic fluorescence microscopy – Oral contribution. 29th International Conference of the Polymer Processing Society, Nuremburg 2013. Attendance support through; **Macro Group D.H Richards Memorial Bursary, RSC Materials Division Bursary and Armourers & Brasiers' Rolls Royce Bursary (2013).**

4.	Polymers in a spin: Direct imaging of topographical, compositional and crystallographic features during spin-coating – Poster presentation. Solutions in the Spring, Leeds 2013.
3.	Direct observation of phase separation in PS:PFO blends during spin coating via high speed stroboscopic fluorescence microscopy – Oral contribution. IOM^3 Young lecturer competition Durham & Teeside 2012. ***Regional winner.***
2.	Direct observation of phase separation in PS:PFO blends during spin coating via high speed stroboscopic fluorescence microscopy - Oral contribution. Macro Group Young Researchers Meeting, Cambridge 2012. ***Awarded "Macro Group Young Researcher of the Year 2012".***
1.	*In situ* studies of spin-coated polymer films – Poster presentation. Higher European Research Course for Users of Large Experimental Systems (HERCULES), Grenoble 2012.